Aeroelastic analysis of a 3D wing structure with a flexible trailing edge

J. Lonsain

Technische Universiteit Delft

TU Delft

Aeroelastic analysis of a 3D wing structure with a flexible trailing edge

by

Johannes Lonsain

to obtain the degree of Master of Science,
at the Delft University of Technology,
to be defended publicly on monday March 27, 2017 at 12:30 PM.

Student number: 1545310
Thesis committee: Dr. S. R. Turteltaub
Dr. Ir. O. K. Bergsma
Dr. Ir. R. De Breuker, supervisor
Dr. J. Sodja, supervisor

A digital copy of this report can be found at: http://repository.tudelft.nl
Cover picture obtained from: http://articles.sae.org/7987

TU Delft

Delft University of Technology
Department of Aerospace Structures and Materials

The undersigned hereby certify that they have read and recommend to the Faculty of Aerospace Engineering for acceptance a thesis entitled:

Aeroelastic analysis of a 3D wing structure with a flexible trailing edge

by
Johannes Lonsain

in partial fulfilment of the requirements for the degree of Master of Science

Graduation Committee

Committee chairman:

Dr. S. R. Turteltaub, MSc.

Signature

Committee member:

Dr. Ir. O. K. Bergsma

Signature

Committee member:

Dr. Ir. R. De Breuker

Signature

Committee member:

Dr. J. Sodja

Signature

Date

Aknowledgments

I would like to thank Jurij and Roeland for all their support while working on my thesis, always taking the time to help me out. I also want to mention Noud, who helped me out often with coding and modelling issues, although he was not my supervisor. For taking the time to be part of my graduation committe, I would like to thank Sergio Turteltaub and Otto Bergsma.

At university, Adriaan, Julliette, Krishna, Maarten, Ron, Stefan and Twan were my fellow thesis students, and I would like to thank them most of all for their company, but they were also very helpful to discuss ideas and problems.

Finally, I want to thank my family, mama, papa, Anne, Sofie and Maarten for their continuous support and patience.

J. Lonsain
Delft, March 2017

Abstract

As aircraft wings become increasingly more slender and lighter to increase flight performance, aeroelasticity is becoming more important to determine the response of such flexible wings. Traditionally, the airfoil of a wing is considered to remain rigid in aeroelastic analyses, only allowing deformation in the span-wise direction of the wing. Recent investigations have shown the benefit of adding chord-wise flexibility in the trailing edge of a wing, however so far only two-dimensional studies have been carried out. Therefore, the investigation presented here determines whether chord-wise flexibility in the trailing edge improves aeroelastic behaviour for three-dimensional wing structures as well.

To determine whether chord-wise flexibility improves the aeroelastic characteristics, a dynamic aeroelastic model is built to compute the flow velocity at which the wing structure becomes instable and a static model to compute the steady aerodynamic loads. For both problems, linear structural and aerodynamic models are used, assuming that wing deflections remain small. This rules out post-critical wing behaviour where oscillations become increasingly large.

Timoshenko beam finite elements are used to represent the wing-box structure and are part of the existing aeroelastic framework PROTEUS, which is developed at the TU Delft. To model the flexible trailing edge, flat shell elements are developed, with 3 deflection and 3 rotational degrees of freedom at each of the 4 corner nodes, such that they are compatible with the beam elements. They are written in an isoparametric representation to allow generic wing shapes to be modelled. Rigid links using the master-slave approach couple the flat shell to the beam elements. The aerodynamic model in PROTEUS is modified in such a way that individual panel forces are extracted and trailing edge deformation can be transferred to these panels. Both structural and aerodynamic models are closely coupled in the static aeroelastic model, and the dynamic model is written in state-space format.

By varying the thickness of a quasi-isotropic carbon fibre laminate in the trailing edge, its flexibility is managed. It was found that increasing the flexibility of the trailing edge increases the flutter speed of the wing in a similar manner as with a 2D typical section. If the thickness becomes too small, plate flutter of the trailing edge occurs, therefore putting a constraint on the minimal thickness. The maximum increase in flutter speed found for a certain wing with a trailing edge comprising 30 % of the chord length, was 13.93%. A difference with a 2D typical section is that in the region of plate flutter, mode jumps occur due to span-wise deflection of the wing-box. If only part of the wing in span-wise direction is equipped with a flexible trailing edge, the flutter speed can be increased more effectively by positioning it towards the tip of the wing. The downside of increased trailing edge flexibility is the reduction in steady lift generated by such a wing.

Contents

Nomenclature

Greek symbols

α	Total perturbance angle of attack of vortex panel	rad
α_0	Wing angle of attack	rad
α_{air}	Perturbance angle of attack induced by free stream flow	rad
δ	Deflection	m
ε	Axial strain	$-$
γ	Shear strain	$-$
Γ	Vortex strength	m^2/s
Γ	Inverse of the Jacobian matrix	$-$
λ	Eigenvalue	$-$
ν	Poisson's ratio	$-$
θ	Plate rotation degree of freedom	rad
Π	Total potential energy	J
ρ	Material density	kg/m^3
ξ	Non-dimensional plate coordinate in the x direction	$-$
μ	Non-dimensional plate coordinate in the y direction	$-$

Latin symbols

A	Cross-sectional area of beam element	m^2
AR	Aspect ratio of the wing	$-$
c	Wing chord	m
E	Modulus of elasticity	N/m^2
G	Shear modulus	N/m^2
I_{ii}	Moment of inertia	m^4
I_p	Polar moment of inertia	m^4
J	Torsional stiffness	m^4
J	Determinant of the jacobian matrix	$-$
k	Shear ratio	$-$
$\mathcal{L}$	Lagrangian	J
L	Length	m
t	Thickness	m
t	Time	s
$\mathcal{T}$	Kinetic energy	J
u	In-plane extension degree of freedom of the plate elements	m
u	Extension degree of freedom of the beam elements	m
$\mathcal{U}$	Strain energy	J
v	In-plane extension degree of freedom of the plate element	m
v	Deflection degree of freedom of the beam element	m
V_e	Element volume	m^3
V_∞	Free stream velocity	m/s
w	Out-of-plane displacement degree of freedom of the plate element	m
w	Deflection degree of freedom of the beam element	m

Subscripts

a	Refers to the aerodynamic model
as	Aerodynamics to structures notation
b	Bending component of the flat shell element
b	Beam degrees of freedom
g	Global coordinate system
l	Local coordinate system
m	Membrane component of the flat shell element
ms	Master-slave relation
p	Plate degrees of freedom
$Q4$	4-node membrane element
$Q8$	8-node membrane element
s	Refers to the structural model
sa	Structures to aerodynamics notation
TE	Refers to the trailing edge region of the wing
x	Refers to variable in x direction, similar for y and z
$,x$	Refers to derivative with respect to x direction, similar for y and z

Vectors and matrices

A	A-matrix of the ABD matrix computed with CLPT
A	Aerodynamic influence coefficients matrix
B	Relates the nodal degrees of freedom to the element's strain field
D	D-matrix of the ABD matrix computed with CLPT
F	Vector containing the loads applied to the structure
J	The jacobian matrix
k	Element stiffness matrix
K	Structure stiffness matrix
m	Element mass matrix
M	Structure mass matrix
n	Normal vector of surface
N	Shape function matrix
p	Structural degrees of freedom
Q	Material constitutive matrix
R	Rotation matrix
T	Transformation matrix

1
Introduction

Aeroelasticity is becoming more and more important in the design of aircraft wings. The main reason for this is that wings are getting increasingly more flexible. Both weight reduction leading to a more compliant wing structure and improved aerodynamic performance, demanding for slender wings, are required to reduce the operating costs of aircraft.
Aeroelasticity is the field of study which investigates the interaction between structures and aerodynamics. To be more precise, aerodynamic loads result in a deformation of the structure, which in return change the aerodynamic loads. This feedback loop means that they should be treated simultaneously to predict the aerodynamic and structural response of an aircraft. Especially since wings are getting more flexible, therefore causing larger deformation and larger changes in aerodynamic behaviour.

Traditionally, the aeroelastic behaviour of chord-wise rigid wings is studied, as it is one of the most important design drivers. But there are some benefits to introducing a degree of flexibility in the chord direction as well: among others, Drazumeric et al. (2014) investigated the effect of a flexible trailing edge on flutter behaviour and found an increase in the flutter and divergence speed compared to a rigid trailing edge. The gradual increase in interest in morphing wings also stimulates the aeroelastic research of chord-wise flexible wings, as increased compliance is required to actively deform wing structure at an acceptable energy cost (De Breuker et al. (2008)).
However, the research done on compliant trailing edges focuses primarily on 2D cases. The aeroelastic behaviour is modelled using a typical section with 2D aerodynamic models and a simplified structural representation. The next step is to implement a flexible trailing edge in a 3D wing structure and investigate its aeroelastic characteristics.

In this introduction, an overview of the most recent advancements in the field of chord-wise flexible aeroelasticity is given in Section 1.1, from which the gap in the body of knowledge was found: to model this chord-wise flexibility in 3 dimensions. Then in Section 1.2, the research question and objective are stated, resulting in requirements for the numerical model that will be build. Next, the research methodology is discussed in Section 1.3. Finally, the outline of the thesis report is given in Section 1.4.

1.1. State of the art

The stability of an airfoil with a flexible trailing edge has been investigated by Drazumeric et al. (2014) and Bergami and Gaunaa (2010). Independent of each other, both authors have modeled the wing as a 2D typical section with pitch, plunge and plate deflection as the degrees of freedom (DOF's). In both cases, increased flexibility had a beneficial effect on the flutter speed, and Drazumeric et al. (2014) showed that the onset of flutter is more benign, which means a less severe amplitude increase at the critical velocity, with a flexible trailing edge. The effects of a flexible trailing edge can be be shown using Figures 1.1 and 1.2, which show the results of the two investigations above:

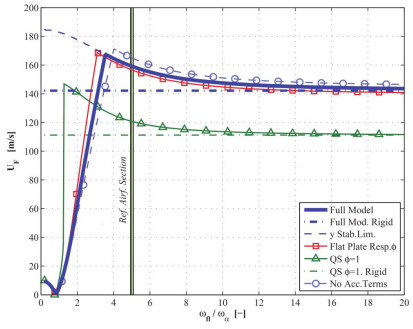

Figure 1.1: Bergami and Gaunaa (2010)

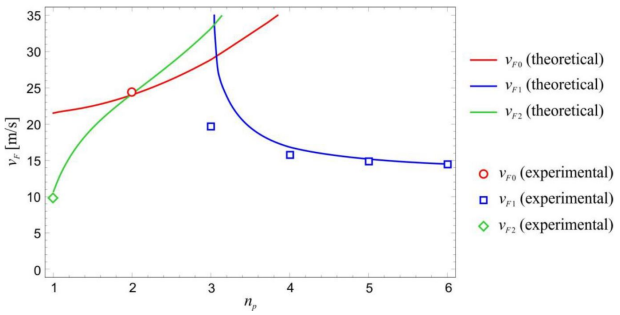

Figure 1.2: Drazumeric et al. (2014)

At the right side of both figures, the stiffness of the flexible trailing edge is relatively high and therefore the aeroelastic behaviour is similar to a wing with a rigid airfoil. Hence, the critical velocity of a wing with a flexible trailing edge converges to a wing with a rigid airfoil if the flexible trailing edge becomes stiffer. If the compliance of the trailing edge increases, which is the case when going from the right to the left side in Figures 1.1 and 1.2, the critical speed increases. At a certain trailing edge flexibility, an optimimal critical velocity is found, after which the critical velocity decreases again, since plate flutter of the trailing edge becomes the dominant instability.
Kim and Lee (1996) and Murua et al. (2010) have also investigated the stability of a 2D typical section, but with flexibility along the entire length of the chord. However, besides showing that the flutter mode related to the camber deflection is important in the stability analysis for specific ratio's of pitch, plunge and camber stiffnesses, no indication that the added flexibility could increase the flutter and divergence speed is found in their research. The models developed in the four investigations above are all based on a 2D typical section.

Before jumping to the research question, the literature about aeroelasticity of chord-wise flexibility is explored and summarised. Firstly, plate flutter of cantilevered plates and partially rigid cantilevered plates is studied. Followed by plate-like wings, in which the wings are modelled using a plate structure, and the possibility of chordwise flexibility to achieve load alleviation.

1.1.1. Plate flutter of cantilevered and partially rigid cantilevered plates

Plate flutter of 2-dimensional structures using 2-dimensional aerodyamics is a field which is well covered in the literature. Kornecki et al. (1976), and several years later Shayo (1980), started investigating the stability of cantilever plates in incompressible and inviscid flow. The first authors concluded that a cantilevered plate with infinite width in subsonic flow is susceptible to flutter and not to divergence. For supersonic it is known that divergence becomes the critical instability. In their analysis, the numerical

results were in good agreement with the experiments they conducted.

A linear investigation of cantilevered plate flutter has also been done by Huang (1995). Among others, he investigated cantilevered plate flutter to better understand human snoring. His findings are similar to Kornecki et al. (1976) and Shayo (1980), but an interesting conclusion is found about how benign flutter onset is for different mass ratios, which is a ratio of the plate's length and fluid's density to the mass of the plate. Given by the equation $\mu = \frac{\rho_f \cdot l_p}{m_p}$. In other words, it says something about the inertia of the plate compared to the mass of the fluid surrounding it. Plates with a high mass ratio react much slower to a a velocity increase close to the critical velocity than plates with a low mass ratio.

Since then, many researchers have investigated the effect of structural non-linearities and 3-dimensional aerodynamic models on the stability of cantilevered plates. Tang and Dowell (2002), assuming a 2-dimensional flow and Tang et al. (2003), assuming a 3-dimensional flow, included structural and inertia non-linearities, but neglected aerodynamic non-linearities. After comparing their numerical results with experiments, they concluded that a 3-dimensional aerodynamic model improves the prediction of velocity at onset of flutter and limit cycle oscillations (LCOs are bounded oscillations beyond the stability boundary) significantly and that aerodynamic non-linearities have to be included to be able to predict the large amplitude LCO's.

Finally, the effect of the span-wise dimension on the flutter of cantilevered plates is studied. Eloy et al. (2007) took the effect of the length of the span of the cantilevered plate explicitly into account, and determined that plates with smaller aspect ratios are more stable. Taking the aspect ratio into account, experimental results for plates with low mass ratios μ are improved. Only one study has modelled the cantilevered plate flutter problem using a 3-dimensional structure. Banerjee et al. (2015), modelled the aerodynamics with a Navier-Stokes model and the structure as a 3-dimensional membrane without bending rigidity. Their conclusion is that adding structural waves in the span-wise direction increase the flutter velocity of a cantilevered plate, compared to a 2-dimensional structure. This confirms the consensus that 3-dimensional structural effects are a cause for the discrepancy between theoretical and experimental results.

Since a chord-wise rigid part of the wing is present upstream of the flexible trailing edge, it is wise to look at research about partially rigid cantilevered plates. Partially rigid cantilevered plate, for which the length of the upstream rigid part has an effect on the stability of the cantilevered plate has been studied by Tanida (2001), Tang and Païdoussis (2007) and De Breuker et al. (2008). Partially rigid means that a part of the structure is rigid. In the studies just mentioned this part does not contribute to the structure of the system, besides providing the boundary conditions at the front edge of the plate. But it does have an effect on the aerodynamics. De Breuker et al. (2008) concluded that increasing the length of the rigid part of the plate can either increase or decrease the flutter speed, depending on the mass ratio μ. Qualitatively, the flutter mode jumps for different mass ratios remain the same for varying rigid part fraction. Tang and Païdoussis (2007) show a similar course of the flutter speed versus mass ratio for different rigid plate fractions.

1.1.2. Stability of plate-like wings

Research to plate-like wings is interesting as the wing with a flexible trailing edge might look more like a plate-like wing as the fraction of the flexible trailing edge becomes larger. Tang et al. (1999a), Tang et al. (1999b), Attar et al. (2003) and Attar et al. (2005) investigated LCO's of plate-like cantilevered and delta wings. Due to their dimensions, these types of wings can be more accurately modelled by a plate model than a beam model. Because the wing is modelled as a plate, deformations are allowed to

occur in the chord-wise direction as well. LCO's with amplitudes in the order of the plate's thickness were predicted by Tang et al. (1999a) and Tang et al. (1999b). A non-linear structural model has been used to account for the non-linearities that arise from double bending in the span-wise and chord-wise direction. Besides, the vortex lattice method has been used to model the aerodynamics. To determine the flutter boundary of the wing, a linearised model was used by excluding the nonlinear force stemming from the double bending. The flutter mode was dominated by the first bending mode in the span-wise direction combined with the first torsion mode.

1.1.3. Chord-wise flexibility as load alleviation

The occurrence of infrequent high loads during the life of aircraft and wind turbines, have triggered many researchers to investigate load alleviation mechanisms to increase the efficiency of light weight structures. The load alleviation potential of flexible airfoils and morphing airfoils are often investigated in wind turbine research with the goal to reduce high load fluctuations originating from gusts for example. By changing the camber of the airfoil, the reduced lift coefficient results in a reduction of the lift force, thereby alleviating the bending moments in the wing structure and at its root.

Active load alleviation by changing the camber of the airfoil was first investigated by Basualdo (2005) and Buhl et al. (2005), both using a trailing edge flap of 10% of the chord length and a control algorithm determined that load fluctuations originating from turbulence could be reduced significantly, up to 25 % in the best case. Andersen et al. (2006) looked at multiple segments of deformable trailing edges with actuation along the span of a wind turbine blade and concluded that the root bending moment during turbulence can be reduced by up to 61%.

The downside of the large share of the mechanisms developed and studied to reduce load fluctuations or loads during manoeuvring is that they require active control of the flap or deformable trailing edge. Lambie et al. (2011) have designed a passive load alleviation concept with a changing camber line due to a leading and trailing edge flap hinged with a rotational spring. More recently, Arrieta et al. (2014) implemented bi-stable composites elements into the ribs of a compliant trailing edge. At a certain threshold load, the bi-stable composite element loses its rigidity and the trailing edge becomes much more compliant, and therefore the camber changes shape under the applied loading. A downside of this mechanism is that the bi-stable elements will not go back to their original shape unaided.

1.2. Research question

From the current state-of-the-art, it can be concluded that the 2-dimensional analyses have clearly shown the potential of increased trailing edge compliance on the stability of a wing structure. However, no researchers have investigated trailing edge flexibility for a three-dimensional wing structure. Hence, the following step is to investigate whether or not the same beneficial effects as shown in the 2-dimensional analyses are also present in 3 dimensional wing structures. The main research question can therefore be stated as:

"To what extent can the aeroelastic characteristics of a 3D wing structure be improved by making its trailing edge flexible, and varying its properties along the span of the wing?"

In which the term aeroelastic characteristics have the following meaning:

- The velocity at which the aeroelastic system becomes unstable due to airfoil flutter, divergence or plate flutter.

- The benignity of the airfoil flutter response: how rapidly the amplitude of the wing motion increases after the critical velocity has been reached.
- The steady aerodynamic loads on the wing structure.

1.3. Methodology

To answer the research question, an aeroelastic model of a three-dimensional wing structure is built in which chord-wise deformation of the trailing edge is allowed, to analyse the static and dynamic aeroelastic response. It is decided to start-off with an existing aeroelastic model, called PROTEUS, developed at the TU Delft, and extend it such that a wing with a flexible trailing edge can be modelled. This model will then be used to investigate the static and dynamic aeroelastic response of a 3D wing structure with a flexible trailinge edge.

1.3.1. The aeroelastic model

The PROTEUS model is chosen because, (1) extending the model is possible as it has been developed in-house, and (2) the aerodynamic and structural model on which the model is built satisfy the requirements for a wing with a flexible trailing edge.

This study will focus on velocities in the low subsonic regime, just like the 2-dimensional analyses have done. Also, the oscillations of the wing and flexible trailing edge are assumed to be small, limiting the scope of the investigation to velocities around the flutter velocity. As a consequence, the assumptions of the linear potential flow theory used in PROTEUS (incompressible, irrotational and inviscid flow) are valid.

In PROTEUS the static structural model is based on non-linear Timoshenko beam elements, and linear Timoshenko beam elements for the dynamic model. A structural model based on beam elements is suitable to represent the wing box, which is the chord-wise rigid part of the wing. In the current study, the static model in PROTEUS is used as a linear model to make the combination with the trailing edge structure more convenient. Just like with the aerodynamic model, the structural model can be linear, under the assumption that beam and plate deflections are small, which is the case around the flutter velocity.

The existing PROTEUS model is extended in the following way. To represent the flexible trailing edge structure, linear flat shell elements are used. To connect these trailing edge elements to the beam elements representing the wing box, rigid links are used. The aerodynamic model is not extended, since it can represent any wing deformation, including a flexible trailing edge. But since it is programmed in PROTEUS to accommodate a chord-wise rigid wing, it will be modified to include the chord-wise deformation in the trailing edge. In Figure 1.3, a schematic representation of the entire model is shown

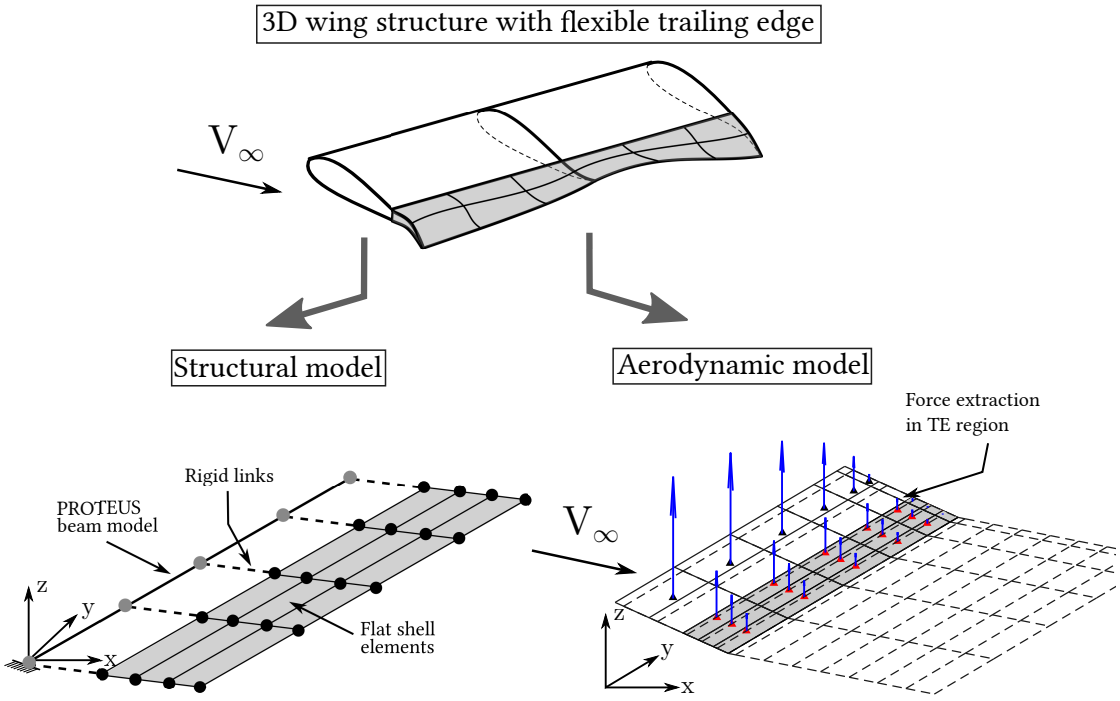

Figure 1.3: Schematic representation of the structural and aerodynamic model

Flat shell elements are chosen for the trailing edge structure since it is a convenient way to represent a compliant structure. The detailed design of a flexible trailing edge might be more complicated than a simple plate, considering that the aerodynamic design favours a continuous airfoil shape. The stiffness and mass distribution of the trailing edge can then be varied using the thickness and material properties of the plate elements. During the investigation, composite laminates and aluminium alloys are used as material.

When the aeroelastic model is finished, it has to be verified to give confidence that it can predict aeroelastic behaviour of a wing with a flexible trailing edge. To achieve this in the absence of verification cases of 3D wings with a flexible trailing edge, the present model of the trailing edge is compared to a plate flutter and a plate-like wing study. In addition, the complete model is compared to the original PROTEUS model, to which the model with a flexible trailing edge should converge if the trailing edge becomes stiff in the chord-wise direction.

1.3.2. Design studies

When the aeroelastic model is finished and verified, it is used to investigate the aeroelastic characteristics of a 3D wing structure with a flexible trailing edge. First, a baseline wing configuration with a chord-wise rigid trailing edge will be defined. How a flexible trailing edge affects this system is determined by keeping the properties of the wing box structure constant and varying the properties and dimensions of the trailing edge. This means varying the thickness and chord-wise length of the trailing edge, varying the span-wise length and position of a trailing edge segment and looking at how benign the aeroelastic response of a trailing edge with a certain thickness is. In addition, investigating the flexible trailing edge effect for varying wing box structures, will allow us to generalise the conclusions. Finally, the consequence of trailing edge flexibility for the steady aerodynamic loads is examined.

1.4. Outline

The outline of this report is organised in the same way as the aeroelastic model itself and the diagram in Figure 1.4 gives a quick overview. In Chapter 2 the structural model is explained, starting with a brief summary of the existing beam model in Section 2.1. The static and dynamic structural model of the trailing edge are discussed in Sections 2.2 and 2.3. The coupling between the existing beam model and the plate model is explained in Section 2.4. To prepare the structural model for the dynamic aeroelastic analysis, it is written in state-space format, explained in Section 2.5. To verify that the structural model works as it is supposed to do, verification cases are given in Section 2.6.

The existing aerodynamic model is briefly discussed in Section 3.1. Modifications required to make it compatible with the flexible trailing edge structure are then discussed in more detail in Section 3.2.

Combining both aerodynamic and structural model into the aeroelastic framework is discussed in Chapter 4, starting with the interaction between the two models in Section 4.1. Next, the static and dynamic aeroelastic models are solved in Section 4.2 and Section 4.3 respectively. Verification of the aeroelastic model is discussed in Section 4.4.

The verified aeroelastic model is now used to investigate the effect of a flexible trailing edge on the aeroelastic characteristics. All shown in Chapter 5.

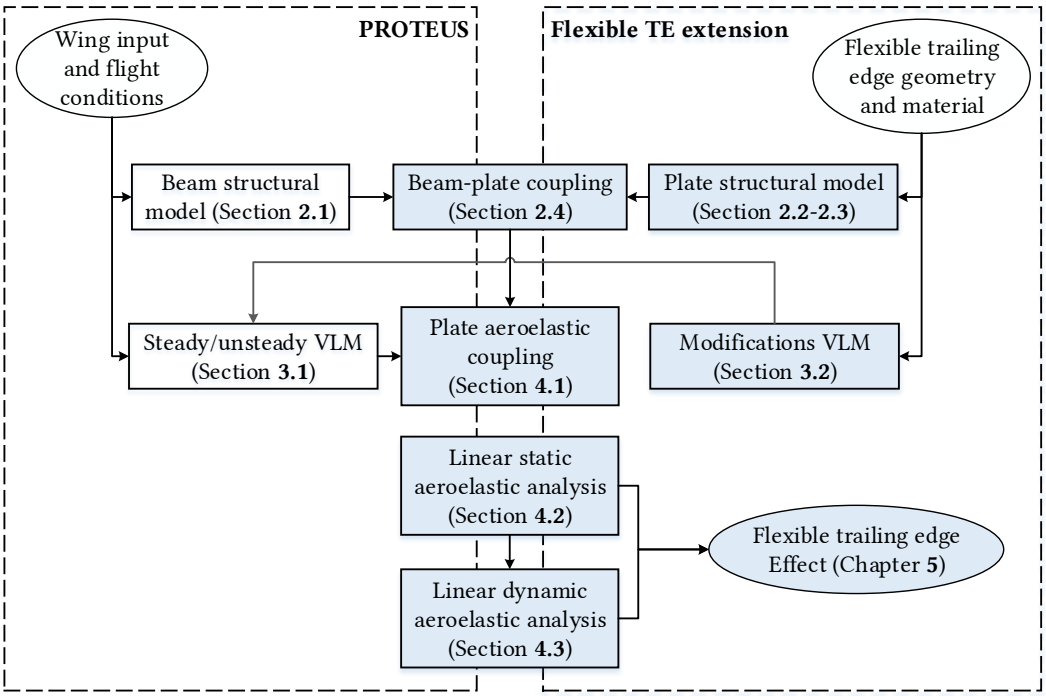

Figure 1.4: Outline of the thesis

2
Structural model

The three-dimensional structure of the wing with a flexible trailing edge is represented by a linear finite element model. The chord-wise rigid part of the wing structure is represented by beam elements, which allow span-wise bending and twisting. However, to account for the chord-wise flexibility, flat shell elements are introduced. In Figure 2.1 a schematic representation of the structural model is shown. To build this model, the flat shell elements have to be modelled, and the connection between the beam elements and the flat shell elements are created.

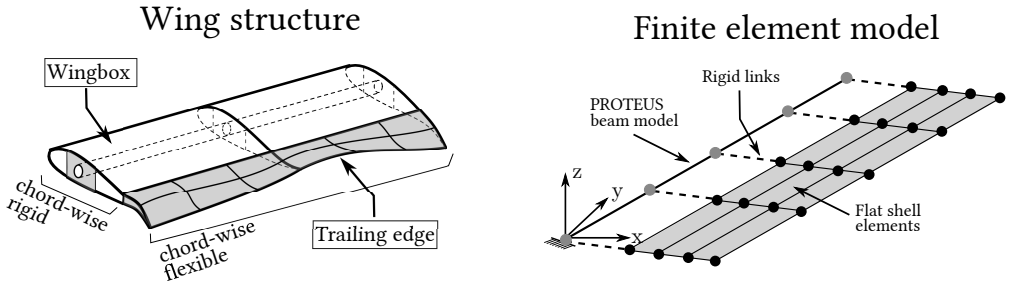

Figure 2.1: Schematic representation of the finite element model which represents the wing structure.

The PROTEUS model allows generic wing shapes to be modelled. To be compatible with the beam elements which model the wing-box structure, the flat shell elements have to satisfy the following requirements:

- The wing deflection requires both membrane and bending deformation of the trailing edge
- The same degrees of freedom as the beam elements have to be included, e.g. deformation in the x, y and z direction, and three rotations θ_x, θ_y and θ_z
- Arbitrary element shapes should be possible, allowing the model to represent a generic wing shape

Flat shell elements with 24 degrees of freedom consisting of membrane and bending stiffness are chosen as they comply with the needs stated above. Kirchhoff Plate Theory is used to model the flat shell elements, assuming that the thickness of the plate remains relatively small and transverse shear deformation is limited. A linear finite element model is chosen, assuming that the deformation of the wing remain small, such that in-plane stretching and double bending do not become significant.

In Section 2.1 a brief summary of the static and dynamic structural beam model of PROTEUS is presented. Afterwards, in Section 2.2, the static trailing edge model is explained, with a derivation of the flat shell elements, leading to the structural equilibrium equation and the stiffness matrix. Then, in Section 2.3 the mass matrix of the flat element is derived.

At this point, the stiffness and mass matrix of the uncoupled beam and trailing edge elements are computed. In Section 2.4 it is explained how these elements are connected using rigid links. The coupled structure can then be written in state-space format, shown in Section 2.5. Finally, both the flat shell elements and the coupled structure are verified. The results of this verification are presented in Section 2.6.

2.1. Structural model PROTEUS

Under the applied aerodynamic loads, the structural static and dynamic model in PROTEUS can determine the structural response of a wing with certain dimensions and properties. By converting the stiffness and mass of the wing box into one-dimensional cross-sectional beam properties, the stiffness and mass matrix of the Timoshenko beam elements are determined. The first step in the PROTEUS model is to determine the cross-sectional properties. The wing box structure is then discretised in a certain number of span-wise elements. For each of these elements the stiffness and mass matrix is determined, which are finally transformed to the global coordinate system and assembled in the global stiffness and mass matrix. This summary does not give a complete description of the model. For more details, the master thesis of Werter (2012) gives an excellent explanation.

Cross-sectional modeller

The cross-sectional modeller translates the three-dimensional cross-sectional properties into 1-dimensional beam element properties. In Figure 2.2, it can be seen how an arbitrary cross-section is discretised in a number of linear elements with constant thickness t_i and properties $\mathbf{P}_i$. The cross-sectional modeller has been developed by Ferede and Abdalla (2014), who determined the stiffness properties of a given cross-section. Werter (2012) has extended this model such that the mass properties of a cross-section can also be computed.

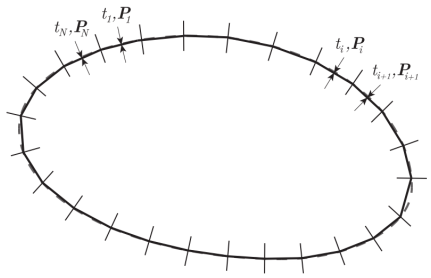

Figure 2.2: Arbitrary beam cross-section, of which the thickness and properties of each element are given by t_i and $\mathbf{P}_i$. Image courtesy of Werter (2012).

With the cross-sectional modeller, the stiffness and mass matrix of a Timoshenko beam element can be determined for thin-walled cross-sections. The cross-sectional modeller can also be bypassed, declaring cross-sectional stiffness and mass properties manually.

Discretisation of a generic wing geometry

A generic wing geometry is discretised into a number of finite elements in the following way, using Figure 2.3 for clarification. The wing is divided in one or more regions and the x,y and z coordinate and wing twist (using the chord-direction $\mathbf{c}_0$) is defined at the ends of each region.

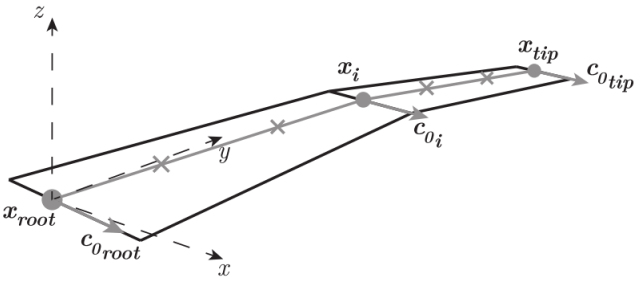

Figure 2.3: Discretisation of generic wing geometry into a number of beam elements. Image courtesy of Werter (2012).

Each region, for example between the root and point i in Figure 2.3, is discretised by a number of elements. Given the x, y and z coordinate and chord direction $\mathbf{c}_0$ at the nodes of each of the elements, the beam orientation is defined.

Static and dynamic structural model

With the cross-sectional stiffnes and mass properties, and the geometry of the beam elements defined, the stiffness and mass matrix of the finite element model can be determined.
Timoshenko beam theory is used for both the static and dynamic model. The Timoshenko stiffness matrix was determined by the cross-sectional modeller. To define the local stiffness matrix of each of the elements, 20 degrees of freedom are used, as shown in Figure 2.4.

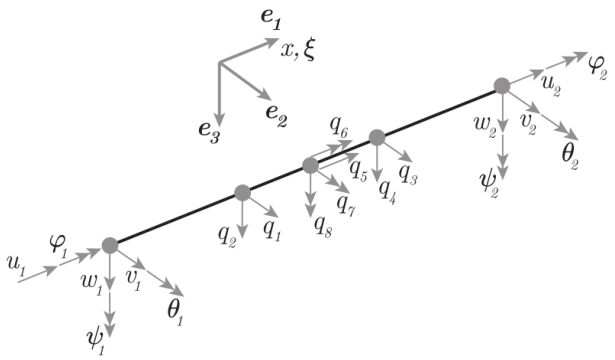

Figure 2.4: Definition of the degrees of freedom of a Timoshenko beam element. Image courtesy of Werter (2012).

All the internal degrees of freedom, given by q_1 to q_8 can be eliminated after the local stiffness matrix is determined, as no external forces are applied to these locations in the element. Similarly the local mass matrices are determined. In the PROTEUS model, the dynamic analysis can be done around a non-linear equilibrium position, by using the stiffness matrix from the non-linear static analysis. But in the present study, the dynamic analysis will use only the linear stiffness matrix of the undeformed wing structure, in order to make the combination with the flat shell elements representing the trailing edge structure more convenient.

In the end, the dynamic structural model is written in state-space format:

$$\begin{Bmatrix} \ddot{\mathbf{p}} \\ \dot{\mathbf{p}} \end{Bmatrix} = \begin{bmatrix} \mathbf{0} & -\mathbf{M}^{-1}\mathbf{K} \\ \mathbf{I} & \mathbf{0} \end{bmatrix} \begin{Bmatrix} \dot{\mathbf{p}} \\ \mathbf{p} \end{Bmatrix} + \begin{bmatrix} \mathbf{M}^{-1} \\ \mathbf{0} \end{bmatrix} \mathbf{F} \tag{2.1}$$

In which **p** contains the structural degrees of freedom, **F** are the external forces, **M** is the global mass matrix and **K** the global stiffness matrix.

2.2. Flexible trailing edge model: static analysis

The flexible plate is modelled using linear quadrilateral flat shell elements. This element is obtained by determining the local stiffness matrices of a membrane element and bending element, and then combining them. Both elements are uncoupled, but membrane-bending coupling can be included if composite laminates are used.

The shell element can have an arbitrary shape. Therefore, an isoparametric representation of the elements is used. The schematic in Figure 2.5 shows the arbitrary shape of an element, and the definition of the local coordinate system, and Figure 2.6 shows its isoparametric counterpart, using natural coordinates ξ and η.

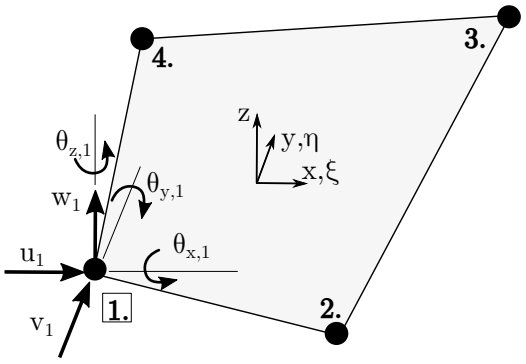

Figure 2.5: Definition of the element's local coordinate system, and the node numbering convention

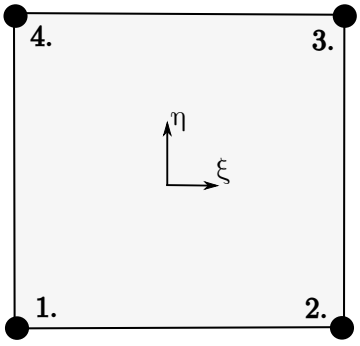

Figure 2.6: Coordinate system of the isoparametric representation

2.2.1. Mesh

The trailing edge geometry is defined as a fraction of the wing's chord length. As a consequence, the chord-wise length of the trailing edge varies in span-wise direction in the same way as the wing itself:

$$l_{TE}(y) = \mu_{TE} \cdot l_{chord}(y) \tag{2.2}$$

In span-wise direction, the trailing edge is discretised in the same number of shell elements as used for the beam model. From the beam nodes, lines are drawn in the global x direction to the trailing edge of the wing to create the 1-2 and 4-3 edges of the flat shell elements. This can be seen in Figure 2.7. The 1-4 and 2-3 edges of the wing are created by dividing the trailing edge in N_c elements of equal length in chord-wise direction.
Using the discretised wing geometry, the position of the nodes in the z direction is then found by using the following equation.

$$z_{TE,i} = z_{b,i} + \Delta x_i \tan \theta_y \tag{2.3}$$

In which $z_{b,i}$ is the z location of the corresponding beam node, Δx_i is the distance between the beam node and the node in the trailing edge mesh, and θ_y is the local twist angle.
A generic wing geometry includes the possibility of wing twist. This means that the trailing edge has a double curvature which causes warping of the elements, as depicted in Figure 2.8. The flat shell element

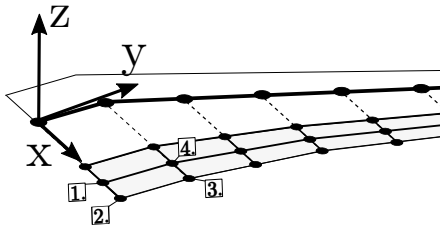

Figure 2.7: Schematic representation of the mesh of the wing structure

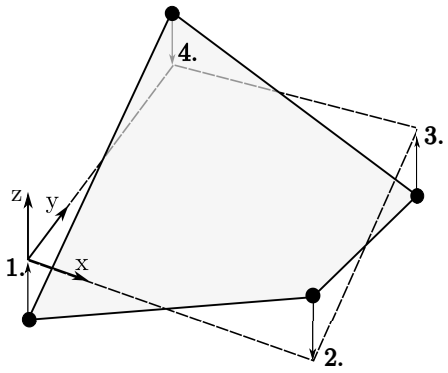

Figure 2.8: Warped geometry of the flat shell element due to wing twist

geometry is obtained by projecting the elements corner nodes on the global $x-y$ plane. The stiffness matrix of a flat shell element can be corrected in case of shell warping, but this is neglected in the present study.

2.2.2. Equilibrium equation

The equilibrium equation of a finite element is determined by using the principle of stationary potential energy, which states that equilibrium is found when $d\Pi = 0$ for every small admissible variation in the configuration. Cook and Saunders (1984) $d\Pi$ can be written as follows:

$$d\Pi = \sum_{i=1}^{12} \frac{\partial \Pi}{\partial p_i} dp_i \tag{2.4}$$

In which the Π is the total potential energy of an element, given by the sum of the elastic strain energy $\mathcal{U}$ and the work done $\mathcal{V}$:

$$\Pi = \mathcal{U} + \mathcal{V} \tag{2.5}$$

Since dp_i is an arbitrary variation in the vector of degrees of freedom $\mathbf{p}$, for $d\Pi = 0$ to hold, the following should be true:

$$\frac{\partial \Pi}{\partial p_i} = 0 \tag{2.6}$$

This results in a set of equations which can be solved to find equilibrium:

$$\mathbf{Kp} = \mathbf{F} \tag{2.7}$$

In the following two sections, the stiffness matrix for both the membrane and bending element are derived.

2.2.3. Quadrilateral membrane element

The local stiffness matrix will be determined by writing the strain energy of the membrane element as a function of the nodal deflections u and v and the drilling rotation θ_z.

The most simple membrane element is a bilinear plane element in which the displacement field within the element is written in function of the u and v displacement at each of the four nodes. A drilling

degree of freedom θ_z is added to make the element compatible with the Timoshenko beam elements of the wing box. To add θ_z, a coordinate transformation on a 8-node quadratic membrane element with mid-side nodes is carried out. Therefore, first the stiffness matrix of an 8-node quadratic membrane element is derived.

To determine the strain energy of an element, the strain field in the element has to be determined, using the nodal displacement. First the displacement field over the membrane element is found by writing them in function of the nodal displacements using the following shape functions, using natural coordinates:

$$N_1 = \frac{1}{4}(1-\xi)(1-\eta) - \frac{1}{2}(N_8 + N_5) \quad (2.8a)$$

$$N_2 = \frac{1}{4}(1+\xi)(1-\eta) - \frac{1}{2}(N_5 + N_6) \quad (2.8b)$$

$$N_3 = \frac{1}{4}(1+\xi)(1+\eta) - \frac{1}{2}(N_6 + N_7) \quad (2.8c)$$

$$N_4 = \frac{1}{4}(1-\xi)(1+\eta) - \frac{1}{2}(N_7 + N_8) \quad (2.8d)$$

$$N_5 = \frac{1}{2}(1-\xi^2)(1-\eta) \quad (2.8e)$$

$$N_6 = \frac{1}{2}(1+\xi)(1-\eta^2) \quad (2.8f)$$

$$N_7 = \frac{1}{2}(1-\xi^2)(1+\eta) \quad (2.8g)$$

$$N_8 = \frac{1}{2}(1-\xi)(1-\eta^2) \quad (2.8h)$$

The mid-side nodes are numbered as depicted in Figure 2.9.

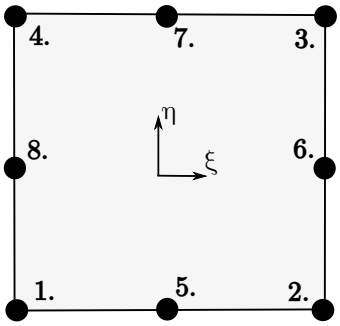

Figure 2.9: Numbering convention of the midside nodes

The displacement field over the element can be described in the following way, using the shape functions:

$$u(\xi,\eta) = \sum_{i=1}^{8} N_i u_i \quad (2.9)$$

$$v(\xi,\eta) = \sum_{i=1}^{8} N_i v_i \quad (2.10)$$

The in-plane strain field is then:

$$\varepsilon = \begin{Bmatrix} \varepsilon_x \\ \varepsilon_y \\ \gamma_{xy} \end{Bmatrix} = \begin{Bmatrix} u_{,x} \\ v_{,y} \\ u_{,y} + v_{,x} \end{Bmatrix} \quad (2.11)$$

The strains are the derivatives of the displacements with respect to the local element coordinate system (x and y). Since the element displacement field is in natural coordinates, the Jacobian matrix is required

to transform the isoparametric derivatives to the derivatives with respect to the local coordinate system:

$$\begin{Bmatrix} u_{,x} \\ v_{,y} \\ u_{,y} + v_{,x} \end{Bmatrix} = \begin{bmatrix} 1 & 0 & 0 & 0 \\ 0 & 0 & 0 & 1 \\ 0 & 1 & 1 & 0 \end{bmatrix} \begin{bmatrix} \Gamma & \mathbf{0} \\ \mathbf{0} & \Gamma \end{bmatrix} \begin{Bmatrix} u_{,\xi} \\ u_{,\eta} \\ v_{,\xi} \\ v_{,\eta} \end{Bmatrix} \tag{2.12}$$

In the expression above, Γ is the inverse of the Jacobian matrix:

$$\mathbf{J} = \begin{bmatrix} \dfrac{\partial x}{\partial \xi} & \dfrac{\partial y}{\partial \xi} \\ \dfrac{\partial x}{\partial \eta} & \dfrac{\partial y}{\partial \eta} \end{bmatrix} \tag{2.13}$$

The strain field is given in function of the in-plane nodal displacements:

$$\varepsilon = \frac{\partial N}{\partial \eta}\mathbf{p} = \mathbf{B}\mathbf{p} \tag{2.14}$$

Now that the strains are known, the strain energy of the 8-node membrane element can be calculated:

$$\mathcal{U} = \frac{1}{2}\int_{-1}^{1}\int_{-1}^{1} \mathbf{p}^T\mathbf{B}^T\mathbf{Q}\mathbf{B}\mathbf{p}\, t\, J d\eta d\xi \tag{2.15}$$

In the above equation, $\mathbf{Q}$ is the material constitutive matrix, linking stress to strain. For isotropic material, is is given by the following equation:

$$\mathbf{Q} = \frac{E}{1-\nu^2}\begin{bmatrix} 1 & \nu & 0 \\ \nu & 1 & 0 \\ 0 & 0 & \dfrac{1-\nu}{2} \end{bmatrix} \tag{2.16}$$

J is the determinant of the Jacobian matrix, which is added because the original integral expression is given within the boundaries of the local coordinate system. Furthermore, t is the thickness of the plate. For composite materials, the strain energy is determined using the in-plane stiffness matrix $\mathbf{A}$, computed using classical lamination theory. In Appendix A, a derivation of the ABD matrix is given, which relates the mid-plane strains and curvatures of the laminate to the stress resultants. The $\mathbf{A}$ matrix relates mid-plane strains to the in-plane stress resultants:

$$\begin{Bmatrix} N_x \\ N_y \\ N_{xy} \end{Bmatrix} = \begin{bmatrix} A_{11} & A_{12} & A_{16} \\ A_{12} & A_{22} & A_{26} \\ A_{16} & A_{26} & A_{66} \end{bmatrix} \begin{Bmatrix} \varepsilon_x^0 \\ \varepsilon_y^0 \\ \gamma_{xy}^0 \end{Bmatrix} \tag{2.17}$$

The strain energy of a membrane element can be written using stress resultants instead of stresses, noting that the through the thickness integration of the element is already accounted for by the $\mathbf{A}$ matrix:

$$\mathcal{U} = \frac{1}{2}\int_{-1}^{1}\int_{-1}^{1} \mathbf{p}^T\mathbf{B}^T\mathbf{A}\mathbf{B}\mathbf{p}\, J d\eta d\xi \tag{2.18}$$

Using Equation (2.4), the membrane element stiffness matrix is computed as follows:

$$\mathbf{k_m} = \int_{-1}^{1}\int_{-1}^{1} \mathbf{B}^T\mathbf{A}\mathbf{B}\, J d\eta d\xi \tag{2.19}$$

Integration of the stiffness matrix is done using numerical integration. The numerical integration scheme used is second-order Gauss quadrature, which can integrate a 3^{rd} order polynomial, like the shape functions used, exactly. The expression is evaluated at four locations, as shown in the following figure:

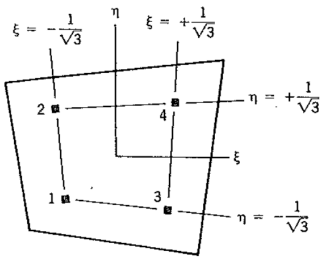

Figure 2.10: Locations and weights of the integration points. Image courtesy of Cook and Saunders (1984)

Hence, the stiffness matrix of the membrane element is calculated as follows:

$$\mathbf{k_m} = \sum_{i=1}^{4} w_i \left[\mathbf{B}^T(\xi_i, \eta_i)\mathbf{Q}\mathbf{B}(\xi_i, \eta_i)\, t\, J\right], \qquad w_i = \pm 1/\sqrt{3} \tag{2.20}$$

Drilling degrees of freedom

Now that the stiffness matrix is found, a coordinate transformation is performed to transform the stiffness matrix of an 8 node quadrilateral membrane element in a 4-node quadrilateral element with drilling degrees of freedom. The Allman triangle approach found by Cook (1986) is followed: the displacement of the mid-side nodes makes it possible to define a quadratic displacement field in the element. The drilling degrees of freedom in the corner nodes can replace the displacement degrees of freedom in the mid-side nodes while maintaining a quadratic displacement field. This can best be explained by the schematic in Figure 2.11.

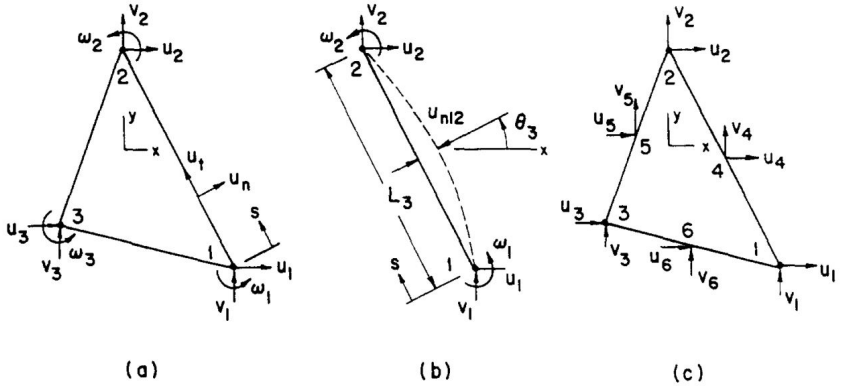

Figure 2.11: (a) Nodal d.o.f. of the Allman triangle. (b) Parabolic edge displacement created by d.o.f. ω_1 and ω_2. (c) D.o.f. of the linear strain triangle (LST). Schematic taken from Cook (1986)

Using the schematic in Figure 2.11, the mid-side node displacement in x-direction at node 5 can be written in function of the drilling degrees of freedom at node 1 and 2:

$$u_5 = \frac{1}{2}u_1 + \frac{1}{2}u_2 + \frac{y_2 - y_1}{8}(\theta_{z,2} - \theta_{z,1}) \tag{2.21}$$

In which y_1 and y_2 are the location of node 1 and 2 in y-direction. Note that the transformation takes place in the local coordinate system, and not in the isoparametric coordinate system. A similar expression can be written for the mid-side node displacements in y-direction. Writing all the mid-side node displacement in function of the DOF's at the corner node yields the transformation matrix $\mathbf{T_{AT}}$ which carries out the transformation between the Q8 element and the Q4 element with drilling DOF's:

$$\begin{Bmatrix} u_5 \\ v_5 \\ u_6 \\ \vdots \\ v_8 \end{Bmatrix} = \mathbf{T_{AT}} \begin{Bmatrix} u_1 \\ v_1 \\ \theta_{z,1} \\ \vdots \\ \theta_{z,4} \end{Bmatrix} \tag{2.22}$$

The stiffness matrix of the 4-node element with drilling DOF's is retrieved by using the transformation matrix $\mathbf{T_{AT}}$:

$$\mathbf{k_{Q4}} = \mathbf{T_{AT}}^T \mathbf{k_{Q8}} \mathbf{T_{AT}} \tag{2.23}$$

2.2.4. Quadrilateral bending element

Just like the membrane element, the strain energy of the bending element is first computed in order to find the stiffness matrix. The bending element chosen is based on Kirchhoff plate theory. This theory assumes that the mid-plane does not deform under bending, and that lines perpendicular to the mid-plane remain both straight and normal to that mid-plane. Also, strains in thickness direction are neglected. With these assumptions the in-plane strains can be written in function of the out-of-plane displacement w in the following way:

$$\varepsilon = \begin{Bmatrix} \varepsilon_x \\ \varepsilon_y \\ \gamma_{xy} \end{Bmatrix} = \begin{Bmatrix} -h\dfrac{\partial^2 w}{\partial x^2} \\ -h\dfrac{\partial^2 w}{\partial y^2} \\ -2h\dfrac{\partial^2 w}{\partial x \partial y} \end{Bmatrix} \tag{2.24}$$

The out-of-plane strains ε_z, γ_{yz} and γ_{xz} are zero. In the above expression, h is the distance from the mid-plane to the location in the plane at which the strain is computed, in out-of-plane direction z, depicted in Figure 2.12.

The strains in the plate can be determined from the out-of-plane displacement w, which can be written in function of the nodal degrees of freedom w, $w_{,x}$ and $w_{,y}$. Note that $w_{,x} = -\theta_y$ and $w_{,y} = -\theta_x$. The shape functions of a Kirchhoff plate element can simply be found by solving for the twelve coefficients of a function with 10 cubic and 2 quartic terms, given in Equation (2.25).

$$w = [1,\ \xi,\ \eta,\ \xi^2,\ \xi\eta,\ \eta^2,\ \xi^3,\ \xi^2\eta,\ \xi\eta^2,\ \eta^3,\ \xi^3\eta,\ \xi\eta^3] \begin{Bmatrix} a_1 \\ a_2 \\ \vdots \\ a_{12} \end{Bmatrix} \tag{2.25}$$

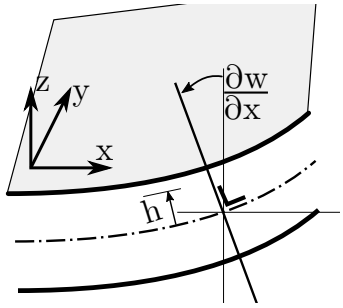

Figure 2.12: Schematic of the Kirchhoff plate theory: the mid-plane does not deform and the normal to that mid-plane remains normal and straight

The following set of shape functions is found:

$$N_1 = -\left(\frac{\eta}{8} - \frac{1}{8}\right)(\xi - 1)\left(\eta^2 + \xi^2 + \eta + \xi - 2\right) \tag{2.26a}$$

$$N_2 = -\left(\frac{\xi}{8} + \frac{1}{8}\right)(\xi - 1)^2(\eta - 1) \tag{2.26b}$$

$$N_3 = -\left(\frac{\eta}{8} + \frac{1}{8}\right)(\eta - 1)^2(\xi - 1) \tag{2.26c}$$

$$N_4 = \left(\frac{\eta}{8} - \frac{1}{8}\right)(\xi + 1)\left(\eta^2 + \xi^2 + \eta - \xi - 2\right) \tag{2.26d}$$

$$N_5 = -\left(\frac{\xi}{8} - \frac{1}{8}\right)(\xi + 1)^2(\eta - 1) \tag{2.26e}$$

$$N_6 = \left(\frac{\eta}{8} + \frac{1}{8}\right)(\eta - 1)^2(\xi + 1) \tag{2.26f}$$

$$N_7 = -\left(\frac{\eta}{8} + \frac{1}{8}\right)(\xi + 1)\left(\eta^2 + \xi^2 - \eta - \xi - 2\right) \tag{2.26g}$$

$$N_8 = \left(\frac{\xi}{8} - \frac{1}{8}\right)(\xi + 1)^2(\eta + 1) \tag{2.26h}$$

$$N_9 = \left(\frac{\eta}{8} - \frac{1}{8}\right)(\eta + 1)^2(\xi + 1) \tag{2.26i}$$

$$N_{10} = \left(\frac{\eta}{8} + \frac{1}{8}\right)(\xi - 1)\left(\eta^2 + \xi^2 - \eta + \xi - 2\right) \tag{2.26j}$$

$$N_{11} = \left(\frac{\xi}{8} + \frac{1}{8}\right)(\xi - 1)^2(\eta + 1) \tag{2.26k}$$

$$N_{12} = -\left(\frac{\eta}{8} - \frac{1}{8}\right)(\eta + 1)^2(\xi - 1) \tag{2.26l}$$

The out-of-plane displacement field over the element can be described in the following way, using the shape functions:

$$w(\xi, \eta) = \sum_{i=1}^{12} N_i q_i \tag{2.27}$$

In which q_i are the nodal unknowns w_1, $w_{,x,1}$, $w_{,y,1}$, up to , $w_{,x,4}$. The strain field is then the derivative with respect to the x and y coordinates using Equation (2.24). Since the displacement field is written in

natural coordinates ξ and η, a second order Jacobian matrix is required for the coordinate transformation. For a Kirchhoff plate element, a method to determine the required coordinate transformation was developed by Ming and Fa (1987).

Second-order Jacobian

Just like for the membrane element, the matrix $\mathbf{B}$ relates the displacement field to the strain field in the following way: $\boldsymbol{\epsilon} = \mathbf{Bp}$. Following the approach of the above mentioned reference, $\mathbf{B}$ is calculated in the following way:

$$\mathbf{B_i} = \mathbf{AC_i} \tag{2.28}$$

With $i = 1, 2, 3, 4$, one for each node. In which $\mathbf{A}$ is:

$$\mathbf{A} = \frac{-1}{J^2}\begin{bmatrix} \left(\frac{\partial y}{\partial \eta}\right)^2 & \left(\frac{\partial y}{\partial \xi}\right)^2 & -2\frac{\partial y}{\partial \xi}\frac{\partial y}{\partial \eta} \\ \left(\frac{\partial x}{\partial \eta}\right)^2 & \left(\frac{\partial x}{\partial \xi}\right)^2 & -2\frac{\partial x}{\partial \xi}\frac{\partial x}{\partial \eta} \\ -2\frac{\partial x}{\partial \eta}\frac{\partial y}{\partial \eta} & -2\frac{\partial x}{\partial \xi}\frac{\partial y}{\partial \xi} & 2\left(\frac{\partial x}{\partial \xi}\frac{\partial y}{\partial \eta} + \frac{\partial x}{\partial \eta}\frac{\partial y}{\partial \xi}\right) \end{bmatrix} \tag{2.29}$$

In the equation above, J is the determinant of the first-order Jacobian, given by Equation (2.13). And $\mathbf{C_i}$ is:

$$\mathbf{C_i} = \begin{bmatrix} \frac{\partial^2 N_i}{\partial \xi^2} & \frac{\partial^2 N_{,xi}}{\partial \xi^2} & \frac{\partial^2 N_{,yi}}{\partial \xi^2} \\ \frac{\partial^2 N_i}{\partial \eta^2} & \frac{\partial^2 N_{,xi}}{\partial \eta^2} & \frac{\partial^2 N_{,yi}}{\partial \eta^2} \\ \frac{\partial^2 N_i}{\partial \xi \partial \eta} - \alpha'\frac{\partial N_i}{\partial \xi} + \beta'\frac{\partial N_i}{\partial \eta} & \frac{\partial^2 N_{,xi}}{\partial \xi \partial \eta} - \alpha'\frac{\partial N_{,xi}}{\partial \xi} + \beta'\frac{\partial N_{,xi}}{\partial \eta} & \frac{\partial^2 N_{,yi}}{\partial \xi \partial \eta} - \alpha'\frac{\partial N_{,yi}}{\partial \xi} + \beta'\frac{\partial N_{,yi}}{\partial \eta} \end{bmatrix} \tag{2.30}$$

With α' and β':

$$\alpha' = \left(\alpha\frac{\partial y}{\partial \eta} - \beta\frac{\partial x}{\partial \eta}\right) \Big/ J \tag{2.31}$$

$$\beta' = \left(\alpha\frac{\partial y}{\partial \xi} - \beta\frac{\partial x}{\partial \xi}\right) \Big/ J \tag{2.32}$$

In which α and β are:

$$\alpha = \sum_{i=1}^{4} \frac{\xi_i \eta_i}{4} x_i = \frac{x_1 - x_2 - x_4 + x_3}{4} \tag{2.33}$$

$$\beta = \sum_{i=1}^{4} \frac{\xi_i \eta_i}{4} y_i = \frac{y_1 - y_2 - y_4 + y_3}{4} \tag{2.34}$$

Stiffness matrix

The strain energy of a plate element in bending is given by:

$$\mathcal{U} = \frac{1}{2}\int_{-1}^{1}\int_{-1}^{1} \mathbf{p}^T\mathbf{B}^T\mathbf{D}\mathbf{B}\mathbf{p}\, J d\eta d\xi \tag{2.35}$$

For an isotropic material, the flexural rigidity of a plate is given by:

$$\mathbf{D} = \frac{Et^3}{12\left(1-\nu^2\right)} \begin{bmatrix} 1 & \nu & 0 \\ \nu & 1 & 0 \\ 0 & 0 & \dfrac{1-\nu}{2} \end{bmatrix} \tag{2.36}$$

For composite materials, the strain energy is determined using the out-of-plane stiffness matrix $\mathbf{D}$, which relates curvatures to the moment resultants:

$$\begin{Bmatrix} M_x \\ M_y \\ M_{xy} \end{Bmatrix} = \begin{bmatrix} D_{11} & D_{12} & D_{16} \\ D_{12} & D_{22} & D_{26} \\ D_{16} & D_{26} & D_{66} \end{bmatrix} \begin{Bmatrix} \kappa_x \\ \kappa_y \\ \kappa_{xy} \end{Bmatrix} \tag{2.37}$$

Again in a similar way as for the membrane element, the stiffness matrix can subsequently be calculated using the following equation and Gauss quadrature:

$$\mathbf{k_b} = \int_{-1}^{1}\int_{-1}^{1} \mathbf{B}^T \mathbf{D}\, \mathbf{B}\, J d\eta d\xi \tag{2.38}$$

2.2.5. Shell stiffness matrix

The local stiffness matrix of the total shell element is found by combining the local stiffness matrix of the membrane and bending element:

$$\mathbf{k_s} = \begin{bmatrix} \mathbf{k_m} & \mathbf{0} \\ \mathbf{0} & \mathbf{k_b} \end{bmatrix} \tag{2.39}$$

The arrangement of degrees of freedom that match the above stiffness matrix is:

$$\mathbf{p} = \begin{Bmatrix} u \\ v \\ \theta_z \\ w \\ w_{,x} \\ w_{,y} \end{Bmatrix} \tag{2.40}$$

Before transforming the stiffness matrix to the global coordinate system, it will be rearranged to match the global degrees of freedom arrangement, including the change from $w_{,x}$ and $w_{,y}$ to θ_x and θ_y :

$$\begin{Bmatrix} u \\ v \\ \theta_z \\ w \\ w_{,x} \\ w_{,y} \end{Bmatrix} = \underbrace{\begin{bmatrix} 1 & 0 & 0 & 0 & 0 & 0 \\ 0 & 1 & 0 & 0 & 0 & 0 \\ 0 & 0 & 0 & 0 & 0 & 1 \\ 0 & 0 & 1 & 0 & 0 & 0 \\ 0 & 0 & 0 & 0 & -1 & 0 \\ 0 & 0 & 0 & -1 & 0 & 0 \end{bmatrix}}_{\mathbf{T_{shell}}} \begin{Bmatrix} u \\ v \\ w \\ \theta_x \\ \theta_y \\ \theta_z \end{Bmatrix} \tag{2.41}$$

The local shell stiffness matrix is therefore:

$$\mathbf{k_s} = \mathbf{T_{shell}^T} \begin{bmatrix} \mathbf{k_m} & \mathbf{0} \\ \mathbf{0} & \mathbf{k_b} \end{bmatrix} \mathbf{T_{shell}} \tag{2.42}$$

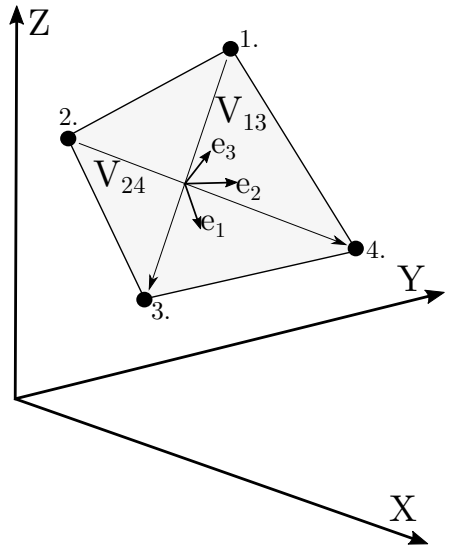

Figure 2.13: Definition of the local coordinate system of the shell element

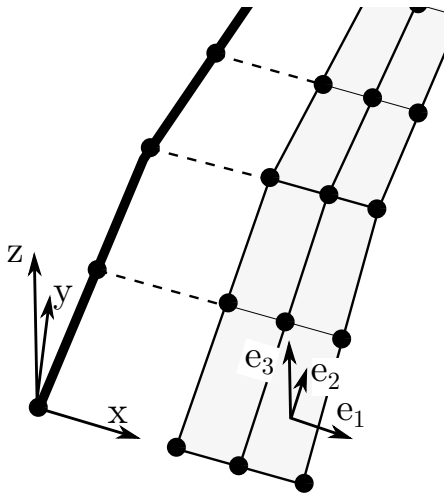

Figure 2.14: Definition of the local coordinate system of the shell element shown in context of the complete wing structure

2.2.6. Local to global coordinate transformation

In Figure 2.13, the definition of the local shell coordinate system in the global coordinate system is given. To define e_1, e_2 and e_3, the following procedure is followed:

First, the 1 direction vector is defined as the normalised sum of vectors $\mathbf{v_{13}}$ and $\mathbf{v_{24}}$, which are depicted in Figure 2.13.

$$\mathbf{e_1} = \frac{\mathbf{v_{13}} + \mathbf{v_{24}}}{|\mathbf{v_{13}} + \mathbf{v_{24}}|} \tag{2.43}$$

Then, a temporary direction vector $\mathbf{e_2^*}$ is constructed to make sure that the $\mathbf{e_3}$ direction vector is normal to the $\mathbf{e_1}$ direction vector.

$$\mathbf{e_2^*} = \frac{\mathbf{v_{13}} - \mathbf{v_{24}}}{|\mathbf{v_{13}} + \mathbf{v_{24}}|} \tag{2.44}$$

The $\mathbf{e_3}$ direction vector is then the cross product of the two previously defined direction vectors $\mathbf{e_1}$ and $\mathbf{e_2^*}$:

$$\mathbf{e_3} = \frac{\mathbf{e_1} \times \mathbf{e_2^*}}{|\mathbf{e_1} \times \mathbf{e_2^*}|} \tag{2.45}$$

At last, also the $\mathbf{e_2}$ can be defined:

$$\mathbf{e_2} = \frac{\mathbf{e_3} \times \mathbf{e_1}}{|\mathbf{e_3} \times \mathbf{e_1}|} \tag{2.46}$$

When the local coordinate system is defined in function of the global coordinate system, a rotation matrix can be assembled containing the x, y and z components of the direction vectors.

$$\mathbf{R_1} = \begin{bmatrix} e_{1,x} & e_{2,x} & e_{3,x} \\ e_{1,y} & e_{2,y} & e_{3,y} \\ e_{1,z} & e_{2,z} & e_{3,z} \end{bmatrix} \tag{2.47}$$

A rotation matrix can transform a set of translational or rotational degrees of freedom in the following way:

$$\begin{Bmatrix} u_g \\ v_g \\ w_g \end{Bmatrix} = \mathbf{R_1} \begin{Bmatrix} u_l \\ v_l \\ w_l \end{Bmatrix} \tag{2.48}$$

$$\begin{Bmatrix} \theta_{x,g} \\ \theta_{y,g} \\ \theta_{z,g} \end{Bmatrix} = \mathbf{R_1} \begin{Bmatrix} \theta_{x,l} \\ \theta_{y,l} \\ \theta_{z,l} \end{Bmatrix} \tag{2.49}$$

Recall that the degrees of freedom of the shell element are arranged in the following manner:

$$\mathbf{p_l} = \begin{Bmatrix} u_1 \\ v_1 \\ w_1 \\ \theta_{x,1} \\ \theta_{y,1} \\ \theta_{z,1} \\ \\ u_2 \\ \vdots \\ \theta_{z,4} \end{Bmatrix} \tag{2.50}$$

Hence, the rotation matrix to transform the entire stiffness matrix of the shell element can be assembled by inserting $\mathbf{R_1}$ on the diagonal of a 24 by 24 matrix, in which the translational and rotational degrees of freedom at each of the 4 nodes are rotated independently:

$$\mathbf{R} = \begin{bmatrix} \mathbf{R_1} & & & & & & & & \\ & \mathbf{R_1} & & & & & & & \\ & & \mathbf{R_1} & & & & & & \\ & & & \mathbf{R_1} & & & & & \\ & & & & \mathbf{R_1} & & & & \\ & & & & & \mathbf{R_1} & & & \\ & & & & & & \mathbf{R_1} & & \\ & & & & & & & \mathbf{R_1} & \\ & & & & & & & & \mathbf{R_1} \end{bmatrix} \tag{2.51}$$

Finally, the shell stiffness matrix is transformed to the global coordinate system in the following way:

$$\mathbf{k_{s,g}} = \mathbf{R^T k_{s,l} R} \tag{2.52}$$

Afterwards, the element stiffness matrices can be assembled in the total stiffness matrix $\mathbf{K_s}$.

2.3. Flexible trailing edge model: dynamic analysis

First, the kinetic energy of both the membrane and bending element is derived in function of the nodal degrees of freedom. Afterwards, Hamilton's principle is used to determine the equation of motion and the mass matrix.

2.3.1. Kinetic energy bending element

The kinetic energy of a plate in bending is given by the following expression:

$$\mathcal{T} = \frac{1}{2}\int_{V_e} \rho \dot{\mathbf{u}}^2 dV_e \tag{2.53}$$

In an orthogonal coordinate system, the square of vector $\dot{\mathbf{u}}$ can be written as the sum of its components squared:

$$\mathcal{T} = \frac{1}{2}\int_{V_e} \rho \left(\dot{u}^2 + \dot{v}^2 + \dot{w}^2\right) dV_e \tag{2.54}$$

The in-plane velocities $\dot{u}$ and $\dot{v}$ are a function of the rotations $w_{,y}$ and $w_{,x}$. Following the sign convention, the kinetic energy can be rewritten:

$$\mathcal{T} = \frac{1}{2}\int_{V_e} \rho \left(z^2 \cdot \dot{w}_{,y}^2 + z^2 \cdot \dot{w}_{,x}^2 + \dot{w}^2\right) dV_e \tag{2.55}$$

Integrating over the thickness of the element, in the z direction, yields:

$$\mathcal{T} = \frac{1}{2}\int_{A_e} \rho \left(t \cdot \dot{w}^2 + \frac{t^3}{12} \cdot \dot{w}_{,y}^2 + \frac{t^3}{12} \cdot \dot{w}_{,x}^2\right) dA_e \tag{2.56}$$

The variables w, $w_{,x}$ and $w_{,y}$ can be written in function of the nodal degrees of freedom using the same shape functions N_i which were used for the stiffness matrix, resulting in a so called consistent mass matrix. The kinetic energy of the bending element is therefore:

$$\mathcal{T} = \frac{1}{2}\int_{A} \dot{\mathbf{p_b}}^T \mathbf{N_b}^T \mathbf{I_b} \mathbf{N_b}\, \dot{\mathbf{p_b}}\, dA \tag{2.57}$$

In which $\dot{\mathbf{p_b}}$ and $\mathbf{I_b}$ are given by:

$$\dot{\mathbf{p_b}} = \begin{Bmatrix} w \\ \dot{w}_{,x} \\ \dot{w}_{,y} \end{Bmatrix} \tag{2.58}$$

$$\mathbf{I_b} = \begin{bmatrix} \rho t & 0 & 0 \\ 0 & \frac{1}{12}\rho t^3 & 0 \\ 0 & 0 & \frac{1}{12}\rho t^3 \end{bmatrix} \tag{2.59}$$

2.3.2. Kinetic energy membrane element

The kinetic energy of the membrane element is more straightforward. Similarly as for the bending element, a consistent mass matrix is computed using the shape functions of the membrane element:

$$\mathcal{T} = \frac{1}{2} t \int_{A} \dot{\mathbf{p_m}}^T \mathbf{N_m}^T \mathbf{N_m}\, \dot{\mathbf{p_m}}\, dA \tag{2.60}$$

with $\dot{\mathbf{p_m}}$ given by:

$$\dot{\mathbf{p_m}} = \begin{Bmatrix} u \\ v \\ \theta_z \end{Bmatrix} \tag{2.61}$$

2.3.3. Equation of motion and mass matrix

When the kinetic energy of the plate element is completely defined, Hamilton's principle is used to derive the equation of motion. The Euler-Lagrange equation is given by:

$$\frac{d}{dt}\left(\frac{\partial \mathcal{L}}{\partial \dot{\mathbf{p}}}\right) - \frac{\partial \mathcal{L}}{\partial \mathbf{p}} = 0 \tag{2.62}$$

In which $\mathcal{L}$ is the lagrangian, given by $\mathcal{L} = \mathcal{T} - \Pi$. The potential energy used to derive the equilibrium equation has been derived in section 2.2. Substituting the kinetic and potential energy into Equation (2.62), yields the equation of motion:

$$\mathbf{M}\ddot{\mathbf{p}} + \mathbf{K}\mathbf{p} = \mathbf{F} \tag{2.63}$$

The stiffness matrix $\mathbf{K}$ was derived in the previous section and the mass matrix $\mathbf{M}$ for the membrane and bending part of the flat shell element is given by the following equations:

$$\mathbf{M_m} = \int_{-1}^{1}\int_{-1}^{1} \mathbf{N_m}^T \mathbf{N_m} J d\xi d\eta \tag{2.64}$$

$$\mathbf{M_b} = \int_{-1}^{1}\int_{-1}^{1} \mathbf{N_b}^T \mathbf{I_b} \mathbf{N_b} J d\xi d\eta \tag{2.65}$$

The construction of the flat shell element's mass matrix, and the assembly in the global mass matrix is done in a similar way as was done for the stiffness matrix.

2.4. Coupling of the trailing edge to the wing-box

In this section, the structural coupling between the flexible trailing edge and the wing box structure is explained. Since there is an offset between the reference axis of the beam elements representing the wing box structure and the plate elements representing the trailing edge, these elements cannot share the same degrees of freedom. The displacement and rotation of these nodes can be related, since the airfoil is assumed to be rigid up to the start of the trailing edge.

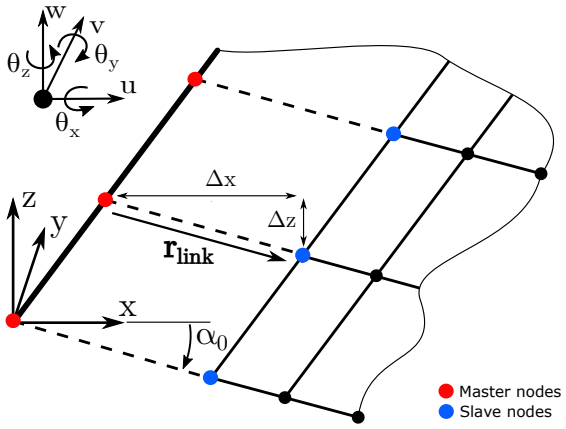

Figure 2.15: Schematic representation of the rigid link between the beam and plate nodes

Firstly, it is discussed why the master-slave approach is chosen as coupling mechanism. Afterwards, the derivation of the coupled stiffness and mass matrices is elaborated.

2.4.1. Different coupling methods

Different methods can be used to enforce the relation between these nodes. At one hand, multi point constraints, which can be implemented using penalty functions, Lagrange multipliers or master-slave elimination and on the other hand beam elements.

Beam elements with high stiffness and a low mass could represent the connection between the beam and plate structures, but increasing the stiffness of the beam elements such that they do not deform too much under the applied loads can cause ill-conditioning of the global stiffness matrix, limiting the accuracy of this method. Multi-point constraints define how two degrees of freedom behave with respect to each other. In this case, they couple the plate nodes to the beam nodes of which the meshes do not match due the offset between the beam's reference axis and the trailing edge.

In the different methods to implement multi-point constraints, a constraint equation defines the relation between two or more degrees of freedom. Penalty functions work by adding penalty elements to the total stiffness matrix. The "penalty" stiffness applied to these elements is chosen such that the constraint equation is approximated. No additional degrees of freedom are added but the weight of the penalty stiffness has to be scaled to approximate the the constraint equation, and the total stiffness matrix becomes more ill-conditioned, reducing accuracy. When Lagrange multipliers are used, the constraint equations are satisfied perfectly. Lagrange multipliers are unknowns that act as a force couple which ensures that the constraint equations are satisfied. The disadvantage is that they add additional degrees of freedom, one for every constraint equation, to the set of degrees of freedom, increasing computational time. The third method is the master-slave approach. With this approach, the slave degrees of freedom (in this case the degrees of freedom related to the nodes at the leading edge of the plate) are written in function of the master degrees of freedom (in this case the beam degrees of freedom). The advantage is that the slave degrees of freedom can be eliminated from the set of global degrees of freedom, reducing computational time. The disadvantage is that they cannot model non-linear constraints, which the two methods above can, but for the present model, this is not needed. Hence, the master-slave approach is chosen.

2.4.2. Rigid links using the master-slave approach

Using the master-slave approach, the translational degrees of freedom corresponding to the first row of plate nodes (slave) are related to the beam translational degrees of freedom (master) in the following way:

$$\boldsymbol{u_p} = \boldsymbol{u_b} + \boldsymbol{\theta_b} \times \boldsymbol{r_{link}} \tag{2.66}$$

The rotational degrees of freedom of the slave nodes are simply equal to those of the master nodes:

$$\boldsymbol{\theta_p} = \boldsymbol{\theta_b} \tag{2.67}$$

In Equation (2.66), $\boldsymbol{r_{link}}$ is the distance vector between the beam and the plate node, as depicted in Figure 2.15. In the present structural model, it is assumed that the rigid links remain in the $x-z$ plane. Therefore, the distance vector of the link is given by the following expression:

$$\boldsymbol{r_{link}} = \begin{Bmatrix} L_{link}\cos\alpha_0 \\ 0 \\ L_{link}\sin\alpha_0 \end{Bmatrix} = \begin{Bmatrix} \Delta x \\ 0 \\ \Delta z \end{Bmatrix} \tag{2.68}$$

In combination with the small angle assumption, the transformation matrix relating the slave to the master degrees of freedom is given by Equation (2.69).

$$\begin{Bmatrix} u_p \\ v_p \\ w_p \\ \theta_{x,p} \\ \theta_{y,p} \\ \theta_{z,p} \end{Bmatrix} = \underbrace{\begin{bmatrix} 1 & 0 & 0 & 0 & -\Delta z & 0 \\ 0 & 1 & 0 & 0 & 0 & \Delta x \\ 0 & 0 & 1 & 0 & -\Delta x & 0 \\ 0 & 0 & 0 & 1 & 0 & 0 \\ 0 & 0 & 0 & 0 & 1 & 0 \\ 0 & 0 & 0 & 0 & 0 & 1 \end{bmatrix}}_{\mathbf{T}_{\mathbf{ms}}^{*}} \begin{Bmatrix} u_b \\ v_b \\ w_b \\ \theta_{x,b} \\ \theta_{y,b} \\ \theta_{z,b} \end{Bmatrix} \tag{2.69}$$

The above transformation matrix $\mathbf{T_{ms}}$ is defined in the global coordinate system. The transformation from the full set of degrees of freedom to the reduced set takes place after the stiffness and mass matrix of both the beam and the plate elements, which are not connected to each other at that moment, are assembled. The following expressions show how this is done:

$$\begin{Bmatrix} \mathbf{p_{b,master}} \\ \mathbf{p_{p,slave}} \\ \mathbf{p_{p,free}} \end{Bmatrix} = \underbrace{\begin{bmatrix} \mathbf{I} & \mathbf{0} \\ \mathbf{T_{ms}^{*}} & \mathbf{0} \\ \mathbf{0} & \mathbf{I} \end{bmatrix}}_{\mathbf{T_{ms}}} \begin{Bmatrix} \mathbf{p_{b,master}} \\ \mathbf{p_{p,free}} \end{Bmatrix} \tag{2.70}$$

At last, the coupling of the structure is achieved by transforming the stiffness and mass matrices containing both master, slave and free degrees of freedom, called full matrices $\mathbf{K}^{\star}$ and $\mathbf{M}^{\star}$ into the reduced stiffness and mass matrices. This can be done in the following way Cook and Saunders (1984):

$$\mathbf{K} = \mathbf{T_{ms}^{T}} \mathbf{K}^{\star} \mathbf{T_{ms}} \tag{2.71}$$

$$\mathbf{M} = \mathbf{T_{ms}^{T}} \mathbf{M}^{\star} \mathbf{T_{ms}} \tag{2.72}$$

2.5. State-space system of the coupled structure

In a state-space system, a set of higher order differential equations is reduced to first-order differential equations, written as a set of state, input and output variables. For a continuous time-invariant state-space model, the state equation is given by Equation (2.73) Ogata (2010):

$$\dot{\mathbf{x}} = \mathbf{A}\mathbf{x} + \mathbf{B}\mathbf{u} \tag{2.73}$$

In which $\mathbf{x}$ is the vector containing the state variables and $\mathbf{u}$ is the input vector. Matrix $\mathbf{A}$ is the so called state matrix. The state-space system is completed with the output equation, written as follows:

$$\mathbf{y} = \mathbf{C}\mathbf{x} + \mathbf{D}\mathbf{u} \tag{2.74}$$

In which $\mathbf{y}$ are the output variables. As stated in Section 2.3, the equation of motion of a linear dynamic system is given by the following expression:

$$\mathbf{M}\ddot{\mathbf{p}} + \mathbf{K}\mathbf{p} = \mathbf{F} \tag{2.75}$$

Before writing the equations of motion in state-space format, the transformation to the reduced set of degrees of freedom using the master-slave transformation matrix has to be done. In the above equation, the stiffness and mass matrix are given by:

$$\mathbf{K} = \mathbf{T_{ms}^{T}} \mathbf{K}^{\star} \mathbf{T_{ms}} \tag{2.76}$$

$$\mathbf{M} = \mathbf{T}_{\mathbf{ms}}^{\mathbf{T}} \mathbf{M}^{\star} \mathbf{T}_{\mathbf{ms}} \tag{2.77}$$

The equations of motion can then be written in state-space format, by including $\dot{\mathbf{p}}$ in the vector of state variables. This results in the following state equation:

$$\begin{Bmatrix} \ddot{\mathbf{p}} \\ \dot{\mathbf{p}} \end{Bmatrix} = \begin{bmatrix} \mathbf{0} & -\mathbf{M}^{-1}\mathbf{K} \\ \mathbf{I} & \mathbf{0} \end{bmatrix} \begin{Bmatrix} \dot{\mathbf{p}} \\ \mathbf{p} \end{Bmatrix} + \begin{bmatrix} \mathbf{M}^{-1} \\ \mathbf{0} \end{bmatrix} \mathbf{F} \tag{2.78}$$

As explained in Section 2.4, the master-slave transformation matrix describes the kinematic relations between the first row of nodes of the plate and the nodes of the beam. The degrees of freedom corresponding to the slave nodes are therefore eliminated from the vector of state variables using the following expression:

$$\begin{Bmatrix} \mathbf{p} \\ \dot{\mathbf{p}} \end{Bmatrix} = \begin{bmatrix} \mathbf{T}_{\mathbf{ms}}^{\mathbf{T}} & \mathbf{0} \\ \mathbf{0} & \mathbf{T}_{\mathbf{ms}}^{\mathbf{T}} \end{bmatrix} \begin{Bmatrix} \mathbf{p}^{\mathbf{F}} \\ \dot{\mathbf{p}}^{\mathbf{F}} \end{Bmatrix} \tag{2.79}$$

But transforming the entire state matrix $\mathbf{A}$ in one go using the transformation matrix used in Equation (2.79) does not hold. This can be explained by working out the following relation:

$$\begin{gathered} -\left(\mathbf{T}_{\mathbf{ms}}^{\mathbf{T}} \mathbf{M} \mathbf{T}_{\mathbf{ms}}\right)^{-1} \left(\mathbf{T}_{\mathbf{ms}}^{\mathbf{T}} \mathbf{K} \mathbf{T}_{\mathbf{ms}}\right) \neq \mathbf{T}_{\mathbf{ms}}^{\mathbf{T}} \left(-\mathbf{M}^{-1}\mathbf{K}\right) \mathbf{T}_{\mathbf{ms}} \\ \Updownarrow \\ -\left(\mathbf{T}_{\mathbf{ms}}\right)^{-1} \mathbf{M}^{-1} \left(\mathbf{T}_{\mathbf{ms}}^{\mathbf{T}}\right)^{-1} \mathbf{T}_{\mathbf{ms}}^{\mathbf{T}} \mathbf{K} \mathbf{T}_{\mathbf{ms}} \neq -\mathbf{T}_{\mathbf{ms}}^{\mathbf{T}} \mathbf{M}^{-1} \mathbf{K} \mathbf{T}_{\mathbf{ms}} \end{gathered}$$

Since $\mathbf{T}_{\mathbf{ms}}$ and its transpose are not square matrices, they cannot be inverted, meaning that the above equality does not hold.

2.6. Verification

In this section, the verification of the structural model is explained. The structural beam model has already been verified by Werter (2012), but the static and dynamic plate model and the coupling of the beam and plate elements still need to be verified.

2.6.1. Verification of the static model

As the bending and membrane stiffnesses are uncoupled, they can be verified independently. First the bending model is verified, followed by the membrane model.

Bending element

The bending element is verified by comparing its performance with Abaqus, in which general-purpose conventional shell elements with 4 nodes (S4) are used. These elements allow transverse shear deformation and use thick shell theory as the shell thickness increases and become discrete Kirchhoff thin shell elements as the thickness decreases Dassault Systèmes (2014). Note that the number of elements is limited to 1000 in the student edition of Abaqus, which is used for the verification. The following aspects of the model have to be verified:

1. Finite element theory: do the results match for a straightforward geometry and isotropic material?
2. Geometry: whether or not arbitrary plate shapes are modelled accurately. A rectangular and skewed plate are used, as depicted in Figures 2.16 and 2.17.

3. Material: is the composite material modelled correctly? Unidirectional and quasi-isotropic CFRP layups are included in the investigation. The definition of the fibre orientation is shown in Figure 2.18.

The geometry and dimensions of the rectangular and skewed plate are depicted in Figures 2.16 and 2.17. The material for which the plate model is verified is aluminium and CFRP, the properties of which can be found in Table 2.8. The unidirectional (UD) and quasi-isotropic (QI) layups are defined as follows: $[0_8]$ and $[0_2/-45_2/45_2/90_2]_s$. The main fibre directions for the rectangular and skewed plate are depicted in Figure 2.18.

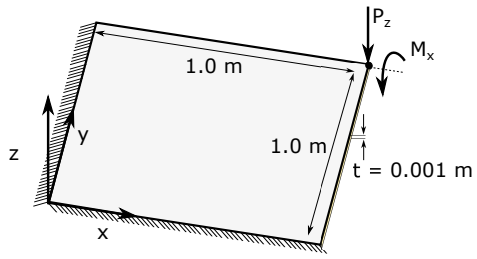

Figure 2.16: Geometry of the rectangular plate used to verify structural model

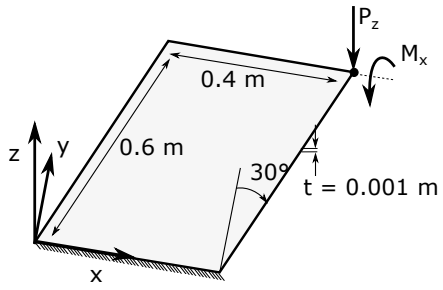

Figure 2.17: Geometry of the skewed plate used to verify structural model

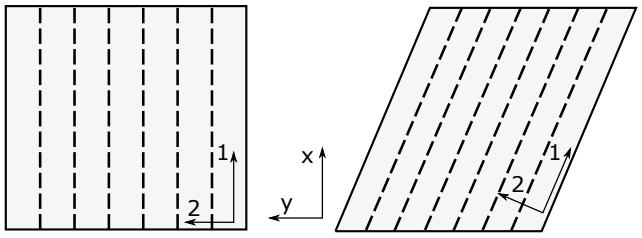

Figure 2.18: Definition of the fibre orientation of the CRFP material in the rectangular and skewed plate: main fibre direction is along the dashed lines.

Aluminium	
E	70 GPa
ν	0.33 -
ρ	2750 kg/m^3
CFRP	
E_1	127.55 GPa
E_2	13.031 GPa
ν_{12}	0.3 —
G_{12}	6.4121 GPa
t_{ply}	0.00127 m
ρ	1611 kg/m^3

Table 2.1: Material properties

First, a rectangular plate of 1.0 m by 1.0 m, clamped at the edges $x = 0$ and $y = 0$ as depicted in Figure 2.16, is subjected to the following 3 static load cases: (1) out-of-plane load acting in the corner node, (2) a moment around the X-axis acting in the corner node and (3) a distributed out-of-plane load. The distributed load is created by applying concentrated load of 0.001 $[N]$ at all of the free nodes.

Table 2.2: Results from static analysis of a rectangular plate, the error is computed using $\frac{U_{matlab}-U_{abaqus}}{U_{matlab}} \cdot 100\%$

Load case	**Out-of-plane disp. [m]**			**Rot. around the x-axis [rad]**		
	Matlab	Abaqus	Error [%]	Matlab	Abaqus	Error [%]
Point load $P_z = 1[N]$						
Aluminium	0.0459	0.0459	-0.0813	0.0667	0.0668	-0.1907
CFRP UD 0^o	0.0879	0.0880	-0.0475	0.1815	0.1826	-0.6119
CFRP QI	0.00704	0.00705	-0.1195	0.00992	0.00997	-0.4677
Point moment $M_x = 1[Nm]$						
Aluminium	0.0667	0.0668	-0.1907	0.4498	0.4896	**-8.842**
CFRP UD 0^o	0.1815	0.1826	-0.6119	1.8631	2.0180	**-8.317**
CFRP QI	0.00992	0.00997	-0.4677	0.0947	0.1074	**-13.388**
Distributed load $q = 0.001[N]$						
Aluminium	0.0667	0.0668	-0.0551	0.0636	0.0635	0.2349
CFRP UD 0^o	0.1046	0.1046	0.0055	0.0709	0.0704	0.6797
CFRP QI	0.0104	0.0104	-0.0591	0.00658	0.00655	0.4807

The displacements and rotations in the corner node computed with the present finite element code match the results from Abaqus well. Only the results for θ_x rotations due to a moment M_x diverge, as can be seen in Table 2.2 (values in red). The rotation θ_x increases rapidly when approaching the corner node. To determine whether the present model differs from Abaqus only locally, θ_x from Matlab and Abaqus along the right edge of the plate (as shown in Figure 2.16) are plotted and depicted in Figure 2.19. It can be seen that only at the two outer nodes the rotations deviates and that it is indeed only a local error.

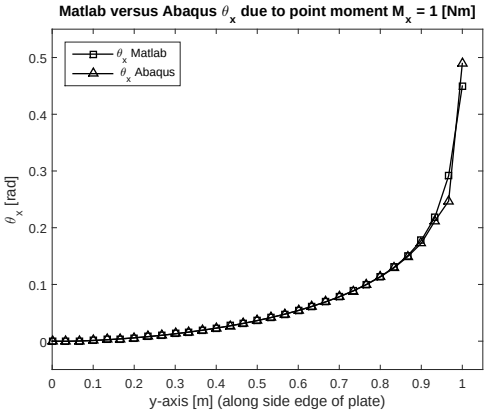

Figure 2.19: Rotation around the x-axis along the right edge due to a moment in the corner node.

A skewed plate of 0.4 m by 0.6 m, clamped at the edge $y = 0$ as depicted in Figure 2.17, is subjected to the following 3 static load cases: (1) out-of-plane load acting in the corner node, (2) a moment around the X-axis acting in the corner node and (3) a distributed out-of-plane load. The distributed load is created by applying concentrated load of 0.001 $[N]$ at all of the free nodes.

Table 2.3: Results from static analysis of a skewed plate, the error is computed using $\frac{U_{matlab}-U_{abaqus}}{U_{matlab}} \cdot 100\%$

Load case	**Out-of-plane disp. [m]**			**Rot. around the x-axis [rad]**		
	Matlab	Abaqus	Error [%]	Matlab	Abaqus	Error [%]
Point load $P_z = 1[N]$						
Aluminium	0.0726	0.0727	-0.126	0.1207	0.1207	-0.034
CFRP UD 0^o	0.0598	0.0599	-0.072	0.1960	0.1966	-0.326
CFRP QI	0.0078	0.0078	-0.149	0.0121	0.0121	-0.010
Point moment $M_x = 1[Nm]$						
Aluminium	0.1595	0.1597	-0.1002	0.7739	0.8184	**-5.748**
CFRP UD 0^o	0.1312	0.1314	-0.1763	0.4510	0.4532	-0.488
CFRP QI	0.0169	0.01670	-0.2008	0.0891	0.0965	**-8.347**
Distributed load $q = 0.001[N]$						
Aluminium	0.0174	0.0175	-0.475	0.0289	0.0287	0.538
CFRP UD 0^o	0.0105	0.0106	-0.661	0.0191	0.0191	0.142
CFRP QI	0.0019	0.0019	-0.6319	0.0034	0.0033	0.285

Again, the results of matlab are very similar to those obtained with the finite element analysis in Abaqus. The same discrepancy in the rotation due to a point moment is observed.

Verification of membrane element

To verify the membrane part of the shell element, two standard verification cases are used. The first one is called the cantilevered plate problem, depicted in Figure 2.20, and the second, called Cook's problem is shown in Figure 2.21. The arbitrary shape of the elements in both verification cases tests whether the isoparametric representation of the elements functions properly. The membrane element is based on the theory of Cook (1986). In this paper, results for the cantilevered plate problem are given as well, and can be compared to the present model.
In Table 2.4 and 2.5, the results of both cases are presented. It can be seen that the results match well with the references. The only discrepancy is the displacement in the cantilevered plate case for distorted mesh, which does not match with the results from Cook (1986). It is however, better in comparison with the other references.

Table 2.4: Tip displacement [-] for the cantilevered plate problem, comparing the present model to several references.

Mesh	4×1 (regular)	Error [%]	4×1 (distorted)	Error [%]
Present model	0.3283	–	0.2969	–
Cook (1986)	0.3283	0	0.3379	13.81
MacNeal and Harder (1988)	0.3409	3.84	0.2978	0.30
Ibrahimbegovic (1990)	0.3445	4.93	0.3066	3.27
Iura and Atluri (1992)	0.3432	4.54	0.3410	14.85

Table 2.5: Tip displacement [-] for Cook's problem, comparing the present model to several references.

Mesh	8×8 (regular)	Error [%]
Present model	22.370	–
Ibrahimbegovic (1990)	23.668	5.80
Iura and Atluri (1992)	23.998	7.28

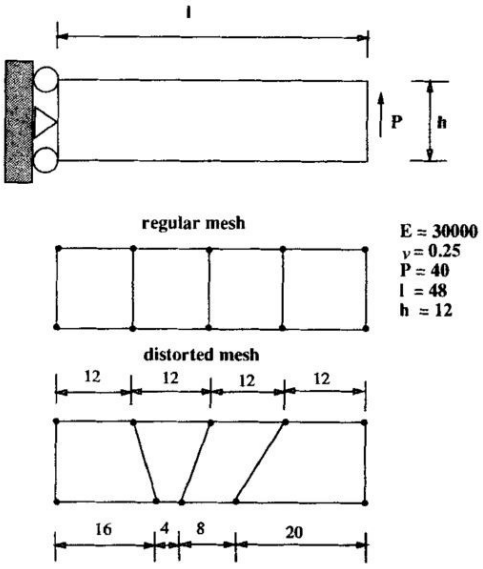

Figure 2.20: Geometry and material properties of the cantilevered plate used for verification

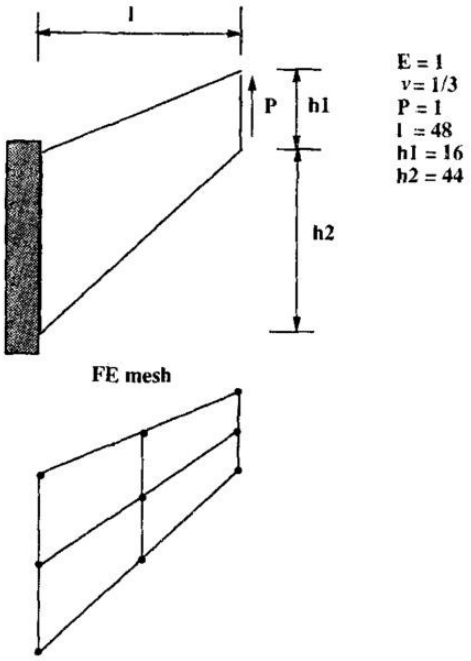

Figure 2.21: Geometry and material properties of the Cook's problem

To verify that the material properties are modelled correctly for the membrane element, an in-plane edge load as drawn in Figure 2.22 is applied to the rectangular plate discussed in the previous section. Again, Abaqus is used for comparison and S4 elements are used. For the three materials (aluminium, CFRP UD 0^o and CFRP QI), the magnitude of the displacement along the diagonal of the rectangular plate is plotted. In Figure 2.23, the results are shown for the UD laminate, and except for the corner node, the results from the present study and Abaqus match perfectly, therefore verifying the material implementation for the membrane element.

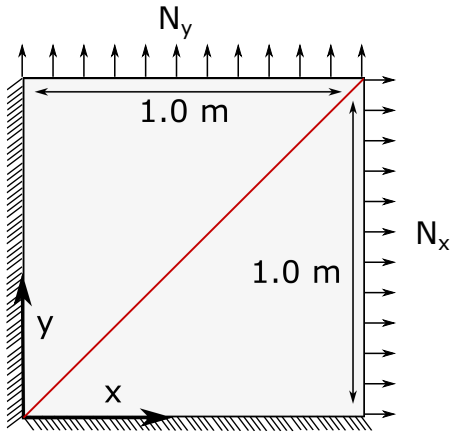

Figure 2.22: Geometry of the rectangular plate used to verify structural model

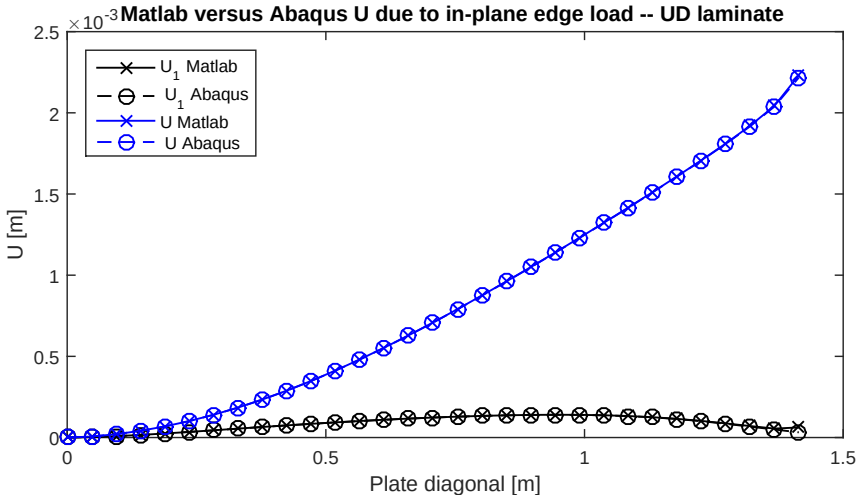

Figure 2.23: Comparison of magnitude and x-component of displacement along the diagonal of the rectangular plate (depicted in red in Figure 2.22) of Matlab and Abaqus. A UD 0^o laminate is used as material.

2.6.2. Verification of the dynamic model

To verify the dynamic model, the eigenfrequencies and eigenmodes of the finite element model of the plate structure are computed and compared with abaqus. In the absence of external loads, the equation of motion is given by:

$$\mathbf{M}\ddot{\mathbf{p}} + \mathbf{K}\mathbf{p} = \mathbf{0} \tag{2.80}$$

The eigenvalues are determined using the equation below. Solving this equation for λ results in the eigenvalues and eigenmodes of the equation of motion.

$$\left(-\lambda^2\mathbf{M} + \mathbf{K}\right)\hat{\mathbf{p}} = \mathbf{0} \tag{2.81}$$

The results from the eigenvalue analysis are given in Table 2.6. It can be seen that the eigenfrequencies computed by Matlab and Abaqus match very well. Only for some of the higher modes, larger discrepancies are found. The same geometries as in the static verification are used. Note that during the eigenvalue analysis both bending and membrane modes are included, but the 5 most critical modes all correspond to a bending mode.

Table 2.6: Eigenvalue analysis of a rectangular plate

Mode number	Eigenfrequency [rad/s]		
	Matlab	Abaqus	Error [%]
Aluminium			
1	1.683	1.683	0.003
2	5.805	5.814	-0.147
3	6.521	6.534	-0.194
4	11.633	11.635	-0.021
5	15.331	15.413	-0.537
CFRP UD 0^o			
1	1.727	1.727	-0.030
2	3.894	3.900	-0.143
3	8.917	8.961	-0.493
4	9.415	9.440	-0.264
5	11.258	11.281	-0.208
CFRP QI			
1	3.852	3.852	0.002
2	10.961	10.974	-0.119
3	16.984	17.018	-0.198
4	24.047	24.100	-0.221
5	27.542	27.620	-0.283

Table 2.7: Eigenvalue analysis of a skewed plate

Mode number	Eigenfrequency [rad/s]		
	Matlab	Abaqus	Error [%]
Aluminium			
1	1.915	1.914	0.027
2	7.164	7.160	0.046
3	12.727	12.723	0.031
4	21.465	21.476	-0.053
5	35.884	35.968	-0.236
CFRP UD 0^o			
1	3.126	3.127	-0.021
2	6.185	6.184	0.001
3	19.656	19.684	-0.142
4	21.543	21.583	-0.187
5	30.221	30.283	-0.204
CFRP UD QI			
1	5.276	5.275	0.015
2	16.115	16.093	0.136
3	33.676	33.698	-0.064
4	52.465	52.439	0.050
5	77.459	77.630	-0.221

2.6.3. Verification of the coupled structure

To verify that the master-slave coupling of the beam and plate degrees of freedom is implemented correctly, the eigenvalues and eigenmodes of a coupled structure are computed and compared with values from Abaqus. The geometry of the beam and plate is shown in Figure 2.25. The beam is discretised using 20 elements and the plate is discretised using 20 elements in length direction and 10 in width direction. The cross-sectional properties of the beam are given in Table 2.8 and the material properties of the aluminium alloy used are stated in Table 4.2.

In Abaqus, the rigid links are modelled using multi point constraints (MPC). The beam nodes are chosen to be the control points and the nodes at the first row of plate elements are therefore the slave nodes. From the different options for MPC types, the beam option is chosen.

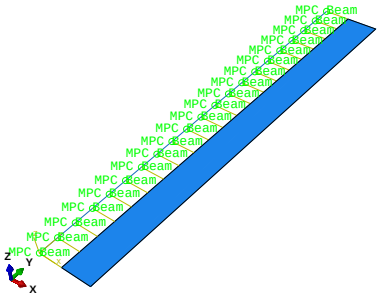

Figure 2.24: The beam and plate model in Abaqus, showing the MPC constraints

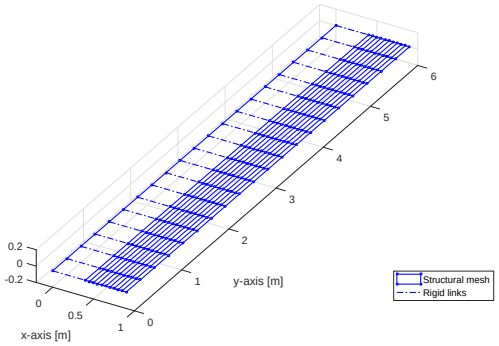

Figure 2.25: Mesh of the beam and plate model in Matlab

Table 2.8: Material properties

Beam cross-sectional properties	
A	$1 \cdot 10^{-3} m^2$
I_{22}	$2 \cdot 10^{-5} m^4$
I_{23}	$5 \cdot 10^{-5} m^4$
I_{33}	$25 \cdot 10^{-5} m^4$
I_p	$27 \cdot 10^{-5} m^4$
J	$4 \cdot 10^{-4} m^4$
k	$5/6$
e_y	$0.1m$
e_z	$0.2m$
Plate properties	
t	$0.005m$
Material properties	
E	$70GPa$
G	$26.9GPa$
ν	0.33

Table 2.9: Eigenfrequencies of the coupled structure compared with results from Abaqus

	Present model	Abaqus	Error [%]
1.	$5.41\ Hz$	$5.20\ Hz$	3.88
2.	$16.62\ Hz$	$16.52\ Hz$	0.60
3.	$18.63\ Hz$	$18.76\ Hz$	0.70
4.	$20.75\ Hz$	$20.81\ Hz$	0.29
5.	$23.01\ Hz$	$23.12\ Hz$	0.48

The comparison of the eigenfrequencies shows good agreement between the present model and Abaqus. Only the natural frequency of the first mode deviates slightly. The eigenmodes in the present model and Abaqus are the same. Therefore it can be said that the structural coupling using the master-slave method is verified.

3
Aerodynamic model

The aerodynamic model used in the aeroelastic analysis, is a steady and unsteady vortex-lattice model based on potential flow theory, developed by Werter and De Breuker (2015). This paper gives a detailed explanation of the model. In Section 3.1, a brief summary of this model is given, to understand its capabilities and limitations, and to be able to explain in Section 3.2 which modifications are made to the aerodynamic model to make it compatible with the flexible trailing edge structure.

3.1. Existing steady and unsteady vortex-lattice method

The steady and unsteady aerodynamic model which are incorporated in the PROTEUS model, are vortex-lattice models (VLM). The vortex-lattice method is based on potential flow theory, which is an efficient way of describing the real flow and holds under the assumption that the flow is irrotational, inviscid and incompressible (however, compressibility is accounted for by the Prandtl-Glauert correction).

The governing equation in potential flow is the Laplace equation, which is derived from the continuity equation, under the assumption of incompressible and irrotational flow:

$$\nabla^2 \phi = 0 \tag{3.1}$$

In which ϕ is the velocity potential. The vortex-lattice method is a way to find a solution to the velocity potential, by discretising the flow over the wing by a series of vortex rings, which satisfy the Laplace equation. After the velocity potential is determined over the wing, the pressure distribution can be determined and hence the aerodynamic forces. Several boundary conditions have to be satisfied by the vortex-lattice method, starting with the far field condition, which states that disturbances of the flow due to the vortex panels have to vanish at infinity:

$$\lim_{|\mathbf{x}-\mathbf{x}_0 \to \infty|} \nabla \phi = 0, \qquad \text{Far field condition} \tag{3.2}$$

In which $|\mathbf{x} - \mathbf{x}_0|$ is the distance from the wing to a point far away from the wing. Next is the flow tangency condition, which ensures that no flow can go through the body of the wing:

$$\mathbf{A}\boldsymbol{\Gamma}^t = -\boldsymbol{V}_\infty \cdot \boldsymbol{n}, \qquad \text{Flow tangency condition} \tag{3.3}$$

In which $\mathbf{A}$ are the aerodynamic influence coefficients, $\boldsymbol{\Gamma}^t$ is the vectors of vortex strengths at time t, $\boldsymbol{V}_\infty$ is the free-stream velocity and $\boldsymbol{n}$ is the vector with surface normals of the vortex panels.
In the absence of viscosity, there is no mechanism which fixes the stagnation point to the trailing edge of the airfoil, leading to infinite velocities around the sharp corner of the trailing edge . Therefore, the Kutta condition is required to enforce the stagnation point at the trailing edge:

$$\boldsymbol{\Gamma}^t_{TE} = \boldsymbol{\Gamma}^t_{w0}, \qquad \text{Kutta condition} \tag{3.4}$$

In which $\mathbf{\Gamma}^t_{TE}$ are the vortex strength of the panels at the trailing edge of the wing surface and $\mathbf{\Gamma}^t_{w0}$ are the vortex strengths at the start of the wake. Finally, for the unsteady aerodynamic model, the Helmholtz theorem defines how vorticity is trasported through the wake after it has been shed by the airfoil.

$$\mathbf{H}_1\mathbf{\Gamma}^t = \mathbf{H}_2\mathbf{\Gamma}^{t-1}, \qquad \text{Helmholtz theorem} \tag{3.5}$$

The wing is discretised in an aerodynamic mesh, with a cosine distribution in the span-wise direction to have an increased mesh density at the wing tip, where the pressure gradients are highest. In chord-wise direction, an equally spaced mesh distribution is applied. In both the steady and unsteady models, the wake is shed in the direction of the free-stream velocity, which can be done under the assumption of small perturbations.

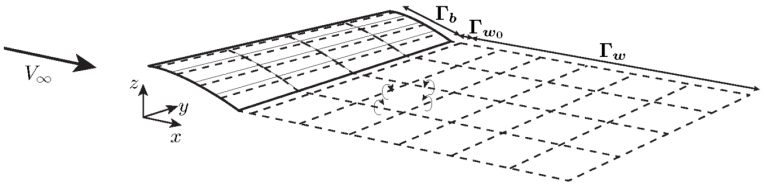

Figure 3.1: Schematic representation of the aerodynamic mesh. The thick solid lines indicate the wing geometry, the thin solid lines the aerodynamic panels and the dashed lines the vortex-ring elements. Image courtesy of Werter and De Breuker (2015).

In Figure 3.1, the wing discretisation is shown for the unsteady aerodynamic model. In the steady model, the wake can be discretised with one element in chord-wise direction, since the vortex strength in the wake is constant.

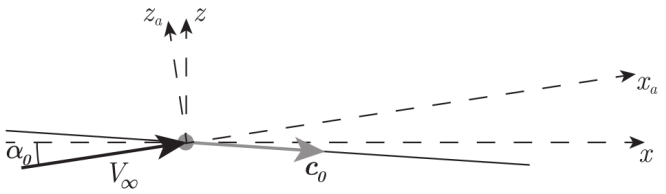

Figure 3.2: Schematic representation of the aerodynamic coordinate system xyz_a, in comparison to the body fixed coordinate system of the wing used by the structural model. Image courtesy of Werter (2012).

The aerodynamic mesh is defined in the aerodynamic coordinate system, shown in Figure 3.2. This coordinate system is defined such that the x-axis is in line with the free stream flow velocity V_∞. This means that the aerodynamic mesh constructed based on the wing geometry has to be transformed to the aerodynamic coordinate system, and the aerodynamic forces computed by the aerodynamic model have to be rotated to the body-fixed reference system before transfered to the structural mesh.

3.1.1. Steady VLM

The steady vortex-lattice method determines the steady aerodynamic forces based on the wing's geometry. In the aeroelastic model, it is closely coupled with the structural model. To achieve this, an aerodynamic stiffness matrix is computed which directly relates structural deformations to aerodynamic forces, which is defined as:

$$\mathbf{K}_a\mathbf{p} = \Delta\mathbf{F}_a \tag{3.6}$$

In which the subscript a refers to any forces, displacements and stiffnesses matrices of the aerodynamic model. Taking the derivative with respect to the structural degrees of freedom yields:

$$\mathbf{K}_a = \frac{d\mathbf{F}_a}{d\mathbf{p}} \tag{3.7}$$

Hence, computing the aerodynamic stiffness matrix is a matter of determining all the derivatives of the aerodynamic force vector $\mathbf{F}_a$ with respect to the structural degrees of freedom. Using the chain rule, the derivative of the forces with respect to the structural degrees of freedom can be written in function of the aerodynamic mesh:

$$\mathbf{K}_a = \frac{d\mathbf{F}_a}{d\mathbf{x}_a} \cdot \frac{d\mathbf{x}_a}{d\mathbf{x}_s} \cdot \frac{d\mathbf{x}_s}{d\mathbf{p}} + \frac{d\mathbf{F}_a}{d\mathbf{x}_a} \cdot \frac{d\mathbf{x}_a}{d\boldsymbol{\theta}_s} \cdot \frac{d\boldsymbol{\theta}_s}{d\mathbf{p}} \tag{3.8}$$

In which $\mathbf{p}$ are the structural degrees of freedom, $\mathbf{x}_s$ contain the coordinates of the structural beam mesh, $\boldsymbol{\theta}_s$ contain the structural rotations and $\mathbf{x}_a$ contains the coordinates of the aerodynamic mesh. The derivatives of the aerodynamic force will be called sensitivities, and have to be derived for the flexible trailing edge as well. This will be discussed in Section 3.2.2.

3.1.2. Unsteady VLM

In the paper of Werter et al. (2015), an explanation for the unsteady aerodynamic model is given, which results in the following expressions for the aerodynamic input and output equations of the aerodynamic state-space system:

$$\begin{Bmatrix} \dot{\boldsymbol{\Gamma}}_W \\ \dot{\boldsymbol{\alpha}} \end{Bmatrix} = \begin{bmatrix} \mathbf{K_1} & \mathbf{K_2} \\ \mathbf{0} & \mathbf{0} \end{bmatrix} \begin{Bmatrix} \boldsymbol{\Gamma_W} \\ \boldsymbol{\alpha} \end{Bmatrix} + \begin{bmatrix} \mathbf{0} \\ \mathbf{I} \end{bmatrix} \dot{\boldsymbol{\alpha}} \tag{3.9}$$

$$\mathbf{F}_a = \begin{bmatrix} \mathbf{L_1} & \mathbf{L_2} \end{bmatrix} \begin{Bmatrix} \boldsymbol{\Gamma}_W \\ \boldsymbol{\alpha} \end{Bmatrix} + \mathbf{L_3}\dot{\boldsymbol{\alpha}} \tag{3.10}$$

In the above equations, $\boldsymbol{\Gamma_W}$ is the vector containing the vortex strengths of the wake panels, and $\mathbf{K}_1$ and $\mathbf{K}_2$ originate from the flow tangency equation, Kutta condition and Helmholtz theorem. $\mathbf{L}_1$ and $\mathbf{L}_2$ are computed using, besides the three mentioned equations, the steady and unsteady components of the Kutta-Joukowski theorem. $\boldsymbol{\alpha}$ is the perturbation angle of attack of each of the aerodynamic panels. This angle depends on the angle of the panel with respect to the perturbed free-stream flow and on the pitch and plunge motion of the panel.

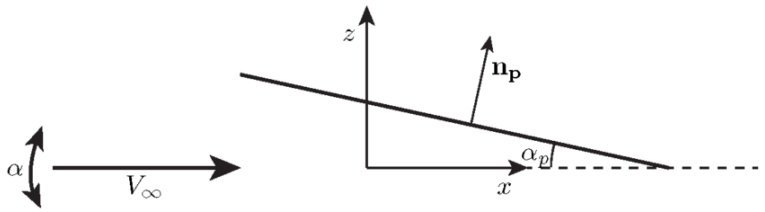

Figure 3.3: The definition of the panel angle of attack α_p, which is the angle of attack of a panel with respect to the undisturbed flow.

Note that the perturbation angle of attack α is different from the panel angle of attack α_p with respect to the undisturbed flow. In Figure 3.3, the difference is depicted. The perturbation angle of attack is a disturbance with respect to the undisturbed flow and assuming this disturbance is small, a small angle

approximation can be made. This allows to write the boundary conditions of the flow tangency condition as follows:

$$-\boldsymbol{V}_\infty \cdot \boldsymbol{n_p} = -V_\infty \begin{pmatrix} 1 \\ \alpha \end{pmatrix} \cdot \begin{pmatrix} \sin\alpha_p \\ \cos\alpha_p \end{pmatrix} = -V_\infty \sin\alpha_p - V_\infty \cos\alpha_p \cdot \alpha \tag{3.11}$$

The above assumption allows the unsteady aerodynamic system to be written in continuous-time state-space form, which results in Equations (4.27) and (4.28).

3.2. Modifications to accommodate deformations in stream-wise direction

The aerodynamic model in the original PROTEUS model can in principle represent any wing deformation, but is programmed to accommodate a chord-wise rigid deformation based on the structural beam deflection and twist.

The chord-wise deformation of the aerodynamic mesh of the trailing edge is accomplished in the steady aerodynamic model by determining the sensitivities of the aerodynamic forces with respect to the structural degrees of freedom of the trailing edge, and in the unsteady model by defining the perturbation angle of attack α of the trailing edge aerodynamic panels in function of the trailing edge structural degrees of freedom.

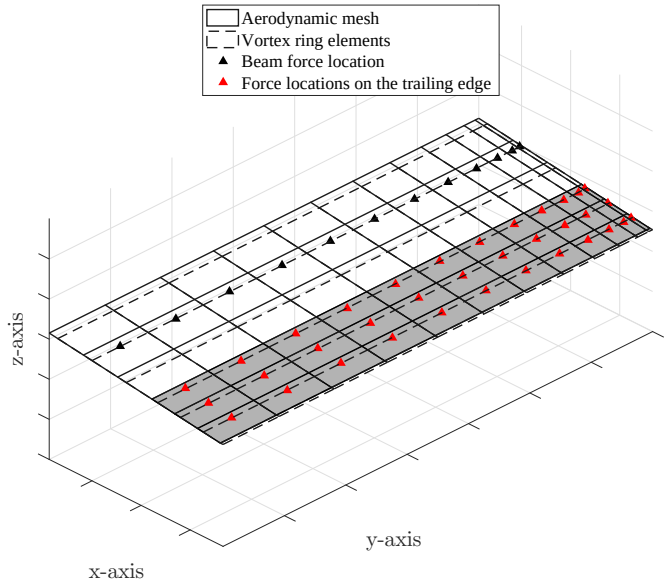

Figure 3.4: Aerodynamic wing discretisation, showing the distinction between the rigid chord-wise and trailing edge region and the different chord-wise mesh densities.

The first step is to modify the aerodynamic mesh, to make sure its edges match the trailing edge region exactly. This is done for 2 reasons:

1. For a short trailing edge, it might be required to have a finer mesh than the rest of the wing to capture the bigger variation in pressure that accompanies a flexible trailing edge. This is needed to determine how the complete airfoil's pressure distribution is affected and to determine plate flutter of the trailing edge.
2. To facilitate the interpolation of displacements and forces between the trailing edges structural and aerodynamic mesh, the outer edges of both meshes coincide. As a result, the beam structure and corresponding aerodynamic mesh at one hand, and the trailing edge structure and corresponding trailing edge aerodynamic mesh on the other hand, can be treated separately in the interpolation of forces and displacements.

3.2.1. Force extraction

In the PROTEUS code, the forces on each chord-wise rigid segment are added to a resultant aerodynamic force and moment at the position of the structural beam, using a rigid link. For the aerodynamic trailing edge mesh, the individual forces at each of the panels are extracted, such that they can be interpolated to the trailing edge structure. This results in a vector of forces $\mathbf{F}_{a,p}$ in the aerodynamic coordinate system, from the force locations shown in Figure 3.4. The force vector does not contain moments, hence the force vector passed on to the structural model will have the following shape:

$$\mathbf{F}_{a,p} = \begin{bmatrix} F_{x,1} & 0 & F_{z,1} & 0 & 0 & 0 & F_{x,2} & \dots & 0 \end{bmatrix}' \tag{3.12}$$

In comparison with the aerodynamic force vector of the beam:

$$\mathbf{F}_{a,b} = \begin{bmatrix} F_{x,1} & 0 & F_{z,1} & 0 & M_{y,1} & 0 & F_{x,2} & \dots & 0 \end{bmatrix}' \tag{3.13}$$

And the total aerodynamic force vector, containing both resultant forces on the beam and individual forces at the trailing edge looks like:

$$\mathbf{F}_a = \begin{Bmatrix} \mathbf{F}_{a,b} \\ \mathbf{F}_{a,p} \end{Bmatrix} \tag{3.14}$$

3.2.2. Sensitivities with respect to plate degrees of freedom

The sensitivities with respect to the trailing edge structural degrees of freedom have to be derived in order to obtain a closely coupled aeroelastic system which includes the trailing edge degrees of freedom. To determine these sensitivities, the wing deformation is split in a purely chord-wise rigid deformation and a flat wing of which only the trailing edge deforms. Since potential flow theory is used, superposition of the vortex strength contribution of both wing shapes can be used. In Figure 3.5, this division of rigid and flexible airfoil deformation is shown schematically.
The reason for splitting it in this way is that two independent aerodynamic stiffness matrices can be computed, leaving the original PROTEUS aerodynamic stiffness matrix unchanged. A variation of Equation (3.8) can be written for the trailing edge degrees of freedom:

$$\mathbf{K}^{\star}_{a,p} = \frac{d\mathbf{F}_a}{d\mathbf{x}_a} \cdot \frac{d\mathbf{x}_a}{d\mathbf{x}_s} \cdot \frac{d\mathbf{x}_s}{d\mathbf{p}_{p,flex}} \tag{3.15}$$

It can be seen that the aerodynamic mesh is not dependent on the rotational degrees of freedom of the trailing edge structure, since it can be defined completely by the displacements of the trailing edge only. The aerodynamic stiffness matrix of the wing with flexible trailing edge can then be written as:

$$\mathbf{K}^{\star}_{a} = \begin{bmatrix} \mathbf{K}_{a,b} & \mathbf{K}^{\star}_{a,p} \end{bmatrix} \tag{3.16}$$

Such that the change in aerodynamic force due to the structural deformation can be calculated using the following equation:

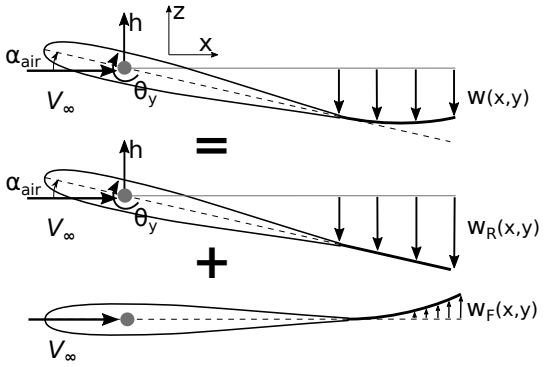

Figure 3.5: Schematic of the superposition of a chord-wise rigid wing and a wing with flexible trailing edge to obtain the actual wing deformation.

$$\Delta \mathbf{F}_a = \mathbf{K}_a^\star \begin{Bmatrix} \Delta \mathbf{p}_b \\ \Delta \mathbf{p}_{p,flex} \end{Bmatrix} \tag{3.17}$$

Note that in the equations above, the flexible deformation without the rigid rotation due to the beam rotation is meant, as depicted in Figure 3.5. In the following section, it is explained how the aerodynamic stiffness matrix is transformed such that the normal degrees of freedom $\mathbf{p}$ can be used.

Transformation matrix $\mathbf{T_{flex}}$

In the static aeroelastic system, the structural degrees of freedom consist of the beam and plate nodal degrees of freedom. Since, the aerodynamic stiffness matrix is split up as shown in Figure 3.5, the deformation of the trailing edge without the rigid body rotation is required, given by $\mathbf{p}_{p,flex}$. These can be obtained by subtracting the displacement due to the rigid rotation:

$$\mathbf{p}_{p,flex} = \mathbf{p}_p - \mathbf{p}_{p,rig} \tag{3.18}$$

To determine the trailing edge's chord-wise rigid deformation due to the beam deflection and rotation, a similar transformation matrix such as presented in Section 2.4, to couple the beam and plate structures, is used. Only now, all trailing edge nodes are involved unlike only the first row of nodes with the beam-plate coupling. For a trailing edge node along a certain chord-wise path, the following equation holds:

$$\begin{Bmatrix} u_{p,i} \\ v_{p,i} \\ w_{p,i} \\ \theta_{x,p,i} \\ \theta_{y,p,i} \\ \theta_{z,p,i} \end{Bmatrix} = \underbrace{\begin{bmatrix} 1 & 0 & 0 & 0 & -\Delta z_i & 0 \\ 0 & 1 & 0 & 0 & 0 & \Delta x_i \\ 0 & 0 & 1 & 0 & -\Delta x_i & 0 \\ 0 & 0 & 0 & 1 & 0 & 0 \\ 0 & 0 & 0 & 0 & 1 & 0 \\ 0 & 0 & 0 & 0 & 0 & 1 \end{bmatrix}}_{\mathbf{T}_{\mathbf{rig}}^*} \begin{Bmatrix} u_b \\ v_b \\ w_b \\ \theta_{x,b} \\ \theta_{y,b} \\ \theta_{z,b} \end{Bmatrix} \tag{3.19}$$

With this transformation matrix, the chord-wise rigid trailing edge deformation is determined:

$$\mathbf{p}_{p,rig} = \mathbf{T}_{rig} \cdot \mathbf{p}_b \tag{3.20}$$

Subtraction of the chord-wise rigid deformation from the total deformation then yields:

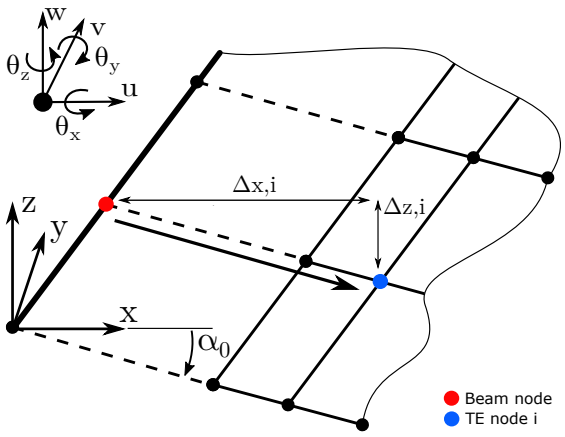

Figure 3.6: Schematic representation of the relation between a beam and a certain trailing edge node i.

$$\mathbf{p}_{p,flex} = \left(\mathbf{I^\star}_p - \mathbf{T}_{rig} \cdot \mathbf{I^\star}_b\right) \begin{Bmatrix} \mathbf{p}_b \\ \mathbf{p}_p \end{Bmatrix} \tag{3.21}$$

In which $\mathbf{I^\star}_p$ and $\mathbf{I^\star}_b$ contain identity matrices with number of rows and columns corresponding to the length of the trailing edge and beam degrees of freedom respectively, to select beam or trailing edge degrees of freedom:

$$\mathbf{I^\star}_p = \begin{bmatrix} \mathbf{0} & \mathbf{I}_p \end{bmatrix} \tag{3.22}$$

$$\mathbf{I^\star}_b = \begin{bmatrix} \mathbf{I}_b & \mathbf{0} \end{bmatrix} \tag{3.23}$$

Finally, a transformation matrix can be defined which relates the complete set of structural degrees of freedom to a new set of degrees of freedom in which the trailing edge degrees of freedom only reflect the deformation due to plate deflection.

$$\begin{Bmatrix} \mathbf{p}_b \\ \mathbf{p}_{p,flex} \end{Bmatrix} = \underbrace{\begin{bmatrix} \mathbf{I^\star}_b \\ \mathbf{I^\star}_p - \mathbf{T}_{rig} \cdot \mathbf{I^\star}_b \end{bmatrix}}_{\mathbf{T_{flex}}} \begin{Bmatrix} \mathbf{p}_b \\ \mathbf{p}_p \end{Bmatrix} \tag{3.24}$$

Now that the transformation matrix is defined, the aerodynamic stiffness matrix can be transformed, such that it matches the actual degrees of freedom of the wing structure:

$$\mathbf{K}_a = \mathbf{T}'_{flex} \mathbf{K}^\star_a \mathbf{T}_{flex} \tag{3.25}$$

Derivative of aerodynamic mesh with respect to the trailing edge structure

The derivative $\frac{d\mathbf{x}_a}{d\mathbf{p}_p}$, is found by first interpolating the structural trailing edge displacements to the aerodynamic mesh of the trailing edge:

$$\mathbf{x}_{a,p} = \mathbf{T}_{sa} \mathbf{x}_{s,p} \tag{3.26}$$

The derivation of the interpolation matrix $\mathbf{T}_{sa}$ will be explained in Section 4.1. Since the displacements of the trailing edge structure are a function of the trailing edge's degrees of freedom the following equality holds:

$$\frac{d\mathbf{x}_{a,p}}{d\mathbf{p}_p} = \frac{d\left(\mathbf{T}_{sa}\mathbf{x}_{s,p}\right)}{d\mathbf{p}_p} = \frac{d\left(\mathbf{T}_{sa}\mathbf{x}_{s,p}\right)}{d\mathbf{x}_{s,p}} \cdot \frac{d\mathbf{x}_{s,p}}{d\mathbf{p}_p} = \mathbf{T}_{sa} \cdot \frac{d\mathbf{x}_{s,p}}{d\mathbf{p}_p} \tag{3.27}$$

Note that $\frac{d\mathbf{x}_{s,p}}{d\mathbf{p}_p}$ is simply a matrix with ones and zeros since the structural mesh deforms exactly as the structural degrees of freedom prescribe, only the rotational degrees of freedom are excluded:

$$\frac{d\mathbf{x}_{s,p}}{d\mathbf{p}_p} = \begin{bmatrix} 1 & 0 & 0 & 0 & 0 & 0 & 0 & 0 & \dots & 0 & 0 & 0 & 0 \\ 0 & 1 & 0 & 0 & 0 & 0 & 0 & 0 & \dots & 0 & 0 & 0 & 0 \\ 0 & 0 & 1 & 0 & 0 & 0 & 0 & 0 & \dots & 0 & 0 & 0 & 0 \\ 0 & 0 & 0 & 0 & 0 & 0 & 1 & 0 & \dots & 0 & 0 & 0 & 0 \\ 0 & 0 & 0 & 0 & 0 & 0 & 0 & 1 & \dots & 0 & 0 & 0 & 0 \\ \vdots & \vdots & \vdots & \vdots & \vdots & \vdots & \vdots & \vdots & \ddots & 0 & 0 & 0 & 0 \\ 0 & 0 & 0 & 0 & 0 & 0 & 0 & 0 & 0 & 1 & 0 & 0 & 0 \end{bmatrix} \tag{3.28}$$

The derivative of the entire wing aerodynamic mesh with respect to the trailing edge structural degrees of freedom is then simply:

$$\frac{d\mathbf{x}_a}{d\mathbf{p}_p} = \begin{bmatrix} \mathbf{0} \\ \mathbf{T}_{sa} \end{bmatrix} \tag{3.29}$$

The part of the aerodynamic mesh not related to the trailing edge structure does not change with a changing trailing edge structural deformation, and is therefore zero.

3.2.3. Aerodynamic state-space system

The modifications to the unsteady aerodynamic state-space system to suit the model with a flexible trailing edge are done to the output equation only. The mesh distribution in the chord-wise direction is modified, but this does not affect the aerodynamic input equation.

In the same way as for the steady aerodynamic model, the forces for the unsteady model from all the individual panels of the trailing edge are extracted. The forces and moments corresponding to the chord-wise rigid segment are still added to the beam resultant forces and moments $\mathbf{F}_a$ and $\mathbf{M}_a$, but for the trailing edge panels, only the aerodynamic forces $\mathbf{F}_a$ are taken into account. Hence the aerodynamic output equation of the state-space system for the model with a flexible trailing edge is slightly different than Equations (4.28), but the aerodynamic input equations remains identical to Equations (4.27):

$$\begin{Bmatrix} \dot{\mathbf{\Gamma}}_W \\ \dot{\boldsymbol{\alpha}} \end{Bmatrix} = \begin{bmatrix} \mathbf{K_1} & \mathbf{K_2} \\ \mathbf{0} & \mathbf{0} \end{bmatrix} \begin{Bmatrix} \mathbf{\Gamma_W} \\ \boldsymbol{\alpha} \end{Bmatrix} + \begin{bmatrix} \mathbf{0} \\ \mathbf{I} \end{bmatrix} \dot{\boldsymbol{\alpha}} \tag{3.30}$$

$$\begin{Bmatrix} \mathbf{F}_{a,b} \\ \mathbf{F}_{a,p} \end{Bmatrix} = \begin{bmatrix} \mathbf{L_{1}}_b & \mathbf{L_{2}}_b \\ \mathbf{L_{1}}_p & \mathbf{L_{2}}_p \end{bmatrix} \begin{Bmatrix} \mathbf{\Gamma}_W \\ \boldsymbol{\alpha} \end{Bmatrix} + \begin{bmatrix} \mathbf{L_{3}}_b \\ \mathbf{L_{3}}_p \end{bmatrix} \dot{\boldsymbol{\alpha}} \tag{3.31}$$

4
Aeroelastic framework

In this chapter, the aeroelastic framework is explained. Firstly, the interpolation method to transfer structural displacements to the aerodynamic mesh and aerodynamic forces to the structural mesh is discussed in Section 4.1. Afterwards, the static aeroelastic equilibrium equation is presented in Section 4.2, followed by the dynamic model, represented with a state-space system in Section 4.3. Finally, the coupled aeroelastic system is verified and these results are shown in Section 4.4.

4.1. Interpolation of forces and displacements

The aerodynamic model determines the aerodynamic forces at the load locations under given flight conditions. To calculate the response of the structure, these loads have to be transferred from the aerodynamic load locations to the nodes of the structure mesh (in Figure 4.1, the position of these nodes is shown). The nodal displacements computed by the structural model then have to be transferred back to determine the new shape of the aerodynamic mesh. Interpolation methods are needed, since the structural and aerodynamic meshes do not coincide. Different requirement for both models result in a difference in the spatial discretisation of both models. The aerodynamic mesh is discretised with a cosine distribution such that larger pressure gradients at the wing tip are captured while keeping the rest of the mesh coarser. For the structural model on the other hand, with a distributed load on both the beam and the shell elements, there is no need for a variable mesh size.

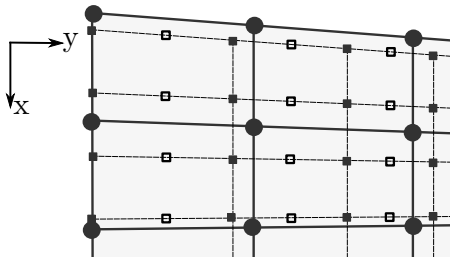

Figure 4.1: Schematic representation of the structure and aerodynamic mesh. The solid circles show the structural nodes, the solid squares the corners of the vortex ring elements and the open squares the aerodynamic force locations.

There is a large range of interpolation methods available. In the work of De Boer et al. (2007), nearest neighbour interpolation, weighted residual methods and radial basis function interpolation are discussed. In the given reference, the radial basis function (RBF) with a compact support radius was favoured. Based on their findings, it is decided to use RBF interpolation for the displacement interpolation as discussed in Section 4.1.1. RBF interpolation does not work for the structural force interpolation, this will be elaborated in Section 4.1.2

4.1.1. Displacement interpolation using radial basis functions

Radial basis functions use spline functions in the form of basis functions to interpolate the displacement over both the structural and aerodynamic interface:

$$u_{a,s}(x) = \sum_{i=1}^{n_{a,s}} \gamma_i \phi \left(\|x - x_i\| \right) + p(x) \tag{4.1}$$

In which $\|x - x_i\|$ is the euclidean distance from the centre at which the displacement is known to x, and $\phi\left(\|x\|\right)$ is the basis function with respect to the euclidean distance. The coefficients γ_i and the polynomial $p(x)$ are determined using the following requirements.

- The interpolated displacement $u(x)$ should match the nodal displacement at every node: $u(x_i) = u_i$
- $\sum_{i=1}^{n} \gamma_i q(x_i) = 0$, in which q is a polynomial with a degree that is equal to or less than that of polynomial p

Without going through the entire derivation of the transformation matrix, the aerodynamic displacements can be written in function of the structural displacement using a transformation matrix:

$$\mathbf{u}_a = \mathbf{T}_{sa} \mathbf{u}_s \tag{4.2}$$

According to Beckert and Wendland (2001), $\mathbf{T}_{sa}$ can be determined in the following manner:

$$\mathbf{T}_{sa} = \mathbf{A}_{as} \mathbf{C}_{ss}^{-1} \tag{4.3}$$

$\mathbf{C}_{ss}$ is given by:

$$\mathbf{C}_{ss} = \begin{bmatrix} 0 & 0 & 0 & 0 & 1 & 1 & \dots & 1 \\ 0 & 0 & 0 & 0 & x_{s1} & x_{s2} & \dots & x_{sNs} \\ 0 & 0 & 0 & 0 & y_{s1} & y_{s2} & \dots & y_{sNs} \\ 0 & 0 & 0 & 0 & z_{s1} & z_{s2} & \dots & z_{sNs} \\ 1 & x_{s1} & y_{s1} & z_{s1} & \phi_{s1,s1} & \phi_{s1,s1} & \dots & \phi_{s1,sNs} \\ 1 & x_{s2} & y_{s2} & z_{s2} & \phi_{s2,s1} & \phi_{s2,s2} & \dots & \phi_{s2,sNs} \\ \vdots & \vdots & \vdots & \vdots & \vdots & \vdots & \ddots & \vdots \\ 1 & x_{sNs} & y_{sNs} & z_{sNs} & \phi_{sNs,s1} & \phi_{sNs,s2} & \dots & \phi_{sNs,sNs} \end{bmatrix} \tag{4.4}$$

In the matrix above, N_s are the number of structural nodes and $\phi_{si,sj}$ is the radial basis function ϕ evaluated based on the euclidean distance between node i and j. Note that $\mathbf{C}_{ss}$ is only dependent on the structural mesh. $\mathbf{A}_{as}$ is written as:

$$\mathbf{A}_{as} = \begin{bmatrix} 1 & x_{a1} & y_{a1} & z_{a1} & \phi_{a1,s1} & \phi_{a1,s2} & \dots & \phi_{a1,sNS} \\ 1 & x_{a2} & y_{a2} & z_{a2} & \phi_{a2,s1} & \phi_{a2,s2} & \dots & \phi_{a2,sNS} \\ \vdots & \vdots & \vdots & \vdots & \vdots & \vdots & \ddots & \vdots \\ 1 & x_{aNa} & y_{aNa} & z_{aNa} & \phi_{aNa,s1} & \phi_{aNa,s2} & \dots & \phi_{aNa,sNS} \end{bmatrix} \tag{4.5}$$

N_a are the number of aerodynamic nodes, and for $\phi_{ai,sj}$, the euclidean distance between an aerodynamic and structure node is used.

Basis function choice

For the present model, the radial basis function ϕ with which the interpolation matrix is determined is one with a compact support. More specifically the one known as the Wendland's C^2-function Wendland (1995):

$$\phi\left(\|\mathbf{x}\|\right) = \left(1 - \frac{\|\mathbf{x}\|}{r}\right)_+^4 \cdot \left(4\frac{\|\mathbf{x}\|}{r} + 1\right) \tag{4.6}$$

In which r is the value of the support radius, and the plus sign denotes that only positive values are taken into account. Negative values arise when the euclidean distance becomes larger than the support radius r. This radial basis function has been chosen for a number of reasons.

The larger the support radius, the more structural nodes are taken into account to determine the displacement of the aerodynamic node. This increases the accuracy of the approximated displacement. However, if all structural nodes are taken into account, this also means that a full interpolation matrix is created. This is both more difficult to solve, and more importantly, it can lead to ill-conditioned matrices as nodes far from the aerodynamic node of interest contribute only very little to its displacement. Matrix ill-conditioning is a serious issue in this aeroelastic problem, due to the significant difference in the wing-box and plate stiffnesses. The support radius should be at least large enough so that the entire interpolation range is covered, which means that all aerodynamic nodes should be coupled to at least one structural node. The choice of increasing the value of r beyond that value is a trade-off between accuracy and matrix ill-conditioning. Compact support radial basis functions also decrease when the euclidean distance become larger, therefore the influence of local phenomena such as aerodynamic forces is taken into account better than by using global support functions, which smooth out displacements and forces to a larger extent.

2D versus 3D radial basis function

When the angle of attack α_0 is zero and there is little twist and dihedral in the wing, the distances in z direction between structure to structure nodes and structure to aerodynamic nodes can be very small, or zero. In this case, it is decided to ignore the distance between nodes in the z direction to make sure that $\mathbf{C}_{ss}$ remains invertible, and that the interpolation matrix does not become more ill-conditioned.

Displacements interpolation of large aspect ratio plates

In the case of large aspect ratio trailing edges, where the aspect ratio of the structural and aerodynamic elements become large, the distance between nodes in the chord-wise direction is much smaller than in span-wise direction. As a result, deformation in the chord-wise direction is taken into account more than the span-wise direction. The counter-intuitive consequence of this is a smoothing out of the chord-wise deformation and hence a poor aerodynamic mesh displacement, as can be seen in Figure **??**.
To correct this phenomenon, the length of the trailing edge is reduced in the span-wise direction, thereby scaling the aspect ratio. On the left side of Figure 4.2, the RBF interpolation of the structural displacement to the aerodynamic collocation points can be seen without a correction, and on the right side of Figure 4.2, the result for scaling the aspect ratio by a factor 10.

4.1.2. Force interpolation using an inverse distance weighted method

Similarly as with the displacement interpolation, the aerodynamic forces acting on the structural nodes can be written in function of the aerodynamic forces generated in the aerodynamic load locations:

$$\mathbf{F}_s = \mathbf{T}_{as}\mathbf{F}_a \tag{4.7}$$

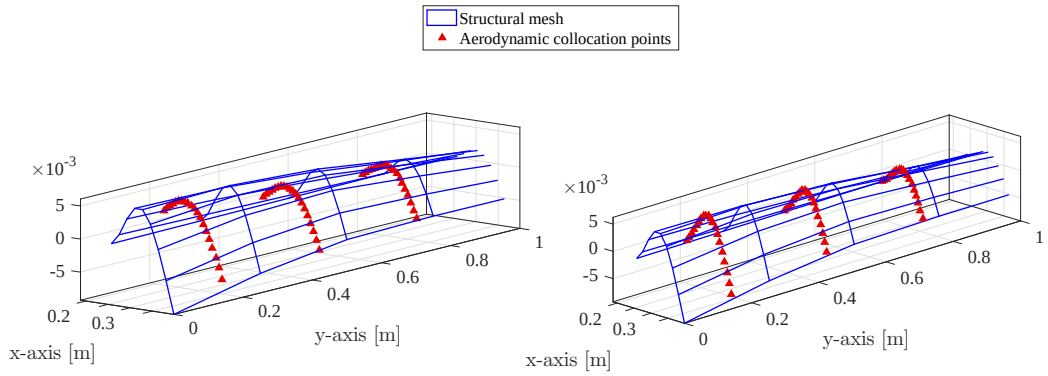

Figure 4.2: Part of the deformation of the flexible trailing edge, showing the structural mesh and aerodynamic collocation points without the aspect ratio correction (at the left side) and with the aspect ratio correction (at the right side).

The first option is to use the same RBF interpolation method which was used for the displacements. The aerodynamic to structures interpolation matrix $\mathbf{T}_{as}$ would simply be the transpose of the structures to aerodynamic interpolation matrix: $\mathbf{T}_{as} = \mathbf{T}_{sa}^{T}$.

Unfortunately, RBF interpolation does not work in all cases for load interpolation. The reason for this is that interpolation functions are used while some of the forces have to be extrapolated as the aerodynamic load locations are situated at the inside of a region of structural nodes, which can be seen in Figure 4.1. The structural nodes are also situated at the edges of the trailing edge, while the aerodynamic forces act at the midpoint of each of the bound vortex segment of a vortex element and are therefore always positioned inwards from the outer edges of the trailing edge. In Figure 4.3, it can be seen that large oscillations in the interpolated force on the structural mesh are present. RBF interpolation ensures that the total aerodynamic force is conserved, but the large oscillations clearly do not represent the actual pressure distribution over the wing. The result is that the deformation of the flexible trailing edge is not smooth, which can be seen in Figure 4.3. Note that the magnitude of the forces plotted in both figures below, do not use the same scale.

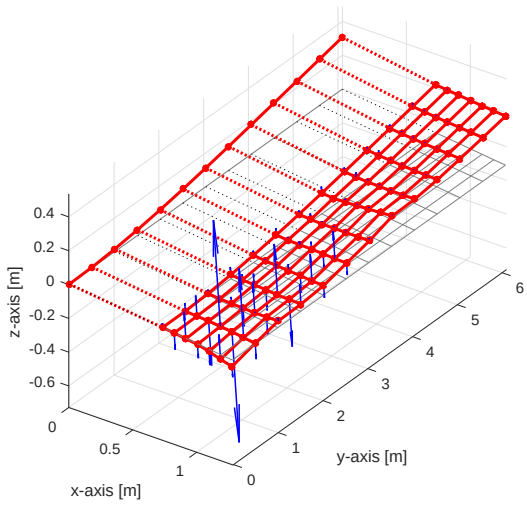

Figure 4.3: Aerodynamic forces on the structural nodes, using RBF interpolation, show large oscillations. Note that the forces are not up to scale.

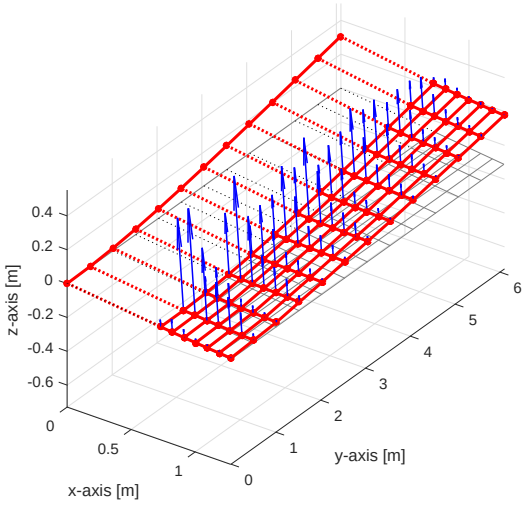

Figure 4.4: Aerodynamic forces on the structural nodes, using IDW interpolation, showing a much better load distribution and smoother trailing edge deformation. Note that the forces are not up to scale.

An alternative to RBF interpolation is nearest neighbour interpolation. However, for a flexible structure, it is important that the forces are spread properly to ensure a smooth deformation. Therefore it is chosen to use a method that spreads the forces more than the nearest neighbour interpolation.

The load in each aerodynamic force location is distributed over the four structural nodes enclosing it. These nodes are found by choosing the 4 nodes with the smallest euclidean distance to the aerodynamic force location. If the four closest structural nodes are chosen however, the distribution of forces is dependent on the structural mesh density in chord-wise direction. As can be seen in Figure 4.5, if an aerodynamic force location is positioned closely to the side of a structural plate element, nodes along the line in chord-wise direction are favoured, resulting in a poor span-wise distribution of the aerodynamic loads. If a restriction is set on the structural nodes enclosing a chord-wise segment over which the loads can be distributed, as can be seen in Figure 4.6, the 4 structural nodes enclosing the aerodynamic force are found.

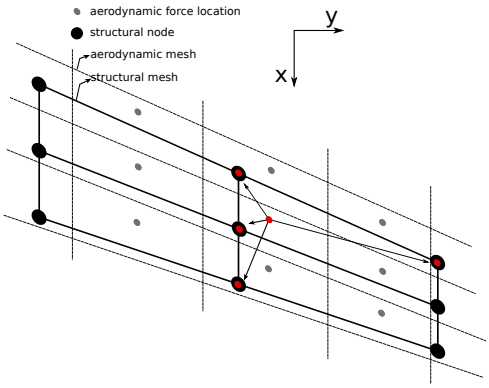

Figure 4.5: Schematic representation of the aerodynamic and structural mesh, showing the four closest structure nodes to an aerodynamic load location.

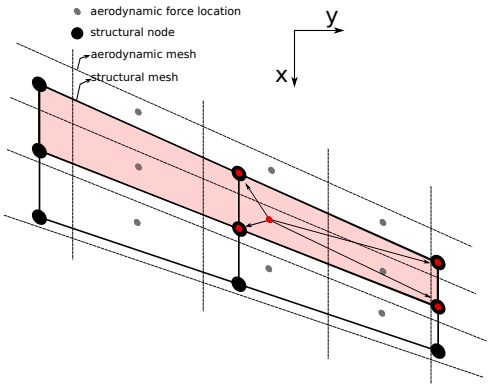

Figure 4.6: Correction to ensure that the 4 structural nodes closest to the aerodynamic load location are searched within a chord-wise segment indicated by the red area. This ensures that the 4 nodes enclosing the aerodynamic node are found.

The interpolation over the selected structural nodes is done using inverse distance weighting (IDW), in which the force on each node is proportional to the inverse of the euclidean distance to the aerodynamic force location:

$$\mathbf{F}_{s,i} = \frac{w_i(\|\mathbf{x}\|) \cdot \mathbf{F}_a}{\sum_{j=1}^{4} w_j(\|\mathbf{x}\|)} \tag{4.8}$$

in which the weight for each structural load w_i is given by:

$$w_i(\|\mathbf{x}\|) = \frac{1}{\|\mathbf{x} - \mathbf{x}_i\|} \tag{4.9}$$

4.1.3. Interpolation method mismatch: conservation of energy

The mismatch between the interpolation methods used for the deformations and forces, mean that the conservation of energy is not guaranteed. The virtual work performed by the aerodynamic loads on the aerodynamic mesh δW_a is not the same as the the virtual work done by the aerodynamic loads on the structural mesh δW_s:

$$\delta W_s = \delta \mathbf{u}_s^T \cdot \mathbf{F}_s \neq \delta \mathbf{u}_a^T \cdot \mathbf{F}_a = \delta W_a \tag{4.10}$$

In which $\delta \mathbf{u}_s$ and $\delta \mathbf{u}_a$ are the virtual displacements of the structural and aerodynamic mesh, and $\mathbf{F}_s$ and $\mathbf{F}_a$ are the aerodynamic loads on the structure and aerodynamic mesh. Although there is a difference, this does not necessarily mean that the interpolation methods can not be used. However, it is wise to check that the difference in work done on the aerodynamic mesh and structure mesh is not too large.

The work done on the aerodynamic and structural mesh in the aeroelastic model is calculated as follows:

$$W_s = \sum_{i=1}^{n_s} \mathbf{F}_{s,i} \mathbf{u}_{s,i} \tag{4.11}$$

$$W_a = \sum_{i=1}^{n_a} \mathbf{F}_{a,i} \mathbf{u}_{a,i} \tag{4.12}$$

In which n_s and n_a are the number of structural and aerodynamic nodes respectively. $\mathbf{u}_{s,i}$ and $\mathbf{u}_{a,i}$ are the translational deformation vector in each node of the structural and aerodynamic mesh. The difference in work done is then simply:

$$\Delta W = W_s - W_a \tag{4.13}$$

This difference is monitored during the aeroelastic analysis. For converged structural and aerodynamic meshes, this value has not become larger than 0.5%. Only for very course meshes of both the structural and aerodynamic meshes, or if only one of the meshes is too course, the difference in work done becomes larger than 1%.

4.1.4. Rotation matrix aerodynamic to structural reference system

To transform the aerodynamic forces, which are defined the aerodynamic reference system, to the structural reference system, an additional transformation matrix is required. The rotation matrix $\mathbf{R}_{as}$ is defined as follows, using the angle of attack α_0:

$$\mathbf{R}_{as} = \begin{bmatrix} \cos\alpha_0 & 0 & -\sin\alpha_0 \\ 0 & 1 & 0 \\ \sin\alpha_0 & 0 & \cos\alpha_0 \end{bmatrix} \tag{4.14}$$

4.2. Static analysis: closely coupled system

The static aeroelastic solution is found by writing the aeroelastic equilibrium of the closely coupled structural and aerodynamic system. Closely coupled means that no iterative solution is required to determine the converged static aeroelastic solution. In the present study, a linear analysis is done. For equilibrium, the internal forces of the structure at one hand have to equilibrate with the aerodynamic and external forces on the other hand:

$$\mathbf{f}(\mathbf{p}) = \mathbf{f}_a(\mathbf{p}) + \mathbf{f}_{ext}(\mathbf{p}) \tag{4.15}$$

As stated above, a linear static analysis is done, which leads to the following equilibrium equation

$$\mathbf{K}_s\mathbf{p} = \mathbf{F}_a + \mathbf{K}_a\mathbf{p} + \mathbf{F}_{ext} + \mathbf{K}_{ext}\mathbf{p} \tag{4.16}$$

In which $\mathbf{K}_s$, $\mathbf{K}_{ext}$ and $\mathbf{K}_a$ are the structural, external forces and aerodynamic stiffness matrix respectively. For a given flight velocity V_∞ and angle of attack α_0, an aerodynamic force vector $\mathbf{F}_a$ is calculated. The aerodynamic stiffness matrix then relates the change in aerodynamic forces to the structural deformation. The external stiffness matrix relates the change in external forces to the structural deformation. It must be noted that in the present study, external forces are not applied to the wing structure. The above equilibrium equation is implemented in the original PROTEUS code as well. The static aeroelastic model is only modified due to the changes in the structural and aerodynamic model, as discussed in Chapter 2 and 3, and will not be discussed further here.

In the static aeroelastic equilibrium equation, the reduced set of degrees of freedom $\mathbf{p}$ is used. This means that the aerodynamic and external forces and stiffness matrix have to be transformed to be compatible:

$$\mathbf{F}_a = \mathbf{T}_{ms}^T \mathbf{F^\star}_a \tag{4.17}$$

$$\mathbf{F}_{ext} = \mathbf{T}_{ms}^T \mathbf{F^\star}_{ext} \tag{4.18}$$

$$\mathbf{K}_a = \mathbf{T}_{ms}^T \mathbf{K^\star}_a \mathbf{T}_{ms} \tag{4.19}$$

$$\mathbf{K}_{ext} = \mathbf{T}_{ms}^{T} \mathbf{K^{\star}}_{ext} \mathbf{T}_{ms} \tag{4.20}$$

4.3. Dynamic analysis: aeroelastic state-space system

The aeroelastic state-space system is derived by coupling the structural and aerodynamic state-space systems. The input and output equations of the aerodynamic state-space system, which were derived in Section 3.2.3 are given by Equations (4.21) and (4.22):

$$\begin{Bmatrix} \dot{\mathbf{\Gamma}}_W \\ \dot{\boldsymbol{\alpha}} \end{Bmatrix} = \begin{bmatrix} \mathbf{K_1} & \mathbf{K_2} \\ \mathbf{0} & \mathbf{0} \end{bmatrix} \begin{Bmatrix} \mathbf{\Gamma}_W \\ \boldsymbol{\alpha} \end{Bmatrix} + \begin{bmatrix} \mathbf{0} \\ \mathbf{I} \end{bmatrix} \dot{\boldsymbol{\alpha}} \tag{4.21}$$

$$\begin{Bmatrix} \mathbf{F_b} \\ \mathbf{F_{TE}} \end{Bmatrix} = \begin{bmatrix} \mathbf{L}_{1_b} & \mathbf{L}_{2_b} \\ \mathbf{L}_{1_p} & \mathbf{L}_{2_p} \end{bmatrix} \begin{Bmatrix} \mathbf{\Gamma}_W \\ \boldsymbol{\alpha} \end{Bmatrix} + \begin{bmatrix} \mathbf{L}_{3_b} \\ \mathbf{L}_{3_p} \end{bmatrix} \dot{\boldsymbol{\alpha}} \tag{4.22}$$

The structural state-space system on the other hand is given by the following set of equations:

$$\begin{Bmatrix} \ddot{\mathbf{p}} \\ \dot{\mathbf{p}} \end{Bmatrix} = \begin{bmatrix} \mathbf{0} & -\mathbf{M}^{-1}\mathbf{K} \\ \mathbf{I} & \mathbf{0} \end{bmatrix} \begin{Bmatrix} \dot{\mathbf{p}} \\ \mathbf{p} \end{Bmatrix} + \begin{bmatrix} \mathbf{M}^{-1} \\ \mathbf{0} \end{bmatrix} \mathbf{F}_s \tag{4.23}$$

An output equation is not required in this case, since the structural deformations which would be the output of the structural state-space system are already given by the state vector itself. Adding the flexible trailing edge to the wing structure only adds degrees of freedom to the structural state-space system. The aerodynamic state vector remains the same, e.g. the wake panel's vortex strengths and the perturbance angle of attack of each of the individual body panels on the wing.

A clear derivation of the aeroelastic state-space system for a chord-wise rigid wing is given by Werter and De Breuker (2016). First, the aerodynamic input and output equation can be linked to the structural deformation, by writing the perturbation angle of attack in function of the structural degrees of freedom. For a chord-wise rigid wing, the perturbation angle of attack is given by the following equation:

$$\alpha_b = \alpha_{air} + \theta - \frac{\dot{h}}{V_\infty} + \frac{\dot{\theta}(x - x_b)}{V_\infty} \tag{4.24}$$

In which α_{air} is the free stream angle of attack and θ the aerodynamic pitch angle. $\dot{h}$ is the plunge rate, which is the motion of the wing in the global z-direction, and $\dot{\theta}$ the pitch rate, which is the angular velocity around the reference axis. These are depicted in Figure 4.7, and it can be seen that they are defined at the aerodynamic reference axis. The pitch rate around this axis therefore increases the local plunge rate depending on the distance of a vortex panel to the reference axis.

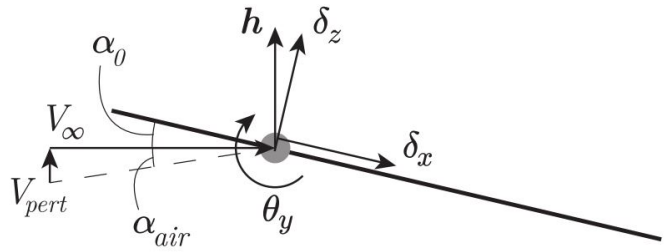

Figure 4.7: Angle of attack of a rigid airfoil section and its individual components.

The angle of attack caused by the flexible deformation of the trailing edge is a function of the plunge rate and pitch of the individual panels. Not of the pitch rate, since that is already taken into account by the motion of the plate elements. This is because, for the chord-wise rigid wing, the motion of all the aerodynamic panels were defined using only the motion of the reference axis. While for the flexible trailing edge, each of the plate elements can have a different plunge velocity. The relation for the perturbation angle of attack of the trailing edge can therefore be written as:

$$\alpha_{te} = \alpha_{air} + \theta - \frac{\dot{h}}{V_\infty} \tag{4.25}$$

These variables can be related to the structural deformation using Figure 4.7.

Due to different reference systems used in the aerodynamic and structural model, the aerodynamic plunge motion $\dot{\mathbf{h}}_a$, has to be written as a function of the structural degrees of freedom as follows:

$$\dot{\mathbf{h}}_a = -\sin\alpha_0 \cdot \mathbf{T}_{sa}\dot{\boldsymbol{\delta}}_{x,s} + \cos\alpha_0 \cdot \mathbf{T}_{sa}\dot{\boldsymbol{\delta}}_{z,s} \tag{4.26}$$

In the above equation, α_0 is the free stream angle of attack, and $\dot{\boldsymbol{\delta}}_{x,s}$ and $\dot{\boldsymbol{\delta}}_{z,s}$ are the structural displacements in the x and z direction.
Substituting the perturbation angle of attack of the wing α given by Equations (4.24) and (4.25) into the aerodynamic input and output equations yields:

$$\begin{Bmatrix} \dot{\boldsymbol{\Gamma}}_W \\ \dot{\boldsymbol{\alpha}}_{air} \end{Bmatrix} = \underbrace{\begin{bmatrix} \mathbf{K_1} & \mathbf{K_2} & \frac{\sin\alpha_0}{V_\infty}\mathbf{K_2}\mathbf{B}_\alpha\mathbf{T}_{sa} & -\frac{\cos\alpha_0}{V_\infty}\mathbf{K_2}\mathbf{B}_\alpha\mathbf{T}_{sa} & \mathbf{K_2}\mathbf{B}_\alpha\mathbf{T}_{sa} & \mathbf{K_2}\mathbf{B_{pitch}}\mathbf{T}_{sa} \\ \mathbf{0} & \mathbf{0} & \mathbf{0} & \mathbf{0} & \mathbf{0} & \mathbf{0} \end{bmatrix}}_{\mathbf{H}_1}$$
$$\times \begin{Bmatrix} \boldsymbol{\Gamma_W} \\ \boldsymbol{\alpha}_{air} \\ \dot{\boldsymbol{\delta}}_{x,s} \\ \dot{\boldsymbol{\delta}}_{z,s} \\ \boldsymbol{\theta}_{y,s} \\ \dot{\boldsymbol{\theta}}_{y,s} \end{Bmatrix} + \underbrace{\begin{bmatrix} \mathbf{0} \\ \mathbf{I} \end{bmatrix}}_{\mathbf{H}_2} \dot{\boldsymbol{\alpha}}_{air} \tag{4.27}$$

$$\mathbf{F}_a = \underbrace{\begin{bmatrix} \mathbf{L}_1 & \mathbf{L}_2 & \frac{\sin\alpha_0}{V_\infty}\mathbf{L_2}\mathbf{B}_\alpha\mathbf{T}_{sa} & -\frac{\cos\alpha_0}{V_\infty}\mathbf{L_2}\mathbf{B}_\alpha\mathbf{T}_{sa} & \mathbf{L_2}\mathbf{B}_\alpha\mathbf{T}_{sa} & \left(\mathbf{L_2}\mathbf{B_{pitch}} + \mathbf{L_3}\mathbf{B}_\alpha\right)\mathbf{T}_{sa} \end{bmatrix}}_{\mathbf{H}_3}$$
$$\times \begin{Bmatrix} \boldsymbol{\Gamma_W} \\ \boldsymbol{\alpha}_{air} \\ \dot{\boldsymbol{\delta}}_{x,s} \\ \dot{\boldsymbol{\delta}}_{z,s} \\ \boldsymbol{\theta}_{y,s} \\ \dot{\boldsymbol{\theta}}_{y,s} \end{Bmatrix} + \underbrace{\begin{bmatrix} \frac{\sin\alpha_0}{V_\infty}\mathbf{L_3}\mathbf{B}_\alpha\mathbf{T}_{sa} & -\frac{\cos\alpha_0}{V_\infty}\mathbf{L_3}\mathbf{B}_\alpha\mathbf{T}_{sa} & \mathbf{L_3}\mathbf{B_{pitch}}\mathbf{T}_{sa} \end{bmatrix}}_{\mathbf{H}_4} \times \begin{Bmatrix} \ddot{\boldsymbol{\delta}}_{z,s} \\ \ddot{\boldsymbol{\delta}}_{x,s} \\ \ddot{\boldsymbol{\theta}}_{y,s} \end{Bmatrix} \mathbf{L_3}\mathbf{B}_\alpha\dot{\boldsymbol{\alpha}}_{air} \tag{4.28}$$

In the equations above, $\mathbf{B}_\alpha$ relates the span-wise distribution of displacements and rotations to the correct aerodynamic panels, for the chord-wise rigid part of the wing. $\mathbf{B_{pitch}}$ has the same function, but translates the span-wise pitch rate to the local plunge rate of the aerodynamic panels. For the trailing edge aerodynamic panels, $\mathbf{B}_\alpha$ is simply an identity matrix, since the plunge and pitch rate are given for each aerodynamic panel, and not only the span-wise distribution. $\mathbf{B}_\alpha$ is therefore given by:

$$\mathbf{B}_\alpha = \begin{bmatrix} \mathbf{I}_{N_b} & \mathbf{0} & \mathbf{0} \\ \mathbf{I}_{N_b} & \mathbf{0} & \mathbf{0} \\ \vdots & \vdots & \vdots \\ \mathbf{I}_{N_b} & \mathbf{0} & \mathbf{0} \\ \mathbf{0} & \mathbf{I}_{N_{TE}} & \end{bmatrix} \tag{4.29}$$

In which N_b is the number of span-wise aerodynamic panels and N_{TE} the number of aerodynamic panels on the trailing edge. The next step is to link the structural pitch and plunge position and rates from the vectors $\begin{Bmatrix} \dot{\boldsymbol{\delta}}_{x,s} & \dot{\boldsymbol{\delta}}_{z,s} & \boldsymbol{\theta}_{y,s} & \dot{\boldsymbol{\theta}}_{y,s} \end{Bmatrix}^T$ and $\begin{Bmatrix} \ddot{\boldsymbol{\delta}}_{z,s} & \ddot{\boldsymbol{\delta}}_{x,s} & \ddot{\boldsymbol{\theta}}_{y,s} \end{Bmatrix}^T$ to the structural degrees of freedom $\mathbf{p}$ and their time derivatives $\dot{\mathbf{p}}$. This is done using matrices which retrieve the correct entries from the vector of degrees of freedom.
With the aeroelastic state vector given by:

$$\mathbf{x} = \begin{Bmatrix} \boldsymbol{\Gamma_W} \\ \boldsymbol{\alpha}_{air} \\ \mathbf{p} \\ \dot{\mathbf{p}} \end{Bmatrix} \tag{4.30}$$

the aerodynamic input and output equation of the state-space equations can be simplified:

$$\begin{Bmatrix} \dot{\boldsymbol{\Gamma}}_W \\ \dot{\boldsymbol{\alpha}}_{air} \end{Bmatrix} = \mathbf{H}_1\mathbf{T}_1\mathbf{x} + \mathbf{H}_2\dot{\boldsymbol{\alpha}}_{air} \tag{4.31}$$

$$\mathbf{F}_a = \mathbf{H}_3\mathbf{T}_1\mathbf{x} + \mathbf{H}_4\mathbf{T}_2\dot{\mathbf{x}}_s + \mathbf{L}_3\mathbf{B}_\alpha\dot{\boldsymbol{\alpha}}_{air} \tag{4.32}$$

In which $\mathbf{T}_1$ and $\mathbf{T}_2$ contains the matrices to link the structural degrees of freedom to the structural pitch and plunge position and rates. $\dot{\mathbf{x}}_s$ is the time derivative of the structural state vector.
The second step in deriving the aeroelastic state-space system is substituting the aerodynamic forces into the structural state-space equation. This means substituting Equation (4.32) into Equation (4.23). The structural state-space system is given by:

$$\begin{Bmatrix} \ddot{\mathbf{p}} \\ \dot{\mathbf{p}} \end{Bmatrix} = \underbrace{\begin{bmatrix} \mathbf{0} & -\mathbf{M}^{-1}\mathbf{K} \\ \mathbf{I} & \mathbf{0} \end{bmatrix}}_{\mathbf{A}_s} \underbrace{\begin{Bmatrix} \dot{\mathbf{p}} \\ \mathbf{p} \end{Bmatrix}}_{\mathbf{x}_s} + \underbrace{\begin{bmatrix} \mathbf{M}^{-1} \\ \mathbf{0} \end{bmatrix}}_{\mathbf{B}_s} \mathbf{T}_{as}\mathbf{R}_{as}\mathbf{F}_a \tag{4.33}$$

The substitution of the aerodynamic forces $\mathbf{F}_a$ into the structural forces $\mathbf{F}_s$ requires a rotation to the structural reference system, using $\mathbf{R}_{as}$ and the force interpolation matrix $\mathbf{T}_{as}$.
Now, substituting Equation (4.32) into Equation (4.33) yields:

$$\underbrace{\left(\mathbf{I} - \mathbf{B}_s\mathbf{T}_{as}\mathbf{R}_{as}\mathbf{H}_4\mathbf{T}_2\right)}_{\mathbf{H}_5}\dot{\mathbf{x}}_s = \underbrace{\left(\mathbf{A}_s\mathbf{T}_3 + \mathbf{B}_s\mathbf{T}_{as}\mathbf{R}_{as}\mathbf{H}_3\mathbf{T}_1\right)}_{\mathbf{H}_6}\mathbf{x} + \underbrace{\mathbf{B}_s\mathbf{T}_{as}\mathbf{R}_{as}\mathbf{L}_3\mathbf{B}_\alpha}_{\mathbf{H}_7}\dot{\boldsymbol{\alpha}}_{air} \tag{4.34}$$

Which can be rewritten as:

$$\dot{\mathbf{x}}_s = \mathbf{H}_5^{-1}\mathbf{H}_6\mathbf{x} + \mathbf{H}_5^{-1}\mathbf{H}_7\dot{\boldsymbol{\alpha}}_{air} \tag{4.35}$$

The state equation of the aeroelastic state-space system can now be completed by combining Equations (4.31) and (4.35), which yields:

$$\dot{\mathbf{x}} = \underbrace{\begin{bmatrix} \mathbf{H}_1\mathbf{T}_1 \\ \mathbf{H}_5^{-1}\mathbf{H}_6 \end{bmatrix}}_{\mathbf{A}_{ss}}\mathbf{x} + \underbrace{\begin{bmatrix} \mathbf{H}_4 \\ \mathbf{H}_5^{-1}\mathbf{H}_7 \end{bmatrix}}_{\mathbf{B}_{ss}}\dot{\boldsymbol{\alpha}}_{air} \tag{4.36}$$

The aeroelastic state equation of the state-space system has now been written for the complete set of structural degrees of freedom. As explained in Section 2.5, transforming the structural state-space system to the reduced set of master-slave degrees of freedom could not be done by pre- and post-multiplying the structural state matrix $\mathbf{A_s}$. Instead, the individual components of the state matrix had to be transformed. The same has to be done with the aeroelastic state-space system.

The structural state-space system is first reduced to the master-slave set of degrees of freedom. In which the structural stiffness and mass matrix $\mathbf{K}$ and $\mathbf{M}$ are transformed by:

$$\mathbf{K} = \mathbf{T}_{ms}^T \mathbf{K}^\star \mathbf{T}_{ms} \tag{4.37}$$

$$\mathbf{M} = \mathbf{T}_{ms}^T \mathbf{M}^\star \mathbf{T}_{ms} \tag{4.38}$$

In which $\star$ indicates the full set of degrees of freedom. The external forces on the structure can be transformed as follows:

$$\mathbf{F}_s = \mathbf{T}_{ms}^T \mathbf{F}_s^\star \tag{4.39}$$

And hence, the aerodynamic forces are given by:

$$\mathbf{F}_a = \mathbf{T}_{ms}^T \mathbf{T}_{as} \mathbf{R}_{as} \mathbf{F}_a^\star \tag{4.40}$$

The introduction of $\mathbf{T}_{ms}^T$ in the aerodynamic force equation, means that $\mathbf{H}_5$, $\mathbf{H}_6$ and $\mathbf{H}_7$ have to be modified:

$$\mathbf{H}_5 = \mathbf{I} - \mathbf{B}_s \mathbf{T}_{ms}^T \mathbf{T}_{as} \mathbf{R}_{as} \mathbf{H}_4 \mathbf{T}_2 \tag{4.41}$$

$$\mathbf{H}_6 = \mathbf{A}_s \mathbf{T}_3 + \mathbf{B}_s \mathbf{T}_{ms}^T \mathbf{T}_{as} \mathbf{R}_{as} \mathbf{H}_3 \mathbf{T}_1 \tag{4.42}$$

$$\mathbf{H}_7 = \mathbf{B}_s \mathbf{T}_{ms}^T \mathbf{T}_{as} \mathbf{R}_{as} \mathbf{L}_3 \mathbf{B}_\alpha \tag{4.43}$$

Several components in the aeroelastic state matrix now have to be transformed, to make them compatible with the reduced set of structural degrees of freedom. In Equation (4.36), $\mathbf{A}_{ss}$ is multiplied by the state vector $\mathbf{x}$, which now contains the reduced set of structural degrees of freedom. The components of $\mathbf{A}_{ss}$ which are multiplied with $\{\boldsymbol{\Gamma_W} \quad \boldsymbol{\alpha}_{air}\}^T$, do not have to be changed, only those which correspond to $\{\mathbf{p} \quad \dot{\mathbf{p}}\}^T$.
The transformation to the reduced state vector is given by:

$$\begin{Bmatrix} \boldsymbol{\Gamma_W} \\ \boldsymbol{\alpha}_{air} \\ \mathbf{p}^\star \\ \dot{\mathbf{p}}^\star \end{Bmatrix} = \underbrace{\begin{bmatrix} \mathbf{I}_{\Gamma_W} & \mathbf{0} & \mathbf{0} & \mathbf{0} \\ \mathbf{0} & \mathbf{I}_{\alpha_{air}} & \mathbf{0} & \mathbf{0} \\ \mathbf{0} & \mathbf{0} & \mathbf{T}_{ms} & \mathbf{0} \\ \mathbf{0} & \mathbf{0} & \mathbf{0} & \mathbf{T}_{ms} \end{bmatrix}}_{\mathbf{T}_4} \begin{Bmatrix} \boldsymbol{\Gamma_W} \\ \boldsymbol{\alpha}_{air} \\ \mathbf{p} \\ \dot{\mathbf{p}} \end{Bmatrix} \tag{4.44}$$

In the state matrix $\mathbf{A}_{ss}$, $\mathbf{H}_1\mathbf{T}_1$ can be right-multiplied by $\mathbf{T}_4$, but the second row of $\mathbf{A}_{ss}$ requires more care. In $\mathbf{H}_6$, the term $\mathbf{A}_s\mathbf{T}_3$, does not have to be multiplied by $\mathbf{T}_4$ anymore, since the structural state-space system is already transformed to the master-slave set of degrees of freedom. And looking at Equation (4.34), it can be seen that $\mathbf{H}_5$ is right-multiplied by the time derivative of the structural state vector, therefore it also has to be right-multiplied by $\mathbf{T}_{ms}$. Hence, first $\mathbf{H}_5$ and $\mathbf{H}_6$ are transformed:

$$\mathbf{H}_5 = (\mathbf{I} - \mathbf{B}_s \mathbf{T}_{ms}^T \mathbf{T}_{as} \mathbf{R}_{as} \mathbf{H}_4 \mathbf{T}_2) \cdot \begin{bmatrix} \mathbf{T}_{ms} & \mathbf{0} \\ \mathbf{0} & \mathbf{T}_{ms} \end{bmatrix} \tag{4.45}$$

$$\mathbf{H}_6 = \mathbf{A}_s \mathbf{T}_3 + \mathbf{B}_s \mathbf{T}_{ms}^T \mathbf{T}_{as} \mathbf{R}_{as} \mathbf{H}_3 \mathbf{T}_1 \cdot \mathbf{T}_4 \tag{4.46}$$

And with the modified matrices $\mathbf{H}_5$ and $\mathbf{H}_6$, the state matrix $\mathbf{A}_{ss}$ can be written as:

$$\mathbf{A}_{ss} = \begin{bmatrix} \mathbf{H}_1 \mathbf{T}_1 \mathbf{T}_4 \\ \mathbf{H}_5^{-1} \mathbf{H}_6 \end{bmatrix} \tag{4.47}$$

4.3.1. Stability analysis

The stability of the aeroelastic system is assessed by looking at the eigenvalues of the state matrix $\mathbf{A}_{ss}$. Three types of instability can occur in this aeroelastic system: divergence, airfoil flutter and plate flutter. Divergence is a static phenomenon, taking place at a velocity at which the structure cannot sustain the increasing aerodynamic moment. Naturally, the frequency that accompanies this instability is $0Hz$. Airfoil flutter can be described as a combination of the plunging and pitching moment of the entire wing. The frequencies of this instability are in the order of magnitude of the structural eigenfrequency of the wing-box structure. Finally, the flutter mode introduced with the flexibility of the trailing edge is plate flutter, with flutter frequencies roughly in the range of the first couple of eigenfrequencies of the plate structure.

Solving an aeroelastic problem with a discretised model, results in a high number of eigenvalues. To be able to track the eigenmodes which are the most critical and can possibly become unstable, other eigenvalues are filtered out. Eigenvalues are first sorted based on their real part. A positive real part means positive damping, corresponding to an unstable mode. Although at some velocity, the flutter or divergent modes are the most critical, before that velocity is reached, many higher frequency modes are more critical as their damping ratio is closer to (but sill below) zero. This is due to the fact that they have very little aerodynamic damping and no structural damping is included in this model. This is a handicap in finding the flutter velocity, since it is more difficult to locate where the first eigenmode becomes unstable.
To mitigate this problem, higher frequency modes are cut-off, based on the structural eigenfrequencies. Since the flexible plate and the wing-box can have substantially different eigenfrequencies, and those of the trailing edge are higher, the cut-off frequency is based on the trailings edge structural eigenfrequencies.

4.4. Verification

The aeroelastic system of a wing with flexible trailing edge is verified in two steps. First, the trailing edge aeroelastic model is verified without the influence of the beam model in Section 4.4.1, looking at plate flutter and a plate-like wing. Secondly, it is checked whether the stability of the model converges to the PROTEUS model for a stiff, short and light trailing edge, in Section 4.4.2. This is done to make sure the modifications to the PROTEUS model did not alter the stability behaviour of the wing-box structure for a quasi chord-wise rigid trailing edge.

4.4.1. Verification of the trailing edge

To verify the aeroelastic model of the flexible trailing edge without the influence of the beam model, 2 cases are investigated: plate flutter of a quasi two-dimensional panel and the stability of a cantilevered plate wing.

Case 1: plate flutter

With the present model, the flutter speed and corresponding mode shape are computed, and compared with numerical and experimental results from reference Tang et al. (2003). In this reference, flutter of a two-dimensional panel in three-dimensional axial flow is simulated and compared to experiments. The plate is clamped at its leading edge by a rigid airfoil, this leads to the following configuration of a partially rigid cantilevered plate. A schematic is shown below in Figure 4.8.

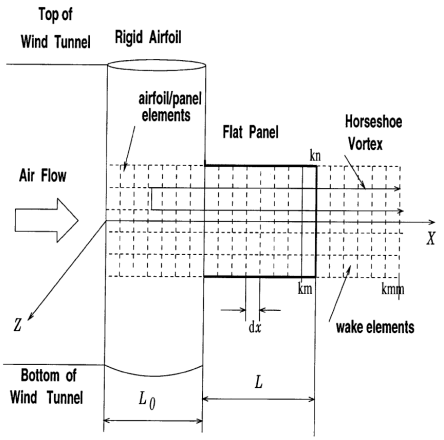

Figure 4.8: Schematics of the geometry of the rigid airfoil and flexible plate

Table 4.1: Dimensions and material properties

L	0.27 m
L_0	0.1 m
t	0.00039 m
E	72 GPa
ν	0.3 —
ρ	2840 kg/m^3
ξ_{damp}	0.005 —

A three-dimensional linear unsteady vortex-lattice model is used to model the aerodynamics, combined with a non-linear 2-dimensional structural model with an axially inextensible assumption, including stiffness and inertia non-linearities. The dimensions and material properties of the partially rigid cantilevered plate used in the experiment and simulation are given in Table 4.1.

The present model consists of beam elements representing the wing-box structure of the wing and plate elements representing the trailing edge. To model the current case, the stiffness of the beam elements is increased and their mass decreased such that it has a negligible effect on the mass of the total structure and does not deform under the applied aerodynamic load. The structure is discretised using 5 span-wise elements and 16 plate elements in chord-wise direction. The aerodynamic mesh has 10 span-wise elements and 24 chord-wise elements, of which 8 are on the rigid part and 16 on the flexible part. The wake is truncated at 20 times the chord length and using 320 chord-wise elements.

The present aerodynamic model is symmetric around the root of the wing, therefore the width of the panel modelled is half of the width used in the verification case. In the structural model, symmetry

conditions are applied by setting the following degrees of freedom to zero at the side of the panel, at $y = 0$: $\theta_x = \theta_z = v = 0$.

The flutter speed is found by increasing the free stream velocity until the real part of any of the eigenvalues becomes positive, which corresponds to negative damping and an unstable system. The computed flutter speed matches the results from Tang et al. (2003) quite well, as can be seen in Table 4.2.

Table 4.2: Flutter speed and frequency of a partially rigid cantilevered plate.

	V_f	ω_f
Tang et al.	29.5 m/s	22.5 Hz
Present	27.04 m/s	22.44 Hz

The difference in flutter speed can be explained by two differences between the present model and the model from Tang et al. (2003). Material damping is neglected in the present model but can have a significant effect on the stability of cantilevered plates. Secondly, a 2-dimensional structural model has been used by Tang et al. (2003). Although a non-linear structural model has been used in the reference study, the flutter speed was determined by analysing the eigenvalues of the linearised system. The flutter mode shape can also be compared by inspecting Figures 4.9 and 4.10.

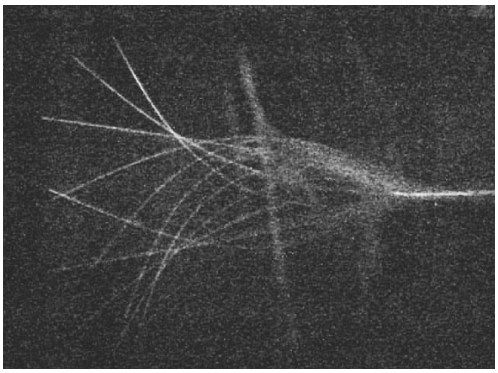

Figure 4.9: Experimental plate's vibration mode at 29.8 m/s.

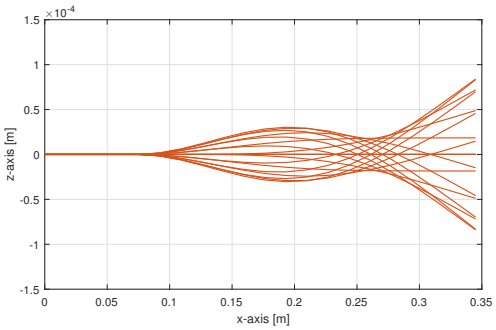

Figure 4.10: Computed mode shape at $V_f = 27.04\ m/s$.

The mode shapes look very similar, although the bottleneck which can be seen in the computed mode shape is not so distinct in the experiment. If the velocity is increased in the simulation to 30 and 35 m/s, this bottleneck also fades looking at Figures 4.11 and 4.12, as the first and second bending mode interact more strongly.

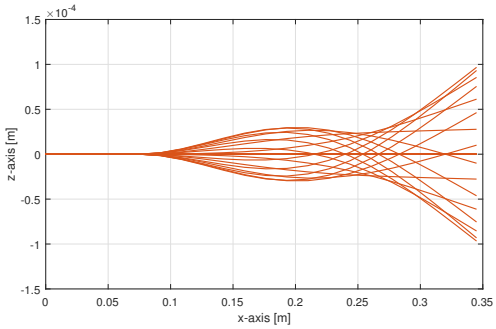

Figure 4.11: Computed mode shape at $V = 30.19\ m/s$.

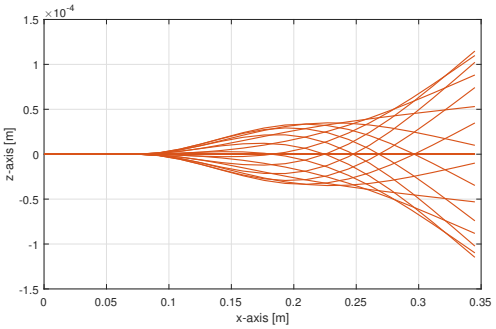

Figure 4.12: Computed mode shape at $V = 35\ m/s$.

The flutter diagram is shown for further understanding of the stability of the aeroelastic system. On the right side of Figure 4.13, it can be seen that as the frequency branches of the first and second mode move closer together, the second mode becomes unstable. Many higher frequency modes are also visible in the damping versus velocity plot, but they are all stable in the inspected velocity range.

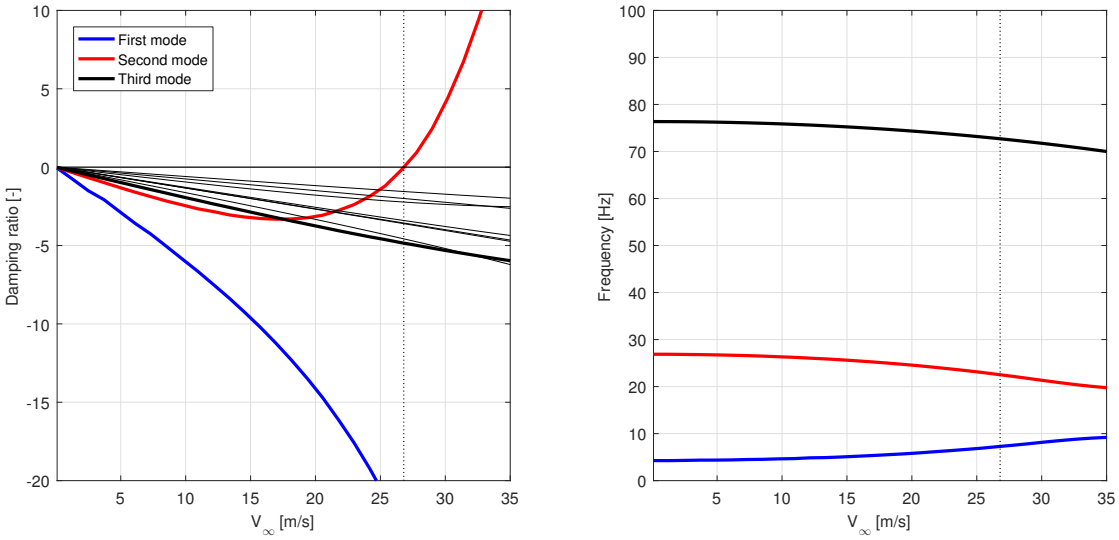

Figure 4.13: Flutter diagram: damping and frequency versus flow velocity.

The first flutter mode, indicated by the red line in Figure 4.13, is depicted in Figure 4.14.

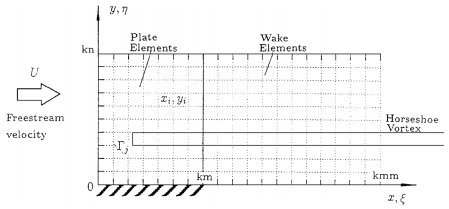

Figure 4.15: Schematics of the geometry of the cantilever plate wing

Table 4.3: Dimensions and material properties

$Semispan$	0.1524 m
$Chord$	0.3 m
t	0.001 m
E	69 GPa
ν	0.3 —
ρ	2700 kg/m^3

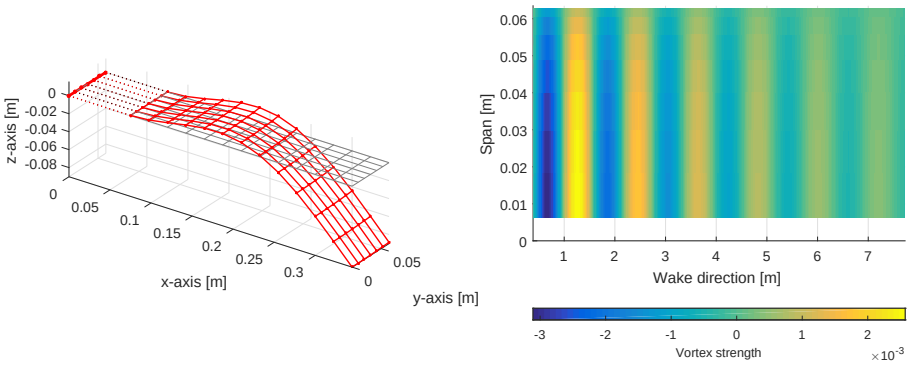

Figure 4.14: Flutter mode of the first verification case. The left side shows the structural deformation, and the right side the vortex strength of the wake panels.

Case 2: plate-like wing

The second verification case is a cantilever plate wing modelled by Tang et al. (1999a). A schematic representation of this wing is shown in Figure 4.15. Like the previous verification case, limit cycle oscillations were the main subject of the study, but the stability of the linearised system has been investigated as well. The advantage of this verification case is that a three-dimensional plate structure is considered, and that material damping is not taken into account. So the critical velocity and frequency should be closer to those found in the given reference. A three-dimensional unsteady vortex lattice model is used in combination with a non-linear structural model based on the von Karman plate equations. The dimensions and material properties were not specified clearly in the given reference. Therefore the material density and Young's modulus were based on the properties of the 6061 aluminium alloy.

To reduce the effect of the beam elements in front of the plate structure on the dynamic behaviour of the total structure, the stiffness and mass of these elements is set to a very low value. The length of the rigid part in chord direction is also reduced to a very small value and it must be noted that therefore the dimensions of the vortex elements on the rigid section become very narrow. The structure is discretised

using 8 span-wise elements and 12plate elements in chord direction. The aerodynamic mesh consists of 8 span-wise elements and 24 chord-wise elements. The wake is truncated at 20 times the chord length and discretised using 320 chord-wise elements.

In the given reference, the stability analysis was done for a range of different aspect ratio's, showing how the flutter velocity decreases with increasing aspect ratio, leaving all other variables constant. The damping versus velocity and root locus plot are shown for an aspect ratio of 1 in Figures 4.16 and 4.17.

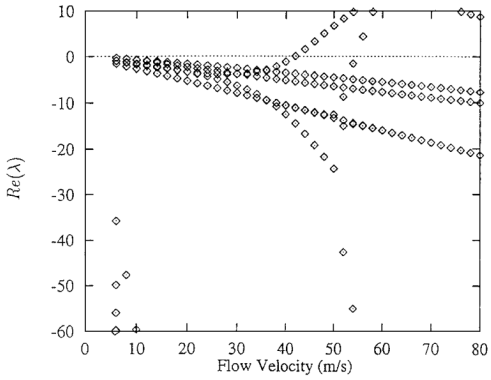

Figure 4.16: Damping versus velocity for $AR = 1$, plots taken from Tang et al. (1999a).

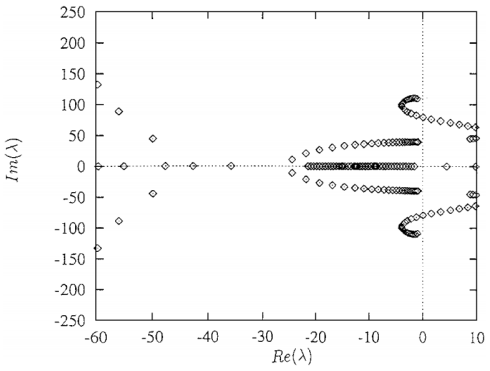

Figure 4.17: Root locus plot of the aeroelastic system for $AR = 1$, plots taken from Tang et al. (1999a).

For the present study, the stability analysis is done for the same aspect ratio. This is shown in Figure 4.18.

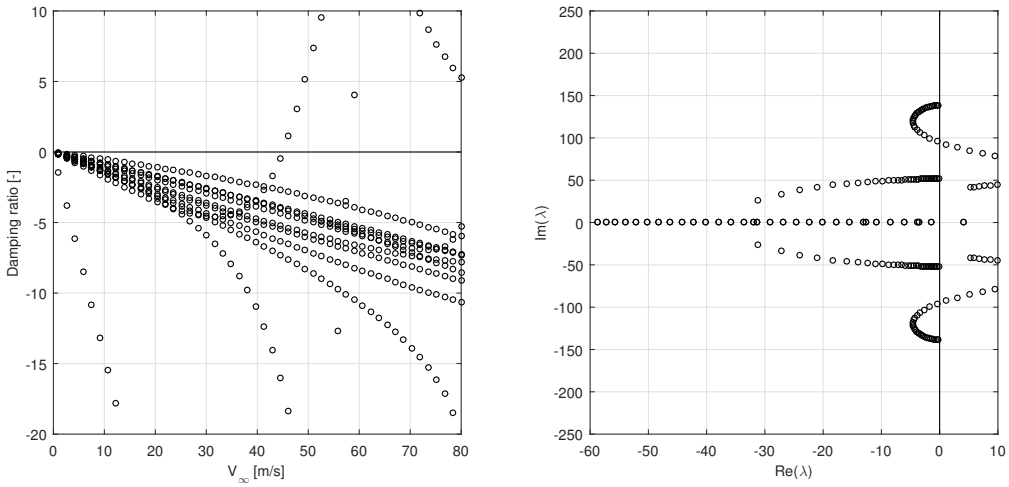

Figure 4.18: Damping versus flow velocity and root locus plot for $AR = 1$.

The first flutter mode of this verification case is depicted in Figure 4.19.

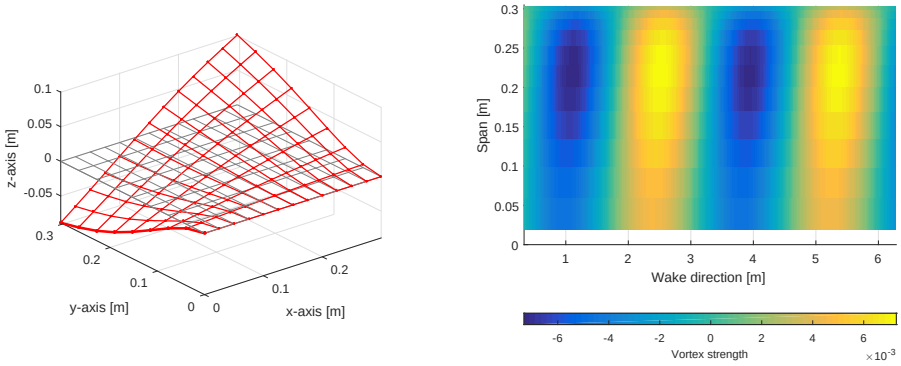

Figure 4.19: Flutter mode of the second verification case. The left side shows the structural deformation, and the right side the vortex strength of the wake panels.

Although the flutter diagrams of the present study and the reference study are qualitatively the same, the velocity of flutter and the corresponding frequency do not match. However, since the material properties and dimensions are not defined clearly in the reference, it cannot be said that either of the results is incorrect. Comparing the first three plate natural frequencies computed by Tang et al. (1999a), with the present model and the linear perturbation analysis of Abaqus (shown in Table 4.4), there clearly is a large difference. The differences between Tang et al. (1999a) at one side and the present model and Abaqus at the other side could be due to a mismatch in the material density, Young's modulus or plate dimensions.

Table 4.4: The first three plate natural frequencies

	$\omega_1 1$	ω_2	ω_3
Tang et al.	$6.5\ Hz$	$18.2\ Hz$	$58.9\ Hz$
Present	$8.49\ Hz$	$21.79\ Hz$	$52.48\ Hz$
Abaqus	$8.52\ Hz$	$21.68\ Hz$	$53.65\ Hz$

Although these structural eigenfrequencies do not match well, the general behaviour of the plate-like wing is correct, with similar damping versus velocity and root locus plots. The first flutter mode to become unstable is due to an interaction between the plate's first bending and torsion mode. At a higher velocity, divergence becomes the dominant instability.

4.4.2. Convergence towards PROTEUS model

Although there are no verification cases available for a wing with a flexible trailing edge, the model with flexible trailing edge should converge towards a wing which is rigid in chord-wise direction. For this purpose, the geometry and structural properties of the Goland wing Goland (1945), are used. The aeroealistic PROTEUS model is compared to a model with a flexible trailing edge which is short, stiff and light, so that its influence on the aeroelastic behaviour of the wing are minimal.
In the thesis of Werter (2012), this wing was chosen to validate the dynamic aeroelastic model as well. The same aerodynamic mesh and structural beam mesh is used here, only the aerodynamic panels in chord-wise direction are divided over the rigid and flexible part, assigning half of the elements to each region:

Table 4.5: Aerodynamic mesh parameters

N_{span}	16
N_{chord}	32
N_{wake}	128

Table 4.6: Structural mesh parameters

N_{span}	16
$N_{chord,TE}$	8

The flexible trailing edge in this simulation has the following properties: its length is 5% of the total chord length, the density 1% of that of aluminium alloy ($\rho = 27.5 kg/m^3$), and its thickness is $2mm$. A low density is chosen, so that it does not significantly change the dynamic properties of the Goland wing.

In Figure 4.20, it can be seen that the flutter diagram of the Goland using both the PROTEUS model and the model with a flexible trailing edge match very well, hence it is fair to say that the model including the flexible trailing edge converges to a chord-wise rigid wing if the trailing edge is stiff, light and short.

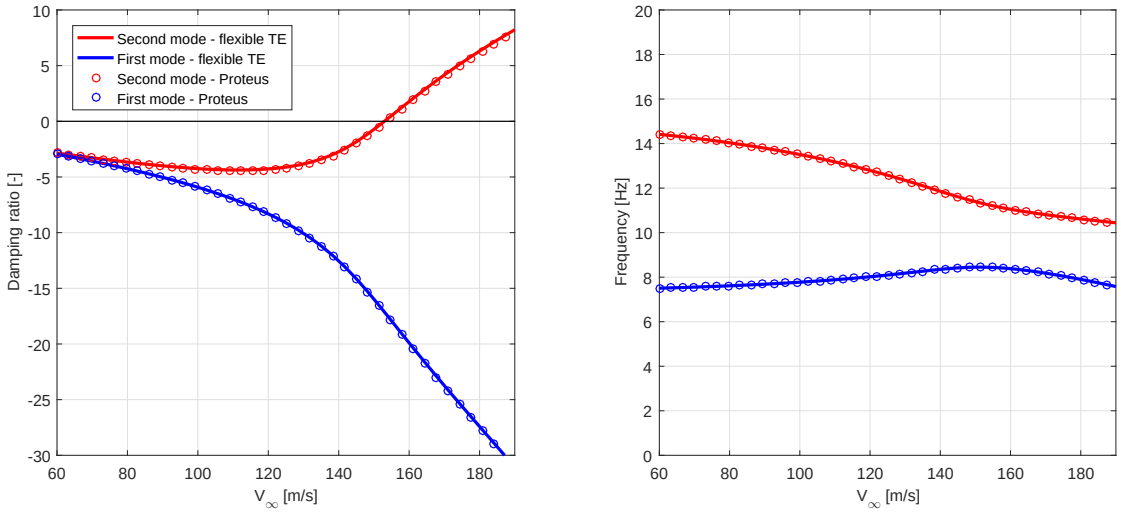

Figure 4.20: Flutter diagram of the Goland wing, using the PROTEUS model and the model with a flexible trailing edge

4.4.3. Spanwise instability

Aeroelastic modes with a number of structural waves in the span-wise direction appear to be unstable for all flow velocities. An example of this unstable mode is shown in Figure 4.21. This instability occurs for all trailing edge stiffnesses, masses and aspect ratios. A mesh convergency study has been done to check whether or not a finer mesh would be needed to avoid this instability. To investigate whether this instability occurs from a certain aspect ratio onwards, or is always present, a study of increasing the aspect ratio has also been done.

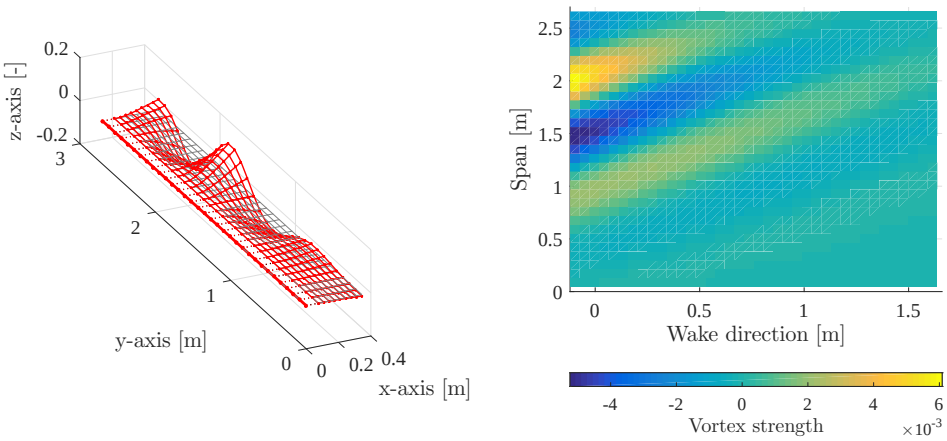

Figure 4.21: Spanwise instability of the trailing edge. This modeshape corresponds to the red line in Figure 4.22

Sorting the eigenvalue solely on damping ratio, the flutter diagram looks like the one shown in Figure 4.22, for all mesh density studied. Showing the results of the mesh convergency and aspect ratio study is not meaningful, as the flutter speed is zero for all mesh densities and aspect ratios considered.

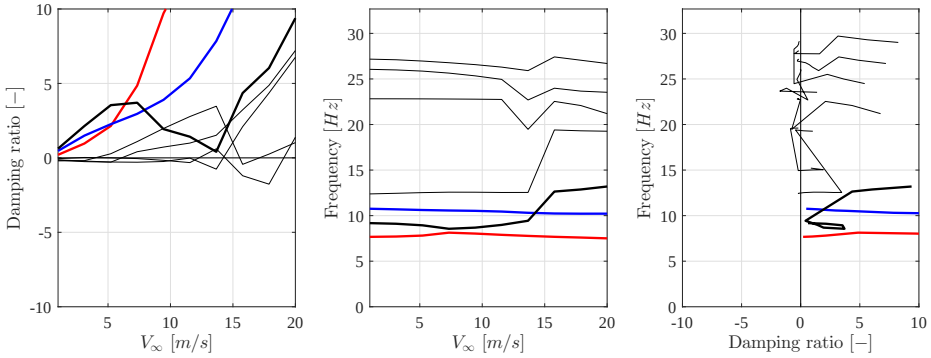

Figure 4.22: Flutter diagram of the aeroelastic system as shown in Figure 4.21

Cause

Since the instability occurs for all mesh densities, it is believed that it is not caused by a discretisation error. There are two other reasons to believe that the modes currently predicted by the model to be unstable, are not actually unstable in reality.

The first one is found in the literature. Although the large majority of plate flutter studies, with both potential flow methods and CFD models to represent the aerodynamics, use a two-dimensional structural representation by modelling the plate as a beam in chord-wise direction, one researcher has investigated it using a three-dimensional structure. Banerjee et al. (2015), modelled the aerodynamics with a Navier-Stokes model and the structure as a 3-dimensional membrane without bending rigidity. His conclusion is that a model with three-dimensional structural deformation is more stable than a 2-dimensional structure.

The second reason is that plate flutter experiments do not show this instability, and not due to the fact that their set-up does not allow any span-wise deformation. Watanabe (2002) did a study of paper flutter, considering plates of small and larger aspect ratio. Span-wise deformation was observed in their experiments, but the difference in the flutter speed of the small and large aspect ratio was small.

A cause for the instability in the present model has not been found yet. Because the current plate model of the trailing edge does not have material damping and the aerodynamic forces computed by the potential flow method act only in the $x-z$ - plane, currently the only explanation is that maybe span-wise waves are not damped, and become unstable as a result.
However, arguments that a higher fidelity model does not predict the current span-wise instabilities and that experiments in which span-wise deformations are present result in the expected flutter speeds, are convincing enough to discard these instabilities in the present study. Since determining the flutter speed depends on finding the most critical eigenvalue in a large set of aeroelastic eigenvalues, a practical solution has to be found to separate the real unstable modes from the spurious ones.

Practical solution

A practical solutions is to filter out the spurious unstable modes, by increasing the frequency of these modes. To increase only the frequency of the modes with waves in the span-wise direction, stiffeners in that direction are added to the trailing edge. Following the approach given by Kassapoglou (2010) about skin-stiffened structures, the stiffness properties of the stiffeners are smeared over the trailing edge structure. This results in an equivalent membrane and bending stiffness in the span-wise direction and leaves the chord-wise stiffness unchanged:

$$(A_{11})_{eq} \approx (A_{11})_{skin} \tag{4.48a}$$
$$(A_{12})_{eq} \approx (A_{12})_{skin} \tag{4.48b}$$
$$(A_{22})_{eq} \approx (A_{22})_{skin} + \frac{n_s (EA)_{stiff}}{b_s} \tag{4.48c}$$
$$(A_{66})_{eq} \approx (A_{66})_{skin} \tag{4.48d}$$
$$\tag{4.48e}$$

$$(D_{11})_{eq} \approx (D_{11})_{skin} \tag{4.49a}$$
$$(D_{12})_{eq} \approx (D_{12})_{skin} \tag{4.49b}$$
$$(D_{22})_{eq} \approx (D_{22})_{skin} + \frac{n_s (EI)_{stiff}}{b_s} \tag{4.49c}$$
$$(D_{66})_{eq} \approx (D_{66})_{skin} \tag{4.49d}$$
$$\tag{4.49e}$$

In the above equations, n_s is the number of stiffeners and b_s is the chord-wise length of the trailing edge over which the stiffeners are distributed. Note that the D_{66} term is not affected, since open-type stiffeners are used, for which the contribution of the polar moment of inertia is negligible.
The downside of adding directional stiffness in the span-wise direction is that tailoring the stiffness of the trailing edge in that direction has become irrelevant.

5
Design studies

The aeroelastic model of a 3D wing structure with a flexible trailing edge is now completed. In Chapter 2 and 3, the structural and aerodynamic model have been discussed, followed by an explanation of the coupled aeroelastic system in Chapter 4. This system has been verified using several reference studies, which now allows us to investigate the effect of the flexible trailing edge with confidence.

In this chapter, the effect of a flexible trailing edge on the aeroelastic characteristics is studied using a conventional wing configuration. The trailing edge properties and dimensions are then modified and its aeroelastic performance compared to the baseline conventional wing with a chord-wise rigid trailing edge.

First, the plan of investigation is presented in Section 5.1. Then the baseline wing configuration is discussed in Section 5.2, showing wing dimensions, wing box properties and the addition of stiffeners to the trailing edge to prevent span-wise instabilities to occur. Finally, the results, combined with a discussion, are presented in Section 5.3.

5.1. Plan of investigation

To assess the effects of a flexible trailing edge on the aeroelastic characteristics of a 3D wing structure, the following steps are taken:

1. The critical velocity is determined for a variation in chord-wise compliance of the trailing edge, keeping all other parameters of the wing constant. The trailing edge thickness is used as parameter to vary the stiffness of the trailing edge. Note that the stiffness will change in the whole trailing edge equally.
2. The critical velocity is determined for a variation in the chord-wise length of the flexible trailing edge, keeping all other parameters of the wing constant.
3. For the same trailing edge length as point 1, the benignity of airfoil flutter is computed for a variation of trailing edge thicknesses.
4. The critical velocity is determined for a span-wise variation of the chord-wise trailing edge stiffness:
    (a) By increasing the length of the flexible trailing edge region in span-wise direction.
    (b) By changing the position of the flexible trailing edge region of fixed width along the span.
5. Alternative configurations are studied:
    (a) By changing the torsional stiffness of the wing-box, it is investigated whether the effect of a flexible trailing edge can be generalised.

(b) A comparison is made between the trailing edge configuration from point 1 to a hinged rigid flap.

(c) A comparison is made between a chord-wise rigid wing, keeping the structural configuration constant, of which the trailing edge is omitted.

6. To determine the effect of a flexible trailing edge on the steady aerodynamic loads, a static aeroelastic analysis of the trailing edge from point 1 is done.

5.2. Baseline wing configuration

A wing without taper, sweep or dihedral has been chosen to get an undisturbed picture of the effects of a flexible trailing edge. The geometry of this wing is shown in Figure 5.1. The semi-span is 3.5 m, the chord length 0.5 m and the elastic axis and centre of gravity are positioned at 40 % of the chord. Note that the flexible trailing edge falls within the outer edges of this wing geometry, the total chord length of the wing is not increased by the flexible trailing edge.

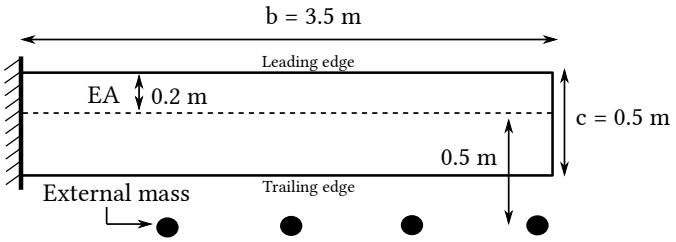

Figure 5.1: Schematic representation of the wing used during the investigations.

Table 5.1: Cross-sectional properties

Beam cross-sectional properties	
A	$1.746 \cdot 10^{-4} m^2$
EI_{22}	$1.081 \cdot 10^{4} m^2$
EI_{23}	0
EI_{33}	$3.506 \cdot 10^{5} m^2$
GJ	$1.087 \cdot 10^{4} m^2$
k	$5/6$
e_y	$0m$
e_z	$0m$

The properties of the wing-box are translated in cross-sectional stiffness properties of the beam elements, and are summarised in Table 5.1. External masses are added to the wing-box structure to destabilise the aeroelastic system. The location of these masses is shown in Figure 5.1. The 4 masses are positioned equally along the span, from 25 % up to the tip of the wing. Going from root to tip, the masses are: 0.1, 0.2, 0.3 and 0.4 kg. The position and size of the masses have been chosen such that the flutter speed of the baseline wing configuration is around 40 m/s.

A quasi-isotropic CFRP laminate is used for the trailing edge structure. A thickness variation of the entire laminate is managed by modifying the thickness of the individual plies. Naturally, ply thickness is not something which can be varied freely in case the trailing edge would be produced. But in this

study, the optimal trailing edge stiffness is determined, without looking at manufacturing constraints. The properties of the CFRP material is shown in Table 5.2. The layup of the quasi-isotropic laminate is defined as $[0_2/-45_2/45_2/90_2]_s$, of which the thickness of the individual plies is scaled such that a certain trailing edge thickness is obtained.

Table 5.2: Material properties of the quasi-isotropic laminate of the trailing edge.

E_1	127.6 GPa
E_2	13.0 GPa
ν_{12}	0.3 –
G_{12}	6.41 GPa
ρ	1520 kg/m^3

To filter out unstable trailing edge flutter modes with structural waves in the span-wise direction, stiffeners are added in the span-wise direction. They will modify the stiffness of the structure, by adding bending and torsional stiffness to the wing, even if the stiffness of the flexible trailing edge is very low. However, during the investigations, the stiffness added by the stiffeners to the wing will not vary and can therefore be seen as an addition to the wing box structure. In Figure 5.2, a schematic representation of these stiffeners are shown.

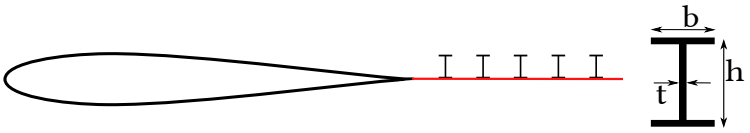

Figure 5.2: Schematic representation of the stiffeners which are added to the trailing edge.

Following the approach given by Kassapoglou (2010) about skin-stiffened structures, the stiffness properties of the stiffeners are smeared over the trailing edge structure. Five I-type stiffeners are distributed over the trailing edge, assuming that the stiffness increase due to these stiffeners is symmetric around the mid-plane of the trailing edge laminate. The contributions of the mass of these stiffeners to the total trailing edge mass is neglected.

Aeroelastic stability of the chord-wise rigid baseline wing configuration

The first three natural frequencies and eigenmodes of the chord-wise rigid structural model are shown in Figure 5.3. The branches in the flutter diagram of Figure 5.4, corresponding to these three eigenmodes are depicted in blue, red and black respectively. It can be seen that the branch corresponding to the first torsion eigenmode becomes unstable while interacting with the first bending mode of the wing.

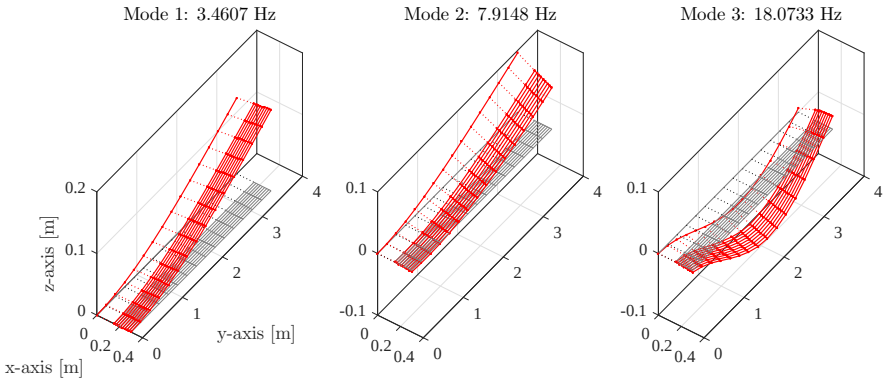

Figure 5.3: First 3 structural eigenmodes of the chord-wise rigid wing, using a trailing edge of 4 mm.

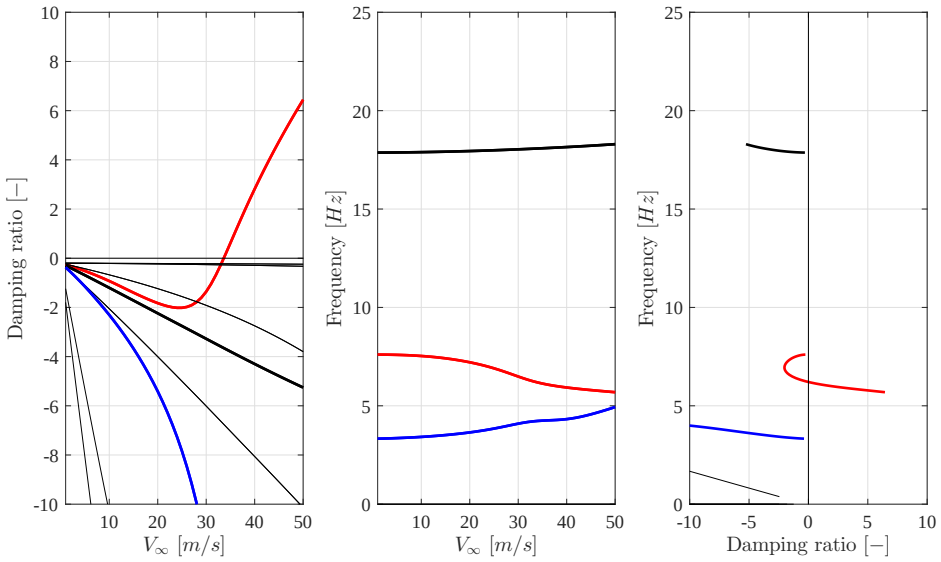

Figure 5.4: Flutter diagram of the chord-wise rigid wing, using a trailing edge of 4 mm.

The unstable aeroelastic eigenmode of this wing is shown in Figure 5.5.

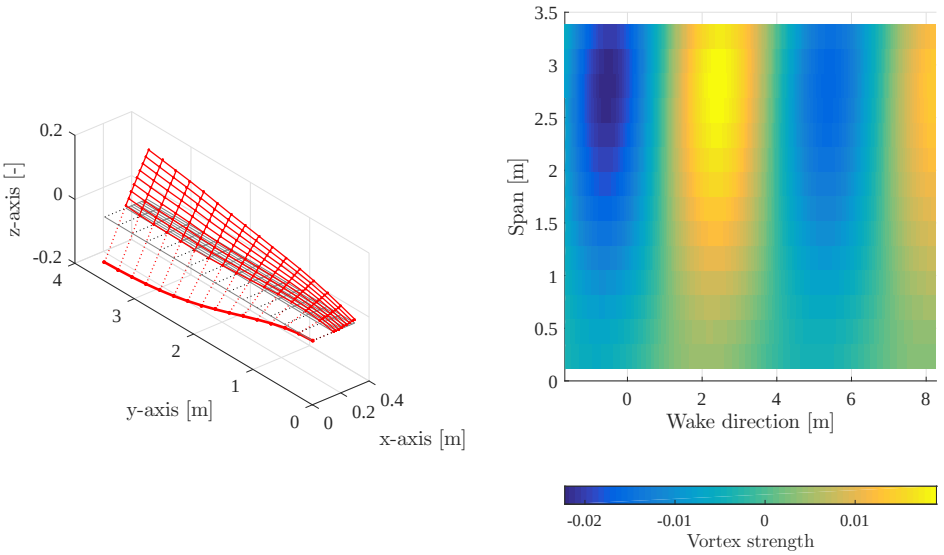

Figure 5.5: Flutter mode of the chord-wise rigid wing, using a trailing edge thickness of 4 mm.

5.3. Results and discussion

The cross-sectional properties of the wing-box and the stiffeners on the trailing edge will not be changed during the design studies. In the oncoming results, only the properties of the trailing edge will be varied.

5.3.1. Chord-wise thickness variation of the trailing edge

The first step is to see how a thickness variation of the entire trailing edge affects the stability of the aeroelastic system. In Figure 5.6 the critical velocity versus trailing edge thickness is presented for a wing with a flexible trailing edge of 30 % of the total chord length. It can be seen that if the trailing edge becomes thicker, it converges to a chord-wise rigid wing. For a decreasing thickness, the trailing edge becomes more compliant, resulting in an increase in the flutter speed, up until the point where plate flutter of the trailing edge becomes the critical instability. The thin black curve with circles shows how the airfoil flutter mode evolves in the region where plate flutter is the dominating instability. It can be seen that the flutter speed increase levels off around a thickness of 0.2 mm. Qualitatively, the results presented here match those published by Bergami and Gaunaa (2010), who also show an increase and leveling off, of the airfoil flutter speed with increasing trailing edge compliance. For this specific case, the flutter speed at the optimal trailing edge thickness is 13.93 % higher than a chord-wise rigid trailing edge. Note that for this wing configuration and trailing edge, the divergence instability mode always occurs at a higher velocity than the plate and airfoil flutter modes.

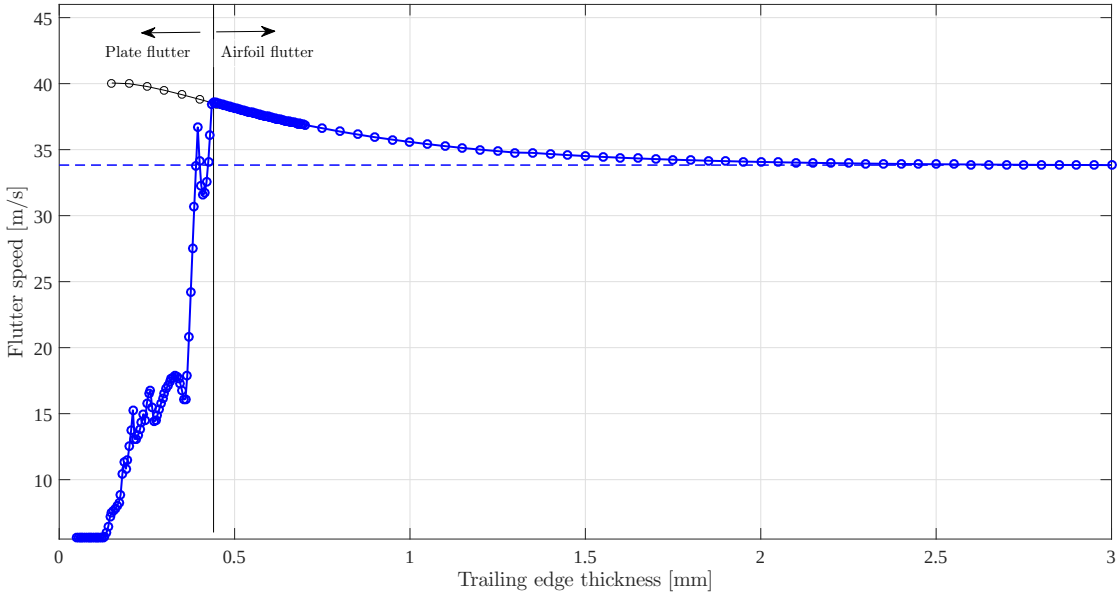

Figure 5.6: Flutter speed versus trailing edge thickness, for a flexible trailing edge of 30 % of the total chord length.

In the region where plate flutter is critical, the curve does not look smooth, but rather irregular. Therefore, the next figure shows this region in more detail. Figure 5.7, shows an enlarged picture of the flutter speed over trailing edge thickness in the plate flutter region.

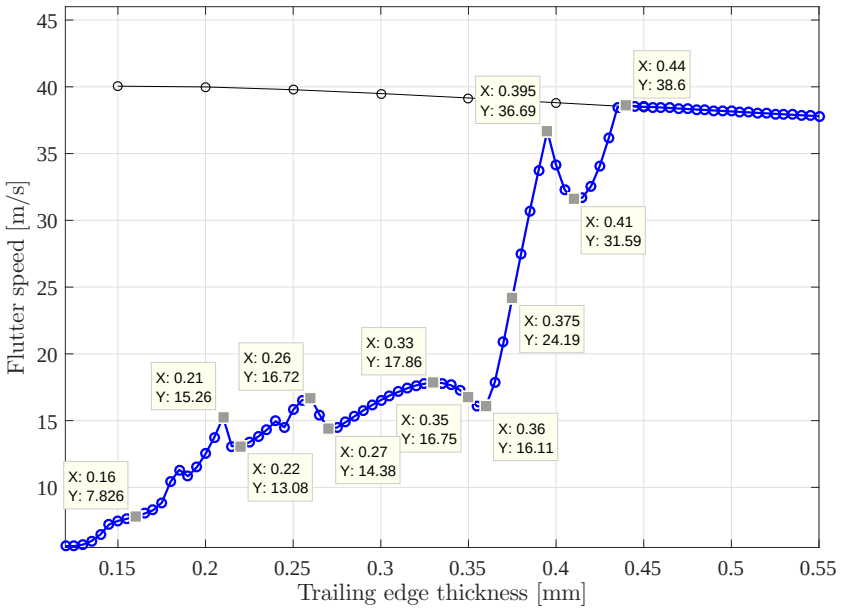

Figure 5.7: Region of plate flutter

The reason for the irregular plate flutter response is due to interaction with the span-wise deformation

of the beam. This can clearly be seen in the eigenmodes at different plate thicknesses. In Figure 5.8, a flutter diagram for a trailing edge thickness of 0.33 mm is shown.

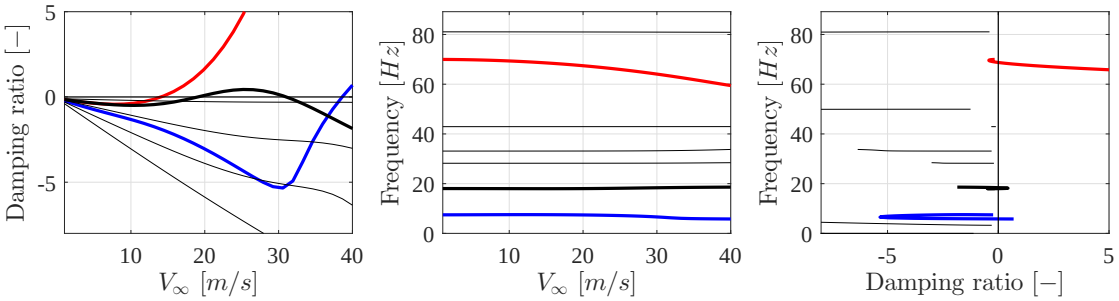

Figure 5.8: Flutter diagram at a trailing edge thickness of 0.33 mm.

The red line indicates the 2^{nd} chord-wise plate bending mode, which is the unstable plate flutter mode. The blue line indicates airfoil flutter and the black line indicates control surface flutter. All three eigenmodes are shown in Figures 5.9, 5.10 and 5.11:

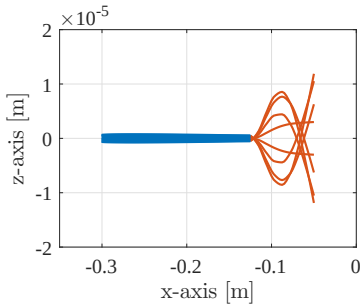

Figure 5.9: Eigenmode corresponding to red line

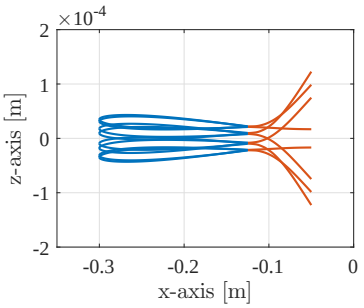

Figure 5.10: Eigenmode corresponding to black line

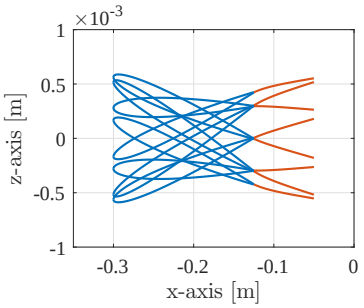

Figure 5.11: Eigenmode corresponding to blue line

To show how the flutter diagram evolves with trailing edge thickness, the damping versus velocity and root locus plots are shown for the airfoil flutter and plate flutter branch in Figures 5.12 and 5.13. The control surface flutter mode is not included since it is not a critical mode for any trailing edge thickness.

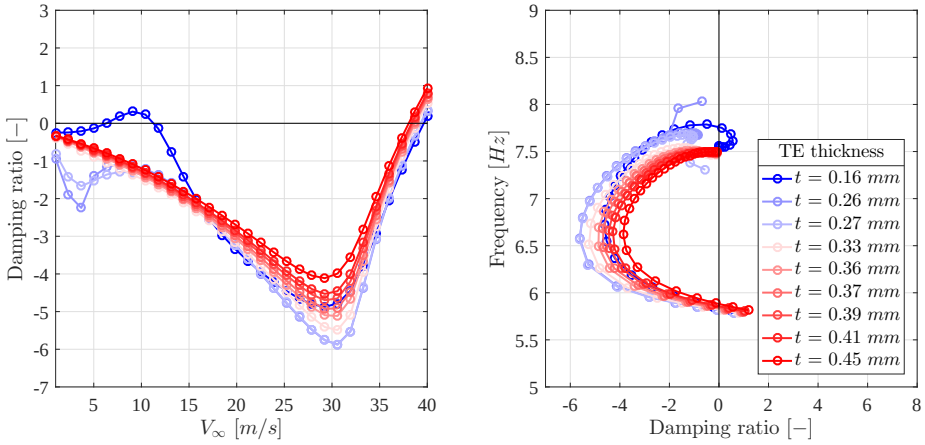

Figure 5.12: Evolution of the branch corresponding to airfoil flutter for different trailing edge thicknesses.

The airfoil flutter mode does not show any unusual behaviour. Simply a decrease in the flutter speed with increasing trailing edge thickness. At the lowest trailing edge thickness, it crosses the zero-damping line briefly at a low velocity before becoming stable again.

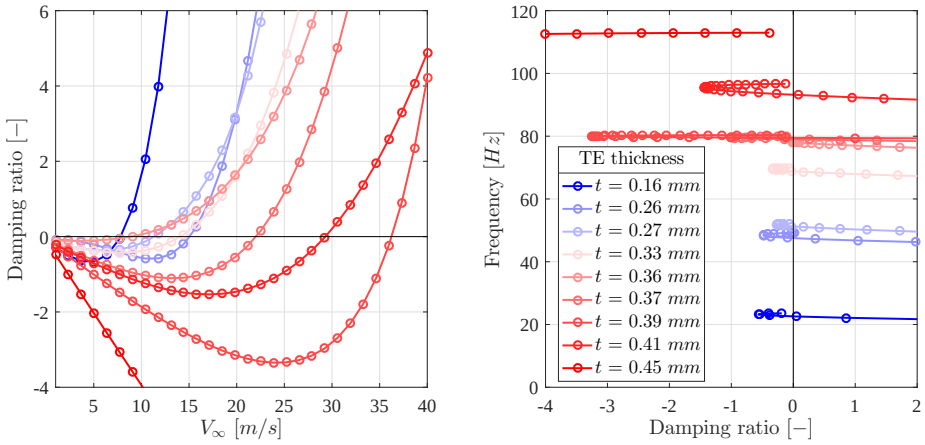

Figure 5.13: Evolution of the branch corresponding to plate flutter for different trailing edge thicknesses.

The plate flutter branches show more variation. As seen before in the flutter speed versus thickness plot, the flutter speed does not increase linearly with increased thickness, but moves up and down. An explanation for this behaviour is the interaction with the wing box span-wise deformation, which varies with changing trailing edge thickness. This can best be shown by the eigenmodes of trailing edge thicknesses of 0.375 mm, 0.39 mm and 0.41 mm, where a clear mode jump is visible in the flutter speed versus thickness plot of Figure 5.7. These eigenmodes are shown in Figures 5.14 through 5.16.

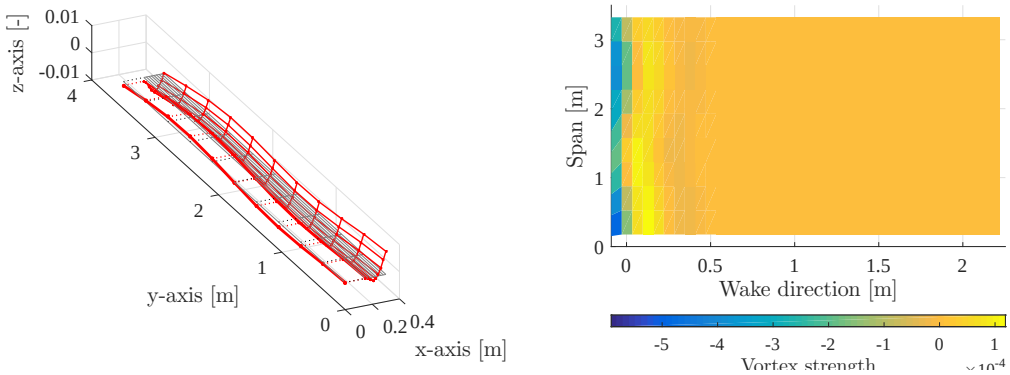

Figure 5.14: Eigenmode at the critical velocity for a trailing edge thickness of 0.375 mm.

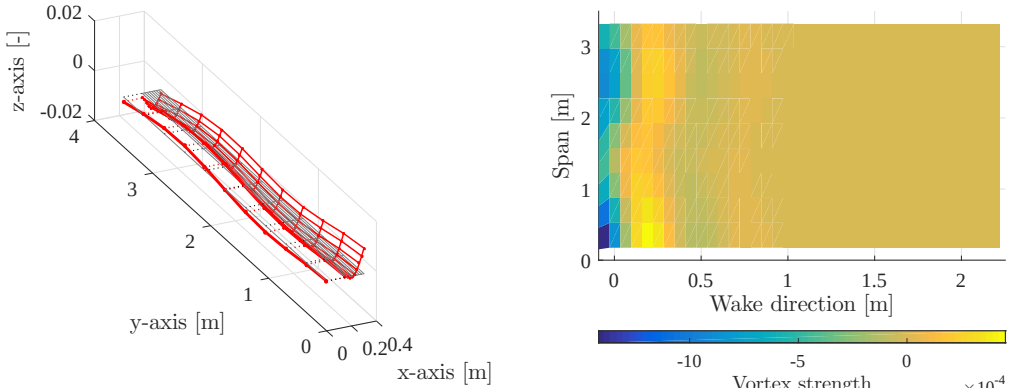

Figure 5.15: Eigenmode at the critical velocity for a trailing edge thickness of 0.39 mm.

In the eigenmodes corresponding to a thickness of 0.375 mm and 0.39 mm, the beam is vibrating in its 3^{rd} bending mode (around the x-axis). The beam deformation is small compared to the trailing edge deflection, but clearly present.

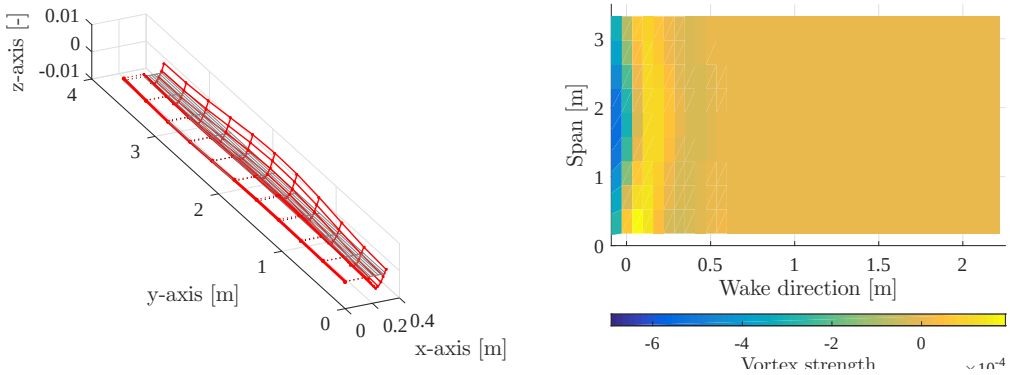

Figure 5.16: Eigenmode at the critical velocity for a trailing edge thickness of 0.41 mm.

It can be seen that the eigenmode of the wing with a trailing edge of 0.41 mm is different from the other

two. Although still 2^{nd} chord-wise plate bending in the trailing edge is present, the span-wise beam deflection is small compared to the other two.

Due to the presence of span-wise deformation, the region of plate flutter is not so smooth as in a two-dimensional case. However, the flutter speed does go up until a point where airfoil flutter is the critical flutter mode.

5.3.2. Chord-wise trailing edge length variation

Next, the variation of the length of the flexible trailing edge is investigated. In Figure 5.17, the flutter speed versus trailing edge thickness plot is shown for four different trailing edge lengths.

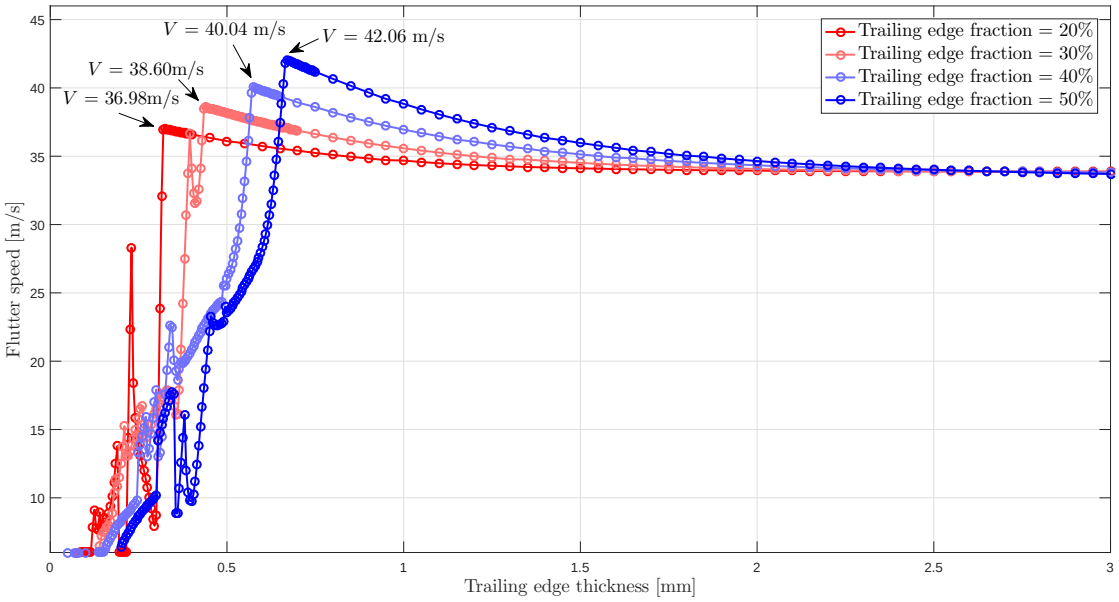

Figure 5.17: Flutter velocity versus trailing edge thickness for different fractions of flexible trailing edge. The maximum increase in flutter speed for the four different fractions are 9.15% 13.93%, 18.19% and 24.14% respectively for 20% to 50% respectively, compared to a chord-wise rigid airfoil.

For all trailing edge lengths, the plate flutter region shows bumps, corresponding to variations in the span-wise deformation of the wing. In general, it can be observed that longer trailing edges result in larger flutter speed increases. Naturally, the plate flutter regions becomes wider, since a longer trailing edge means that the trailing edge has to be stiffer to increase the plate flutter velocity.

5.3.3. Benignity

Drazumeric et al. (2014) conducted experiments with an airfoil with a flexible trailing edge and concluded that an airfoil with a flexible trailing edge showed a slower increase in pitch and plunge amplitude after the critical velocity was reached than a rigid airfoil. How slow or fast the amplitude increases after the critical velocity is reached is characterised by the benignity, which is defined as the inverse of the change in damping ratio with velocity, given by Equation (5.1). Higher benignity is favoured, because more time is available to react to flutter.

$$benignity = \left(\frac{\Delta Damping\ \ ratio}{\Delta V_\infty} \right)^{-1} \tag{5.1}$$

In Figures 5.18 and 5.19, the results of these experiments for a rigid and flexible airfoil can be seen.

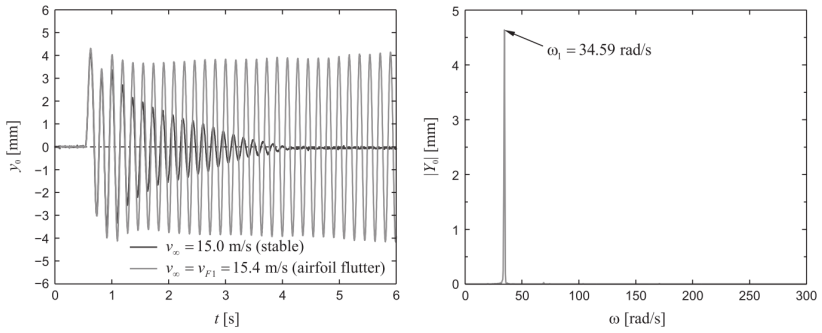

Figure 5.18: Amplitude response for a quasi-rigid airfoil, for a velocity just below and just above the flutter boundary. Drazumeric et al. (2014)

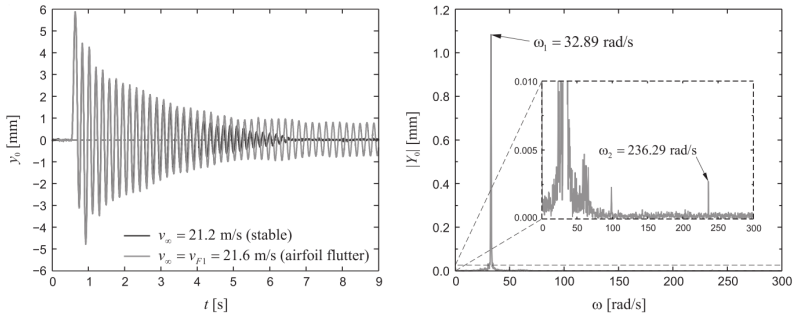

Figure 5.19: Amplitude response for an airfoil with a flexible trailing edge, for a velocity just below and just above the flutter boundary. Drazumeric et al. (2014)

For a wing with a flexible trailing edge of 30 % of the total chord length, the benignity as a function of the trailing edge thickness is investigated. In Figure 5.20, the benignity is plotted, and it can be seen that it hardly varies with increased trailing edge compliance. The difference between the benignity of a quasi chord-wise rigid trailing edge and that of a flexible trailing edge is 2.28 %. Considering the fact that the benignity does not level out for increasing trailing edge thicknesses, the reduction in benignity could also be due to a shift in the centre of gravity as the trailing edge becomes heavier.

Although the present wing configurations differs from the experiment conducted by Drazumeric et al. (2014), the discrepancy is large: a small increase in benignity using the present model, and a large increase shown by Figures 5.18 and 5.19. Naturally, with a longer flexible trailing edge, the increase in benignity will be larger, but this cannot explain everything. Two things could explain the discrepancy: the absence of material damping in the present model, and the fact that non-linear aerodynamic effects could become significant after the flutter speed is reached, and pitch and plunge amplitudes become larger.

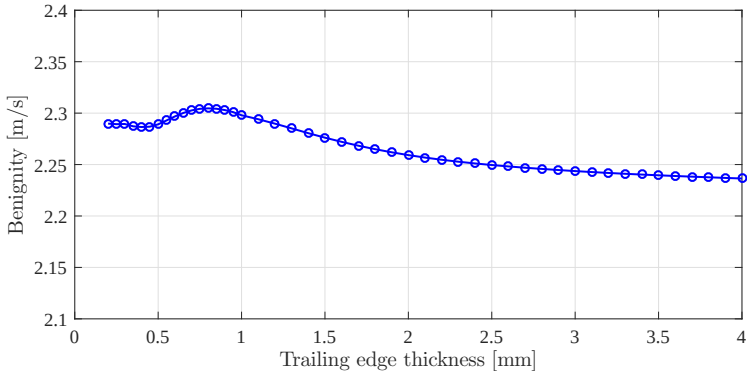

Figure 5.20: Benignity of the airfoil flutter mode versus the trailing edge thickness. Benignity is defined as the inverse of the change of damping ratio with velocity $\left(\frac{\Delta Damping\ ratio}{\Delta V_\infty}\right)^{-1}$.

5.3.4. Span-wise length and position variation

From the previous sections, it can be concluded that generally speaking, no big differences are found with the two-dimensional analyses done before. The present three-dimensional model allows to vary the properties of the trailing edge in span-wise direction. Note that the added stiffeners make it impossible to tailor the stiffness in the span-wise direction, but the chord-wise stiffness can be varied along the span. In Figure 5.21, it can be seen how the span-wise thickness variation is implemented. At the left side, the length variation is shown: starting with a trailing edge segment of a certain span-wise length at the root, then the length is increased until the entire trailing edge is flexible. The region outside the flexible segment has a thickness of 3 mm, to represent a chord-wise rigid trailing edge. Using the right side of Figure 5.21, the position variation of the flexible part can be explained: a trailing edge segment of a certain width is shifted along the span of the wing, keeping its width constant.

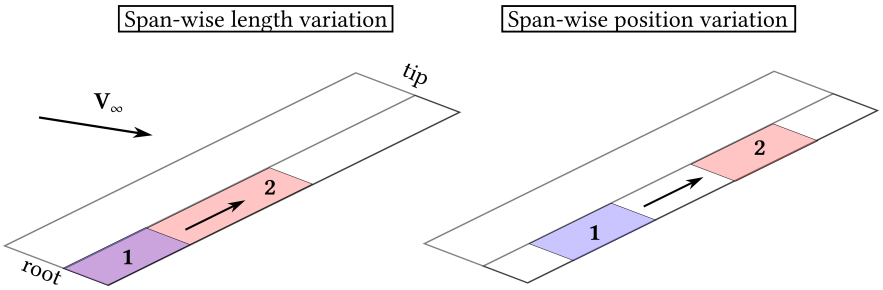

Figure 5.21: Schematic representation of the variation of the flexible trailing edge region. At the left side, a variation in the length of the regio is shown and at the right side, a variation in the position of the flexible region.

Translating a span-wise region of trailing edge flexibility into the aeroelastic model is done by reducing the thickness of the elements in this region, while keeping the elements in the rest of the trailing edge constant at a thickness of 3 mm. To make sure span-wise instabilities do not occur in the flexible region, the same number of stiffeners are added to this region. To allow the flexible segment to move freely, the stiffeners are removed in a line of elements in between the rigid an flexible region. In Figure 5.22, it can be seen that the flexible region can move independently from the rigid region.

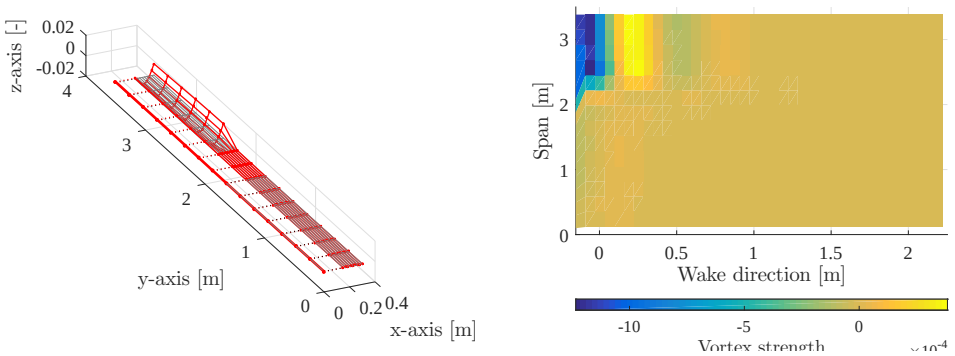

Figure 5.22: Eigenmode of the wing with a flexible trailing edge segment at the tip of the wing.

Showing the variation in trailing edge thickness of the different lengths of trailing edge segments, results in the curves depicted in Figure 5.23. The fraction indicated in the legend of the plot, originates from discretising the span of the wing in 15 structural elements and increasing the flexible trailing edge region in steps of 3 span-wise elements: 20 % means 3 elements at the root are flexible, 100 % means all the elements are flexible.

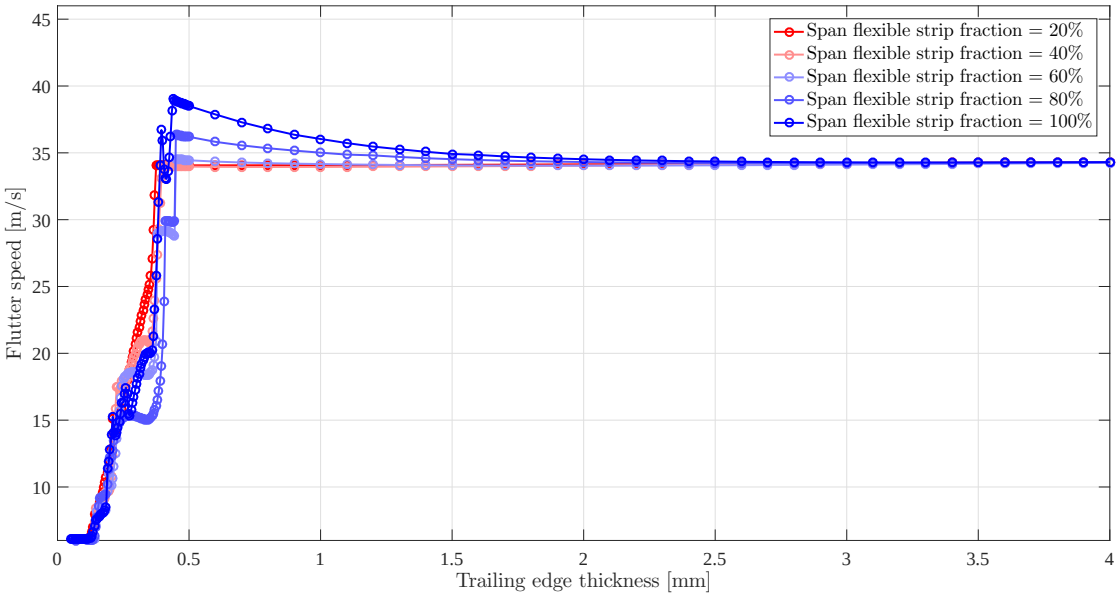

Figure 5.23: Flutter velocity versus trailing edge thickness for different trailing edge segment lengths.

Extracting the maximum flutter speed for each trailing edge segment length, and comparing it to the chord-wise rigid flutter speed, results in the plot shown in Figure 5.24. Figure 5.24 shows that increasing the trailing edge compliance only at the root has hardly, if any effect on the flutter speed.

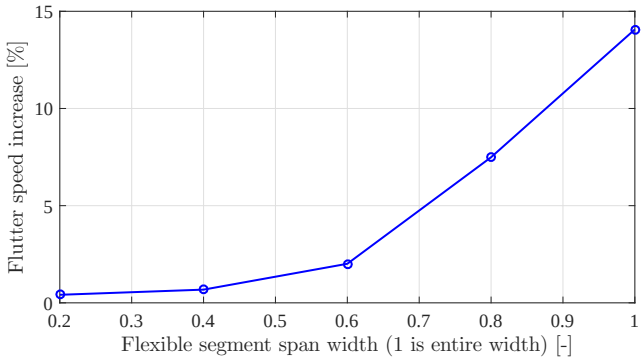

Figure 5.24: Flutter velocity versus span position.

Repeating the exercise for a variation in the position of a trailing edge segment of fixed width, yields the results shown in Figure 5.25, which indicates that positioning the flexible trailing edge segment at the tip has the largest effect.

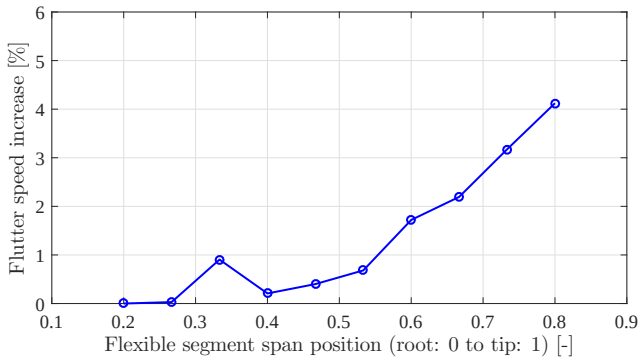

Figure 5.25: Flutter velocity versus span position.

Considering that the flexible trailing edge increases the flutter speed by changing the lift force and moment distribution, it makes sense that a tip segment is most effective. By changing forces at the tip, the bending moment in the wing is affected much more than by changing forces at the root.

5.3.5. Alternative configuration 1: wing box torsional stiffness variation

The torsional stiffness of the wing-box is varied. The current conventional wing configuration is changed by reducing the torsional stiffness of the beam elements. In Figure 5.26, the flutter speed of the chord-wise rigid wing and optimal flutter speed for a range of different torsional stiffness values can be seen. The x-axis of Figure 5.26 shows the GJ value divided by the GJ value of the baseline wing configuration.

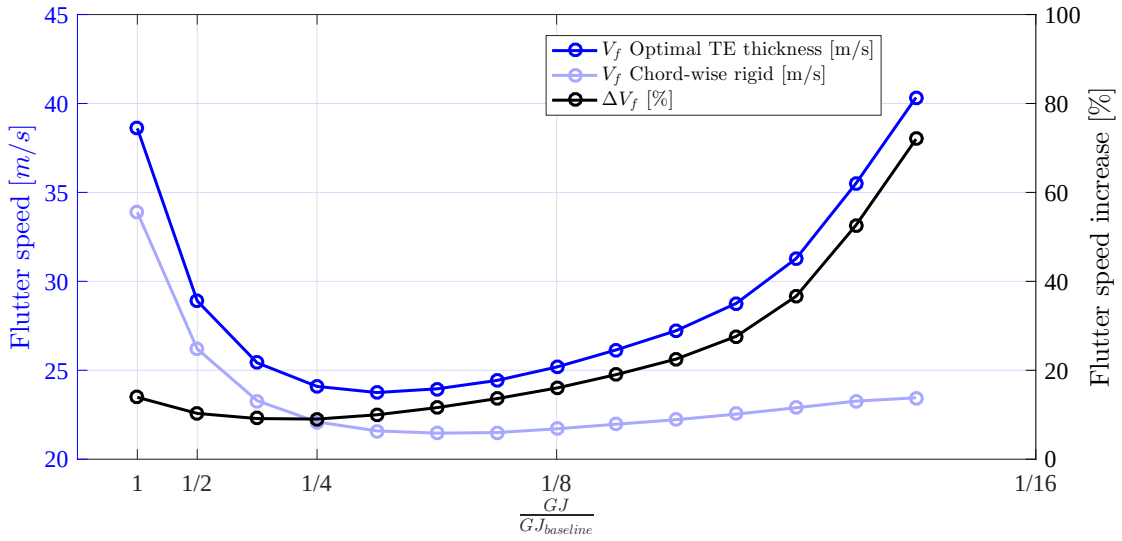

Figure 5.26: Flutter speed variation obtained when varying the torsional stiffness of the wing box. The x-axis shows the GJ value divided by the GJ value of the baseline wing configuration

It can be seen that initially, the flutter speed of the chord-wise rigid wing drops as the torsional stiffness decreases. This is due to the fact that the 1^{st} bending and 1^{st} torsional eigenfrequency come closer together, which reduces the flutter speed. After a minimum flutter speed is reached at a certain torsional stiffness, the flutter speed increases again. The increase is limited, because although the bending and torsional frequency move apart, the torsional stiffness keeps decreasing.

It is interesting to see that the flutter speed of the wing with a flexible trailing edge increases significantly when the torsional stiffness decreases. A maximum flutter speed increase of 71.98% compared to a chord-wise rigid wing is achieved for the minimum torsional stiffness.

5.3.6. Alternative configuration 2: comparison with a rigid hinged flap

Maximising the flutter speed of a wing with a flexible trailing edge is a trade-off between increasing the airfoil flutter speed by reducing the thickness of the trailing edge and making the trailing edge stiff enough such that plate flutter does not occur. In this light, the effect of a hinged flap is investigated. By reducing the thickness of the first row of elements of the trailing edge only, a rigid flap is modelled with a certain rotational spring at the hinge between the flap and the airfoil. A schematic is shown in Figure 5.27.

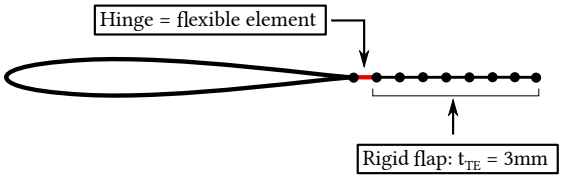

Figure 5.27: Schematic representation of the hinged trailing edge flap

In Figure 5.28, the results are shown and compared to the fully flexible trailing edge discussed in previous sections.

When reducing the thickness, going from the right to the left side of the plot, it can be seen that the flexible trailing edge (indicated in blue) shows a larger increase in flutter speed than the hinged rigid flap (indicated in red). However, for the flexible trailing edge, plate flutter becomes critical at a thickness of $0.44mm$. The thickness of the hinge element in the hinged rigid flap can be reduced further before it becomes unstable, and therefore the flutter speed can still be increased more using a hinged rigid flap. The reason that the thickness of the hinge element can be reduced to $0.32mm$ before becoming unstable, is that a hinged rigid flap does not suffer from plate flutter. On the other hand, it does suffer from control surface flutter, which is often a combination of span-wise bending and control surface deflection , or a combination of span-wise bending, torsion and control surface deflection Wright and Cooper (2007). The drop in flutter speed shown at a thickness of $0.32mm$ is due to control surface flutter.

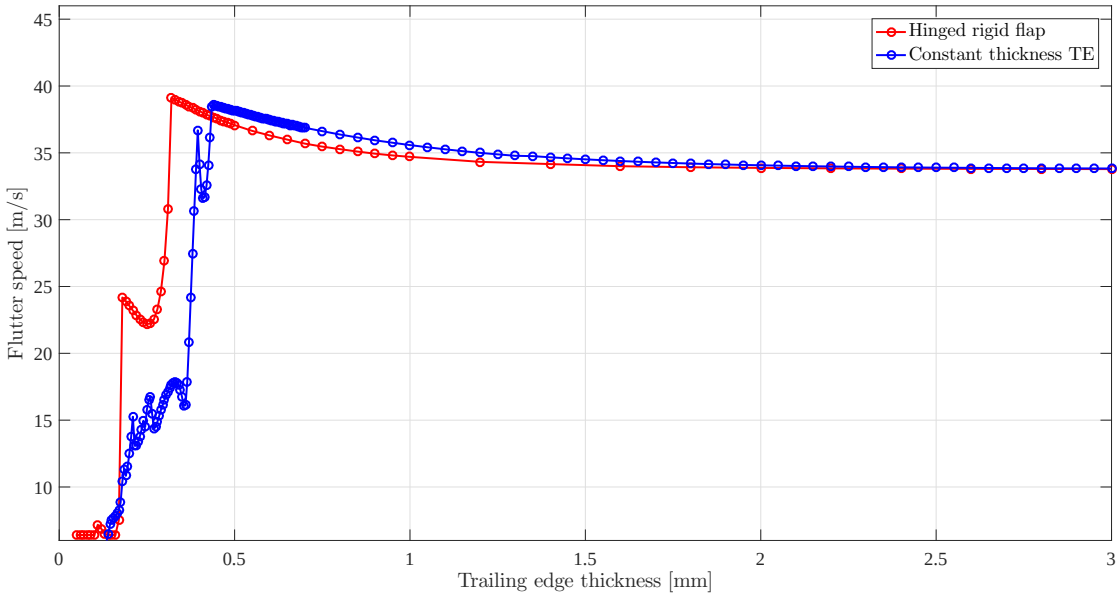

Figure 5.28: Flutter speed versus thickness for a hinged rigid trailing edge flap compared to a flexible trailing edge flap.

The flutter diagram for a hinge element thickness of $0.25\ mm$ is shown in Figure 5.29, in which the branch corresponding to control surface flutter is indicated in red. The eigenmodes of this branch are shown in Figures 5.30 and 5.31 in two- and three-dimensional view respectively.

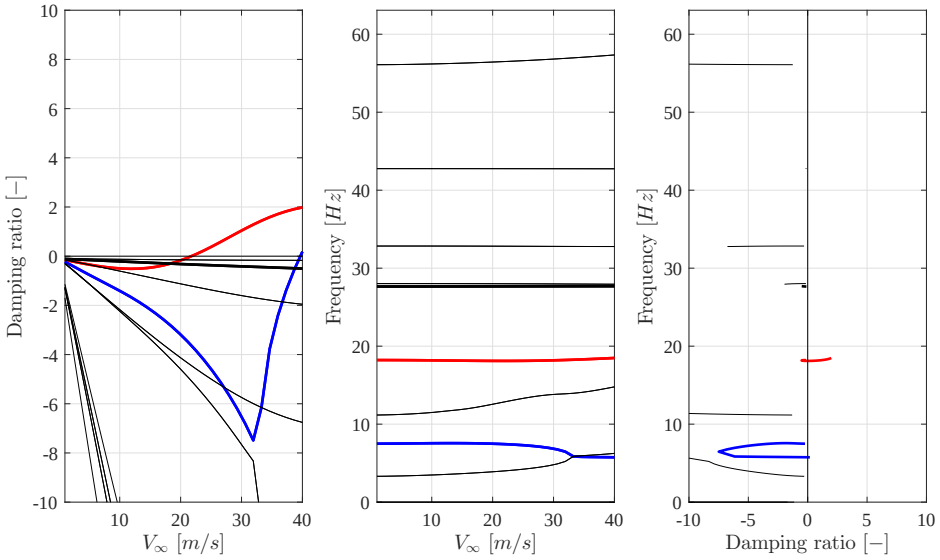

Figure 5.29: Flutter diagram of wing with the hinged rigid flap, for a hinge element thickness of 0.25 mm.

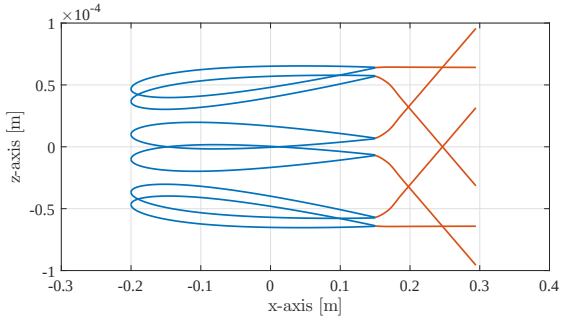

Figure 5.30: Two-dimensional eigenmode of the wing with the hinged rigid flap, for a hinge element thickness of 0.25 mm, just above the critical velocity.

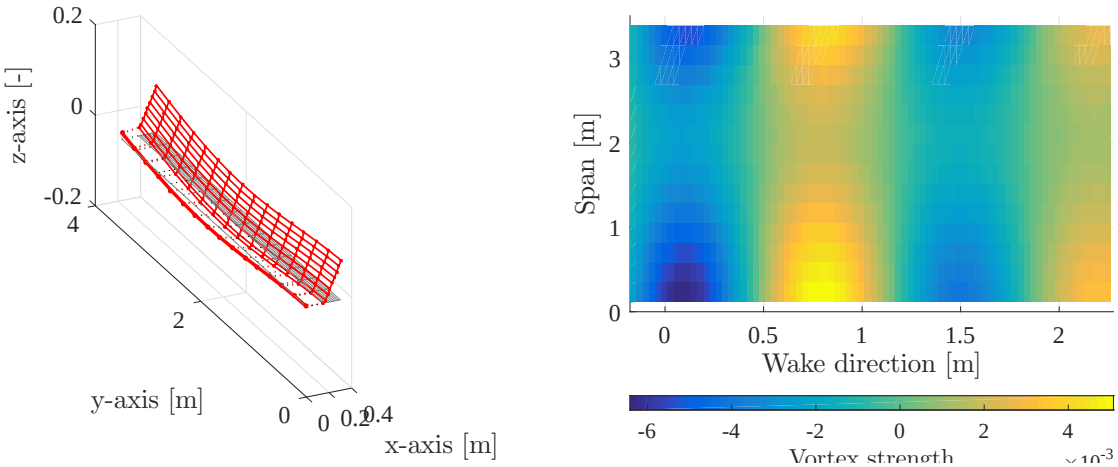

Figure 5.31: Three-dimensional eigenmode of the wing with the hinged rigid flap, for a hinge element thickness of 0.25 mm, just above the critical velocity.

5.3.7. Alternative configuration 3: comparison with a chord-wise rigid wing of shorter chord length

In all the investigations previously done, part of the chord was made compliant and it was concluded that this leads to an increase in flutter speed compared to a chord-wise rigid wing. It is interesting to determine whether this increase can also be seen by adding a flexible trailing edge to a wing, by making the total chord length longer. To investigate this, a wing with a chord length of 70 % of the original wing configuration is analysed, keeping the structural properties constant. This boils down to a wing of which the trailing edge is omitted. The flutter diagram of this chord-wise rigid wing is shown in Figure 5.32.

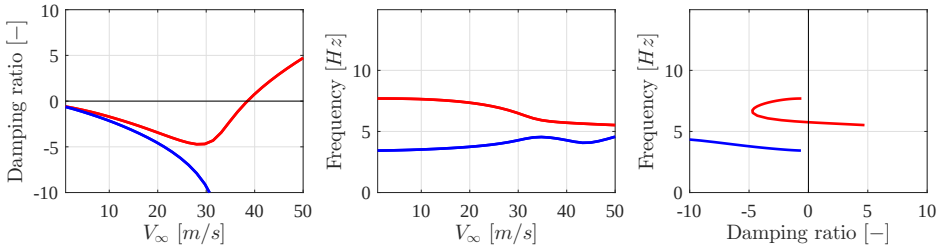

Figure 5.32: Flutter diagram of a chord-wise rigid wing with a chord length of 70 % of that of the original wing.

From the flutter diagram, it can be found that flutter speed of this wing is 38.51 m/s. Now consider that adding a flexible trailing edge to this wing would lead to the wing configuration studied in Section 5.3.1 with a flexible trailing edge of 30 % of the chord length, which showed a maximum flutter speed of 38.60 m/s, it can be concluded that it would not help to extend the wing with a flexible trailing edge.

5.3.8. Effect on steady aerodynamics

Increasing the compliance of the trailing edge in chord-wise direction is clearly beneficial for the dynamic aeroelastic behaviour. At this moment, the flexible trailing edge improves the flutter speed passively and cannot be turned on and off. It is therefore interesting to see how it affects the aircraft performance during (normal) flight conditions. The influence on the steady aerodynamic forces is in-

vestigated in this section. The effect on the aerodynamic drag will not be studied.
The steady forces are studied for the same wing as used for the dynamic analyses, using a trailing edge of 30 % of the chord length. The lift and moment coefficients C_L and C_M are computed for varying trailing edge thicknesses, using the same quasi-isotropic laminate. The flow velocity is 38.6 m/s, the maximum flutter speed achieved in the range of trailing edge thicknesses. The angle of attack α_0 is 5°. The results are shown in Figure 5.33. In Figure 5.34, the wing and trailing edge deformation under the given angle of attack and flow velocity are shown.

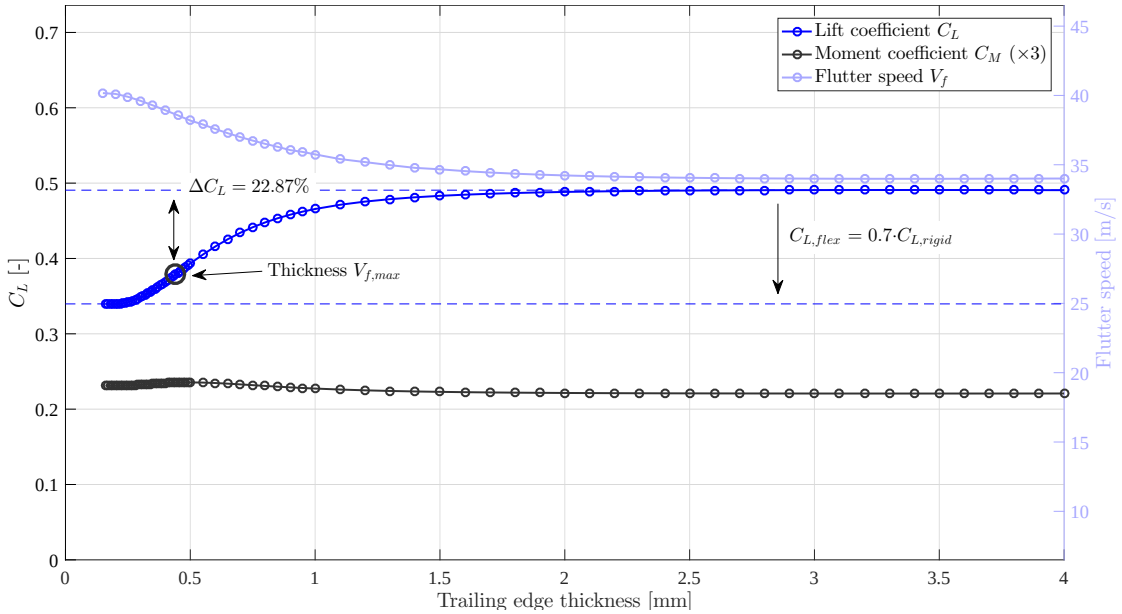

Figure 5.33: Steady lift coefficient C_L versus trailing edge thickness for flexible trailing edge fraction of 30%, under an angle of attack $\alpha_0 = 5°$. For an increasing trailing edge thickness, the lift coefficient converges to a chord-wise rigid wing. At the other extreme, the lift coefficient reduces such that the lift generated is equal to a chord-wise rigid wing of which the chord length is only 70% of that of the original wing. It can be observed that the increase of the flutter speed has a similar trend as the reduction in lift generated by the wing.

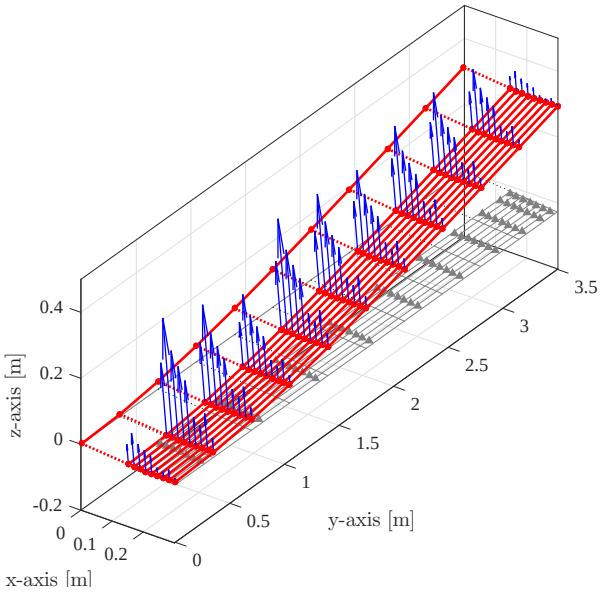

Figure 5.34: Static deformation of the wing under an angle of attack $\alpha_0 = 5°$.

Looking at the evolution of the lift coefficient for a variation of trailing edge thicknesses, several things can be observed. For a quasi-rigid trailing edge ($t_{TE} = 4mm$), the lift coefficient converges to a chord-wise rigid wing, and when the trailing edge becomes very thin, the lift coefficient converges to one corresponding to a wing of which the chord length is 70% of the length of the original wing. In other words, as if the wing would be cut-off at the point where the trailing edge starts. This means that improving the flutter speed by increasing the trailing edge compliance comes at a cost: a reduction in steady lift. Interestingly, the trend of the flutter speed curve is very similar to that of the steady lift coefficient. It starts increasing when the lift coefficient starts reducing and it levels off when the steady lift coefficient curve starts to level off.
The moment coefficient increases slightly with increased trailing edge compliance. For this particular wing, the elastic axis is at 40% of the chord, therefore an aerodynamic moment is present around this reference axis. When the trailing edge becomes more flexible, the aerodynamic centre shifts forward, away from the elastic axis, and therefore increasing the moment arm. On the other hand, the resultant lift force reduces as the trailing edge thickness reduces. The combination of these two factors partially cancel each other out, but still cause a slight increase of the moment coefficient.

To generate the same amount of lift with a wing with flexible trailing edge, the angle of attack needs to be larger than its chord-wise rigid counterpart. In Figure 5.35, it can be seen how large the difference in angle of attack to obtain a certain lift coefficient is. The interesting thing is that unlike an airfoil with a certain amount of camber, the lift coefficient is zero at an angle of attack $\alpha_0 = 0°$, and does not have an offset in C_L. The slope of the $\alpha - C_L$ - curve of the airfoil with flexible trailing edge is less steep than the chord-wise rigid wing, but still linear.

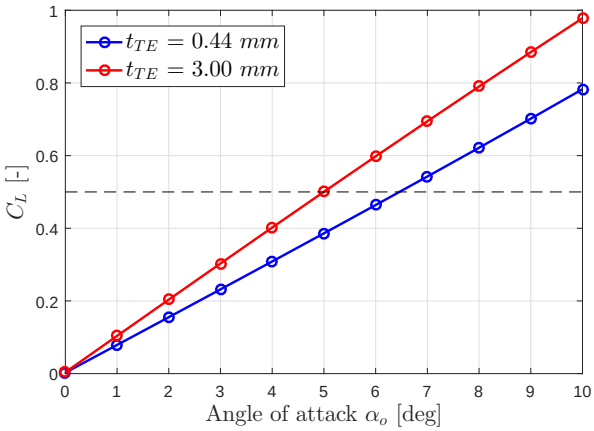

Figure 5.35: Lift coefficient C_L versus angle of attack α_0 plot for a the trailing edge thickness of maximum flutter speed versus a quasi-rigid trailing edge.

6
Conclusions and recommendations

The research question of this thesis was: *"To what extent can the aeroelastic characteristics of a 3D wing structure be improved by making its trailing edge flexible, and varying its properties along the span of the wing?"* In which the term aeroelastic characteristics have the following meaning:

- The velocity at which the aeroelastic system becomes unstable due to airfoil flutter, divergence or plate flutter.
- The benignity of the airfoil flutter response: how rapidly the amplitude of the wing motion increases after the critical velocity has been reached.
- The steady aerodynamic loads on the wing structure.

With this in mind, the following conclusions and recommendations are presented.

6.1. Conclusions

Similar to two-dimensional studies, the flutter velocity of a 3D wing structure increases with a reduction in trailing edge stiffness. Although the size of the flutter speed increase depends on the wing configuration and therefore can only be determined on a case by case basis, the parameter study conducted in this research showed a flutter speed increase in the range of 9.15 % to 24.14 % for trailing edge lengths of 20 % to 50 % of the total chord length.

The optimal flutter speed is found by using a trailing edge stiffness where both airfoil and plate flutter occur at the same time. If the stiffness is too low, plate flutter is the critical instability and when the stiffness is higher than the optimal stiffness, airfoil flutter is the critical instability.

Compared to a two-dimensional analysis, the region in which plate flutter occurs is qualitatively different. In a 2D analysis, the flutter speed increases approximately linearly with increased thickness, but in a 3D analysis, the flutter diagram shows mode jumps caused by interaction with the span-wise deformation of the wing-box structure.

If only part of the wing in span-wise direction is equipped with a flexible trailing edge, the flutter speed can be increased more effectively by positioning a flexible segment towards the tip of the wing. Increased flexibility in the trailing edge at the root of the wing has almost no effect on the flutter speed.

Benignity of airfoil flutter is only marginally affected by a flexible trailing edge: a small improvement of 2.28 % has been computed in the present investigation.

Extending the surface of the wing in chord-wise direction with a flexible trailing edge will not improve the flutter speed of the wing structure. It is found that the flutter speed of a wing at an optimal trailing edge stiffness is approximately the same as a wing of which that trailing edge is omitted.

The steady aerodynamic loads decrease proportionally to an increase in flutter speed as the trailing edge stiffness reduces. In the extreme case where the trailing edge stiffness is close to zero, the steady lift generated by such a wing is the same as that of a wing of which the trailing edge is omitted altogether. The steady aerodynamic moment around the elastic axis of the wing increases slightly since the aerodynamic centre shifts forward.

The flexible trailing edge does not perform better than a rigid hinged flap with a certain spring stiffness in the hinge. Rigid flaps do not suffer from plate flutter, which limits the potential flutter speed increase of a flexible trailing edge. In case the spring stiffness is too low, control surface flutter occurs. But even with a spring stiffness high enough to prevent control surface flutter, the flutter speed increase is higher than that of a flexible trailing edge.

6.2. Recommendations

The present aeroelastic system resulted in a relatively ill-conditioned state matrix, most likely as a consequence of the large difference in stiffness between beam and plate elements. The computation of an inverse of an ill-conditioned matrix results in significant numerical errors, which was observed in the aeroelastic eigenvalues in case large beam stiffnesses were used compared to the trailing edge stiffness. One of the consequences was that time-integration of the entire state-space system was numerically unstable and the gust response could not be analysed. More research is needed to determine what the exact cause of the ill-conditioning is such that this problem can be solved.

Eigenmodes of plate flutter with waves in the span-wise direction of the trailing edge were unstable for all flow velocities. Although plate flutter of three-dimensional structures is not covered abundantly in literature, with only one reference available, in combination with experimental observations the author is convinced that the instabilities in the current model are spurious. It would be interesting to know whether this is due to the combination of a 3D structure and the potential flow theory as aerodynamic model.

The flutter speed can only be increased a limited amount with a passive flexible trailing edge, at the same time resulting in a reduction of the steady lift generated by such a wing. A large step forward could therefore be made by actively controlling the trailing edge deformation.

The current model of the flexible trailing edge is integrated into the PROTEUS model and it is therefore harder to update the PROTEUS and the flexible trailing edge model independently. A modular approach would be preferable, in which the Matlab code for the flexible trailing edge model works as a completely independent add-on to the PROTEUS code.

Due to unforeseen problems and time constraints, a simple wing geometry without sweep, taper, dihedral and twist has been studied. The present model should have capabilities to model such a wing, although the aeroelastic model has only been verified for simple geometries. It would be interesting to use the present model to analyse different wing geometries to determine how a flexible trailing edge affects these types of wings.

Bibliography

Andersen, P. B., M. Gaunaa, C. Bak, and T. Buhl (2006). "Load alleviation on wind turbine blades using variable airfoil geometry". In: *European Wind Energy Conference and Exhibition*. DOI: 10.1260/0309524054797122 (cit. on p. 4).

Arrieta, A. F., I. K. Kuder, M. Rist, T. Waeber, and P. Ermanni (2014). "Passive load alleviation aerofoil concept with variable stiffness multi-stable composites". In: *Composite Structures* 116, pp. 235–242. DOI: 10.1016/j.compstruct.2014.05.016 (cit. on p. 4).

Attar, P. J., E. H. Dowell, and D. M. Tang (2003). "A theoretical and experimental investigation of the effects of a steady angle of attack on the nonlinear flutter of a delta wing plate model". In: *Journal of Fluids and Structures* 17.2, pp. 243–259. DOI: 10.1016/S0889-9746(02)00123-8 (cit. on p. 3).

Attar, P. J., E. H. Dowell, and J. R. White (2005). "Modeling Delta Wing Limit-Cycle Oscillations Using a High-Fidelity Structural Model". In: *Journal of Aircraft* 42.5, pp. 1209–1217. DOI: 10.2514/1.11325 (cit. on p. 3).

Banerjee, S., B. S. H. Connell, and D. K. P. Yue (2015). "Three-dimensional effects on flag flapping dynamics". In: 783, pp. 103–136. DOI: 10.1017/jfm.2015.516 (cit. on pp. 3, 62).

Basualdo, S. (2005). "Load alleviation on wind turbine blades using variable airfoil geometry". In: *Wind Engineering* 29.2, pp. 169–182. DOI: 10.1260/0309524054797122 (cit. on p. 4).

Beckert, A. and H. Wendland (2001). "Multivariate interpolation for fluid-structure-interaction problems using radial basis functions". In: *Aerospace Science and Technology* 5.2, pp. 125–134. DOI: 10.1016/S1270-9638(00)01087-7 (cit. on p. 44).

Bergami, L. and M. Gaunaa (2010). "Stability investigation of an airfoil section with active flap control". In: *Wind Energy* 13.2-3, pp. 151–166. DOI: 10.1002/we.354 (cit. on pp. 2, 69).

Buhl, T., M. Gaunaa, and C. Bak (2005). "Potential Load Reduction Using Airfoils with Variable Trailing Edge Geometry". In: *Journal of Solar Energy Engineering* 127.4, p. 503. DOI: 10.1115/1.2037094 (cit. on p. 4).

Cook, R. D. (1986). "On the allman triangle and a related quadrilateral element". In: *Computers & Structures* 22.6, pp. 1065–1067. DOI: 10.1016/0045-7949(86)90167-7 (cit. on pp. 16, 30).

Cook, R. D. and H. Saunders (1984). *Concepts and Applications of Finite Element Analysis (2nd Edition)*. Vol. 106, p. 127. DOI: 10.1115/1.3264300 (cit. on pp. 13, 16, 26).

Dassault Systèmes (2014). *Abaqus documentation* (cit. on p. 27).

De Boer, A., A. H. van Zuijlen, and H. Bijl (2007). "Review of coupling methods for non-matching meshes". In: *Computer Methods in Applied Mechanics and Engineering* 196.8, pp. 1515–1525. DOI: 10.1016/j.cma.2006.03.017 (cit. on p. 43).

De Breuker, R., M. M. Abdalla, and Z. Gürdal (2008). "Flutter of Partially Rigid Cantilevered Two-Dimensional Plates in Axial Flow". In: *AIAA Journal* 46.4, pp. 936–946. DOI: 10.2514/1.31887 (cit. on pp. 1, 3).

Drazumeric, R., B. Gjerek, and F. Kosel (2014). "Aeroelastic Characteristic of an Airfoil Containing Laminated Composite Plate". In: *55th AIAA/ASMe/ASCE/AHS/SC Structures, Structural Dynamics, and Materials Conference*. January, pp. 1–15. DOI: 10.2514/6.2014-1196 (cit. on pp. 1, 2, 74, 75).

Eloy, C., C. Souilliez, and L. Schouveiler (2007). "Flutter of a rectangular plate". In: *Journal of Fluid and Structure* 23.6, pp. 904–919. DOI: http://dx.doi.org/10.1016/j.jfluidstructs.2007.02.002 (cit. on p. 3).

Ferede, E. A. and M. M. Abdalla (2014). "Cross-sectional modelling of thin-walled composite beams". In: *55th AIAA/ASME/ASCE/AHS/ASC Structures, Structural Dynamics, and Materials Conference*. January. DOI: 10.2514/6.2014-0163 (cit. on p. 10).

Goland, M. (1945). "The flutter of a uniform cantilever wing". In: *Journal of Applied Mechanics* 12, A–197 –A–208 (cit. on p. 60).

Huang, L. (1995). "Futter of cantilevered plates in axial flow". In: *Journal of Fluids and Structures* 9, pp. 127–147. DOI: 10.1006/jfls.1995.1007 (cit. on p. 3).

Ibrahimbegovic, A (1990). "A robust quadrilateral membrane finite element with drilling degrees of freedom". In: *International Journal for Numerical Methods in Engineering* 30.August 1989, pp. 445–457. DOI: 10.1002/nme.1620300305 (cit. on p. 30).

Iura, M. and S. N. Atluri (1992). "Formulation of a membrane finite element with drilling degrees of freedom". In: *Computational Mechanics* 9.6, pp. 417–428. DOI: 10.1007/BF00364007 (cit. on p. 30).

Kassapoglou, C. (2010). *Design and Analysis of Composite Structures*, p. 300. DOI: 10.1002/9780470972700 (cit. on pp. 63, 67, 93).

Kim, S. H. and I. Lee (1996). "Aeroelastic Analysis Of A Flexible Airfoil With A Freeplay Non-Linearity". In: *Journal of Sound and Vibration* 193.4, pp. 823–846. DOI: 10.1006/jsvi.1996.0317 (cit. on p. 2).

Kornecki, A., E. H. Dowell, and J. O'Brien (1976). "On the aeroelastic instability of two-dimensional panels in uniform incompressible flow". In: *Journal of Sound and Vibration* 47.2, pp. 163–178. DOI: 10.1016/0022-460X(76)90715-X (cit. on pp. 2, 3).

Lambie, B., M. Jain, and C. Tropea (2011). "Passive Camber Change for Windturbine Load Alleviation". In: *AIAA Aerospace Sciences Meeting* 49. DOI: 10.2514/6.2011-637 (cit. on p. 4).

MacNeal, R. H. and R. L. Harder (1988). "A refined four-noded membrane element with rotational degrees of freedom". In: *Computational Structures* 28.1, pp. 75–84. DOI: doi.org/10.1016/0045-7949(88)90094-6 (cit. on p. 30).

Ming, P A N Guang and L U O Song Fa (1987). "A New Element Used in the Non-Orthogonal Boundary Plate Bending Theory - An Arbitrarily Quadrilateral Element". In: *International Journal for Numerical Methods in Engineering* 24, pp. 1031–1042. DOI: 10.1002/nme.1620240602 (cit. on p. 19).

Murua, J., R. Palacios, and J. Peiró (2010). "Camber effects in the dynamic aeroelasticity of compliant airfoils". In: *Journal of Fluids and Structures* 26.4, pp. 527–543. DOI: 10.1016/j.jfluidstructs.2010.01.009 (cit. on p. 2).

Ogata, K. (2010). *Modern Control Engineering*. Fifth Edit. Prentice Hall, p. 1013 (cit. on p. 26).

Shayo, L. K. (1980). "The stability of cantilever panels in uniform incompressible flow". In: *Journal of Sound and Vibration* 68.3, pp. 341–350. DOI: 10.1016/0022-460X(80)90391-0 (cit. on pp. 2, 3).

Tang, D. and E. H. Dowell (2002). "Limit cycle oscillations of two-dimensional panels in low subsonic flow". In: *International Journal of Non-Linear Mechanics* 37, pp. 1199–1209. DOI: 10.1016/S0020-7462(01)00140-8 (cit. on p. 3).

Tang, D., J. K. Henry, and E. H. Dowell (1999a). "Limit cycle oscillations of a cantilevered wing in low subsonic flow". In: *AIAA Journal* 37.3, pp. 1355–1362. DOI: 10.2514/3.14330 (cit. on pp. 3, 4, 58–60).

— (1999b). "Limit cycle oscillations of delta wing models in low subsonic flow". In: *AIAA Journal* 37.11, pp. 1355–1362. DOI: 10.2514/3.14330 (cit. on pp. 3, 4).

Tang, D., H. Yamamoto, and E. H. Dowell (2003). "Flutter and limit cycle oscillations of two-dimensional panels in three-dimensional axial flow". In: *Journal of Fluids and Structures* 17, pp. 225–242. DOI: 10.1016/S0889-9746(02)00121-4 (cit. on pp. 3, 55, 56).

Tang, L. and M. P. Païdoussis (2007). "On the instability and the post-critical behaviour of two-dimensional cantilevered flexible plates in axial flow". In: *Journal of Sound and Vibration* 305.1-2, pp. 97–115. DOI: 10.1016/j.jsv.2007.03.042 (cit. on p. 3).

Tanida, Y. (2001). "Stability of a Soft Plate in Channel Flow (Aerodynamic Aspects of Palatal Flutter)". In: *JSME International Journal* 44.1, pp. 8–13. DOI: 10.1299/jsmeb.44.8 (cit. on p. 3).

Watanabe, Y (2002). "An experimental study of paper flutter". In: *Journal of Fluid and Structures* 16.4, pp. 529–542. DOI: 10.1006/jfls.2001.0435 (cit. on p. 63).

Wendland, H. (1995). "Piecewise polynomial, positive definite and compactly supported radial functions of minimal degree". In: *Advances in Computational Mathematics* 4, pp. 389–396. DOI: 10.1007/BF02123482 (cit. on p. 45).

Werter, N. P. M. (2012). *An Advanced Aeroelastic Tailoring Tool for Wing Optimisation*. Tech. rep. Delft University of Technology (cit. on pp. 10, 11, 27, 36, 60).

Werter, N. P. M. and R. De Breuker (2015). "Aeroelastic Tailoring and Structural Optimisation using an Advanced Dynamic Aeroelastic Framework". In: *International Forum on Aeroelasticity and Structural Dynamics*. Saint Petersburg, pp. 1–20 (cit. on pp. 35, 36).

Werter, N P M and R De Breuker (2016). "A novel dynamic aeroelastic framework for aeroelastic tailoring and structural optimisation q". In: *Composite Structures* 158, pp. 369–386. DOI: 10.1016/j.compstruct.2016.09.044 (cit. on p. 50).

Werter, N. P. M., R. De Breuker, and M. M. Abdalla (2015). "Continuous-time State-space Unsteady Aerodynamic Modelling for Efficient Aeroelastic Load Analysis". In: *International Forum on Aeroealsticity and Structural Dynamics*. Saint Petersburg (cit. on p. 37).

Wright, J. R. and J. E. Cooper (2007). *Introduction to Aircraft Aeroelasticity and Loads*. 1st ed. Chichester: John Wiley & Sons Ltd, p. 499. DOI: 10.1002/9781118700440 (cit. on p. 80).

A

Classical lamination theory

This appendix shortly explains the method used to calculate the response of the laminate under applied forces. For this purpose the classical laminate theory is used, following the approach explained in Kassapoglou (2010). In Figure A.1, the coordinate system used is defined. The indices 1 and 2 are used to represent the local coordinate system of the ply. With 1 being in the longitudinal direction and 2 in the direction perpendicular to the fibers. X and y are the axes of global coordinate system of the laminate. The angle θ indicates the angle of the fibers in each ply of the laminate.

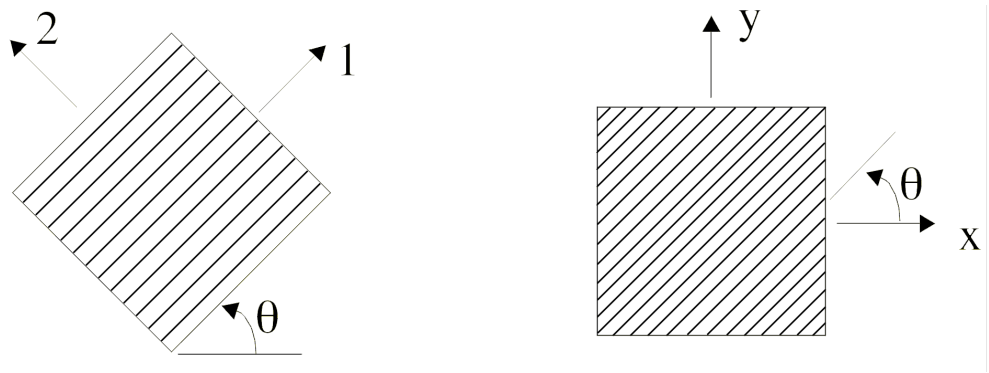

Figure A.1: Definition of the local coordinate system used for each ply and the global coordinate system of the laminate

For each ply of the laminate the constitutive relations for a single orthotropic layer are written. It is assumed that the ply is in a state of plane stress, which significantly simplifies the stiffness matrix and yields the following relation between the strains and stresses in each ply in the local coordinate system:

$$\begin{Bmatrix} \sigma_1 \\ \sigma_2 \\ \tau_{12} \end{Bmatrix} = \begin{bmatrix} Q_{11} & Q_{12} & 0 \\ Q_{12} & Q_{22} & 0 \\ 0 & 0 & Q_{66} \end{bmatrix} \begin{Bmatrix} \varepsilon_1 \\ \varepsilon_2 \\ \gamma_{12} \end{Bmatrix} \tag{A.1}$$

The elements in the reduced stiffnes matrix Q are the following:

$$Q_{11} = \frac{E_1}{1 - \nu_{12} \cdot \nu_{21}} \tag{A.2a}$$

$$Q_{22} = \frac{E_2}{1 - \nu_{12} \cdot \nu_{21}} \tag{A.2b}$$

$$Q_{12} = \frac{\nu_{12} \cdot E_2}{1 - \nu_{12} \cdot \nu_{21}} \tag{A.2c}$$

$$Q_{66} = G_{12} \tag{A.2d}$$

When the stress strain relation in the local coordinate system of the ply is known, the stresses and strains can be transformed to the global x and y coordinate system of the laminate. The stresses and strains are related in the laminate coordinate system as follows:

$$\begin{Bmatrix} \sigma_x \\ \sigma_y \\ \tau_{xy} \end{Bmatrix} = \begin{bmatrix} \overline{Q}_{11} & \overline{Q}_{12} & \overline{Q}_{16} \\ \overline{Q}_{12} & \overline{Q}_{22} & \overline{Q}_{26} \\ \overline{Q}_{16} & \overline{Q}_{26} & \overline{Q}_{66} \end{bmatrix} \begin{Bmatrix} \varepsilon_x \\ \varepsilon_y \\ \gamma_{xy} \end{Bmatrix} \tag{A.3}$$

The $\overline{Q}$ matrix or the transformed reduced stiffness matrix is obtained by using material invariants. With this method, the elements in the $\overline{Q}$ matrix can all be expressed in terms of material properties only:

$$\overline{Q}_{11} = U_1 + U_2 \cdot \cos(2\theta) + U_3 \cdot \cos(4\theta) \tag{A.4a}$$
$$\overline{Q}_{22} = U_1 - U_2 \cdot \cos(2\theta) + U_3 \cdot \cos(4\theta) \tag{A.4b}$$
$$\overline{Q}_{12} = U_4 + U_3 \cdot \cos(4\theta) \tag{A.4c}$$
$$\overline{Q}_{66} = U_5 - U_3 \cdot \cos(4\theta) \tag{A.4d}$$
$$\overline{Q}_{16} = \frac{1}{2} \cdot (U_2 \cdot \sin(2\theta) + U_3 \sin(4\theta)) \tag{A.4e}$$
$$\overline{Q}_{26} = \frac{1}{2} \cdot (U_2 \cdot \sin(2\theta) - U_3 \cdot \sin(4\theta)) \tag{A.4f}$$

With the following invariants U_i:

$$U_1 = \frac{1}{2}(3 \cdot Q_{11} + 3 \cdot Q_{22} + 2 \cdot Q_{12} + 4 \cdot Q_{66}) \tag{A.5a}$$
$$U_2 = \frac{1}{2}(Q_{11} - Q_{22}) \tag{A.5b}$$
$$U_3 = \frac{1}{8}(Q_{11} + Q_{22} - 2 \cdot Q_{12} - 4 \cdot Q_{66}) \tag{A.5c}$$
$$U_4 = \frac{1}{8}(Q_{11} + Q_{22} + 6 \cdot Q_{12} - 4 \cdot Q_{66}) \tag{A.5d}$$
$$U_5 = \frac{1}{8}(Q_{11} + Q_{22} - 2 \cdot Q_{12} + 4 \cdot Q_{66}) \tag{A.5e}$$

The transformed reduced stiffness matrix can be computed for each ply of the laminate, after which the ABD matrix for the entire laminate can be computed. The elements in the ABD matrix are calculated with the following equations:

$$A_{ij} = \sum_{k=1}^{n} \overline{Q}_{ij} \cdot (z_k - z_{k-1}) \tag{A.6a}$$
$$B_{ij} = \sum_{k=1}^{n} \overline{Q}_{ij} \cdot (z_k^2 - z_{k-1}^2) \tag{A.6b}$$
$$D_{ij} = \sum_{k=1}^{n} \overline{Q}_{ij} \cdot (z_k^3 - z_{k-1}^3) \tag{A.6c}$$

In these equations, z stands for the local height of the ply in the laminate, these heights are defined in Figure A.2. Note that layer 1 is the lower side of the laminate and in the matlab code, z_1 is defined as the height representing the lower side of the laminate.

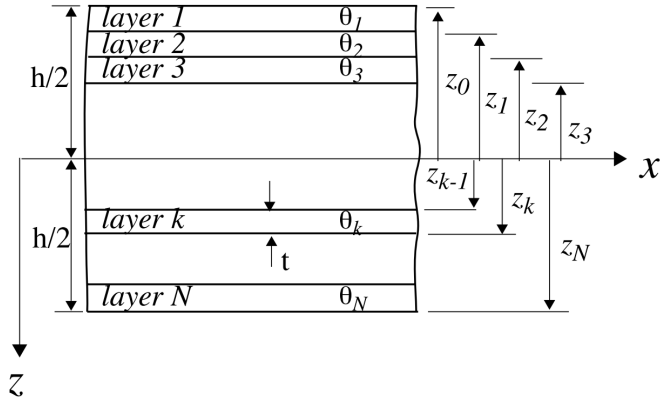

Figure A.2: Definition of the laminate

Then the ABD matrix can be written as follows:

$$\begin{Bmatrix} N_x \\ N_y \\ N_{xy} \\ M_x \\ M_y \\ M_{xy} \end{Bmatrix} = \begin{bmatrix} A_{11} & A_{12} & A_{16} & B_{11} & B_{12} & B_{16} \\ A_{12} & A_{22} & A_{26} & B_{12} & B_{22} & B_{26} \\ A_{16} & A_{26} & A_{66} & B_{16} & B_{26} & B_{66} \\ B_{11} & B_{12} & B_{16} & D_{11} & D_{12} & D_{16} \\ B_{12} & B_{22} & B_{26} & D_{12} & D_{22} & D_{26} \\ B_{16} & B_{26} & B_{66} & D_{16} & D_{26} & D_{66} \end{bmatrix} \begin{Bmatrix} \varepsilon_x^0 \\ \varepsilon_y^0 \\ \gamma_{xy}^0 \\ \kappa_x \\ \kappa_y \\ \kappa_{xy} \end{Bmatrix} \tag{A.7}$$

Using the ABD matrix, the mid plane strains ϵ^0 and the curvatures κ can be calculated as follows:

$$\begin{Bmatrix} \varepsilon^0 \\ \kappa \end{Bmatrix} = \mathbf{ABD}^{-1} \begin{Bmatrix} N \\ M \end{Bmatrix} \tag{A.8}$$

The strains in each ply in the laminate coordinate system can then be computed using Equation (A.9) and for each ply, the srains at the top and the bottom are calculated.

$$\varepsilon_x(x,y,z) = \varepsilon^o{}_x(x,y) + z_k \cdot \kappa_x(x,y) \tag{A.9a}$$
$$\varepsilon_y(x,y,z) = \varepsilon^o{}_y x,y) + z_k \cdot \kappa_y(x,y) \tag{A.9b}$$
$$\gamma_{xy}(x,y,z) = \gamma^o{}_{xy}(x,y) + z_k \cdot \kappa_{xy}(x,y) \tag{A.9c}$$